



# LUND UNIVERSITY

## Temperature Dependent in situ Studies of two Simple Structure Types Revealing Modulation or the Art of Making Glitter

Folkers, Laura

2019

*Document Version:*

Publisher's PDF, also known as Version of record

[Link to publication](#)

*Citation for published version (APA):*

Folkers, L. (2019). *Temperature Dependent in situ Studies of two Simple Structure Types Revealing Modulation: or the Art of Making Glitter*. [Doctoral Thesis (compilation), Lund University]. Lund University, Faculty of Engineering.

*Total number of authors:*

1

### General rights

Unless other specific re-use rights are stated the following general rights apply:

Copyright and moral rights for the publications made accessible in the public portal are retained by the authors and/or other copyright owners and it is a condition of accessing publications that users recognise and abide by the legal requirements associated with these rights.

- Users may download and print one copy of any publication from the public portal for the purpose of private study or research.
- You may not further distribute the material or use it for any profit-making activity or commercial gain
- You may freely distribute the URL identifying the publication in the public portal

Read more about Creative commons licenses: <https://creativecommons.org/licenses/>

### Take down policy

If you believe that this document breaches copyright please contact us providing details, and we will remove access to the work immediately and investigate your claim.

LUND UNIVERSITY

PO Box 117  
221 00 Lund  
+46 46-222 00 00

# Temperature Dependent *in situ* Studies of two Simple Structure Types Revealing Modulation: or the Art of Making Glitter

LAURA CHRISTINA FOLKERS | CENTRE FOR ANALYSIS AND SYNTHESIS | LUND UNIVERSITY





Temperature Dependent *in situ* Studies of two Simple Structure  
Types Revealing Modulation





# Temperature Dependent *in situ* Studies of two Simple Structure Types Revealing Modulation

Or The Art of making Glitter

by Laura Christina Folkers



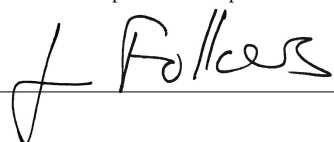
**LUND**  
UNIVERSITY

Thesis for the degree of Doctor of Philosophy  
Thesis advisors: Prof. Sven Lidin, Prof. Jan-Olle Malm  
Faculty opponent: Prof. Joke Hadermann

To be presented, with the permission of the Faculty of Engineering of Lund University,  
for public criticism in lecture hall B at the Department of Chemistry  
on Friday, the 6th of December 2019 at 13:15.

Organization <b>LUND UNIVERSITY</b>		Document name <b>DOCTORAL DISSERTATION</b>
Department of Chemistry Box 124 SE-221 00 LUND Sweden		Date of dissertation 2019-12-06
Author Laura Christina Folkers		Sponsoring organization Westlings Minnesfond (Grant 2015-05227) The Royal Physiographic Society of Lund (Application No.: 38572)
Title and subtitle Temperature Dependent <i>in situ</i> Studies of two Simple Structure Types Revealing Modulation: Or The Art of making Glitter		
Abstract <p>In the first part of this thesis, three intermetallic compounds are discussed, that were originally thought of as thallium iodide type compounds. Starting from small evidence that there is more than meets the eye, investigations began to find the true structure of AuIn. AuIn emerged to be modulated with various domain sizes over temperatures between room temperature and 400°C, where at room temperature it shows satellite reflections up to third order that are fully replaced by diffuse scattering at 400°C. While the atomic network is optically the same at all temperatures, the space group changes from the incommensurate <math>C\bar{1}(\alpha, \beta, \gamma)0</math> at room temperature to <math>Cmcm</math> at 400°C and the gold network appears as a Peierls type distorted version of the thallium network in TII.</p> <p>In addition the alloys PdBi and PdPb were examined with PdBi showing a very similar behaviour to AuIn, <i>i.e.</i> showcasing various degrees of modulation between room temperature and 300°C and Pd adopting a Peierls type distorted version of the thallium network in TII. For PdPb only room temperature data was measured so far, which also shows promising features of a Peierls type distorted thallium network for Pd.</p> <p>The second part of the thesis addresses the alloy Sn<sub>3</sub>Sb<sub>2</sub>, which is a high temperature modification of stisite, SnSb. Its structure can only be accessed <i>in situ</i> when a pre-grown crystal is mounted in a capillary with an additional piece of tin. This sample has to be heated to a temperature of 250°C to enable the structural transition. If the sample is monitored by X-ray diffraction during the heating process, the decay of the <math>\beta</math>-tin reflections and the upsurge of the ordered Sn<sub>3</sub>Sb<sub>2</sub> can be witnessed. Resulting is a structure consisting of 7x7x7 NaCl-type clusters interleaved by single Sn layers, presenting the space group <math>Xm\bar{3}m</math>.</p> <p>These two parts are unified by both of them dealing with a simple structure type, which reveals modulation that can be studied <i>in situ</i>.</p>		
Key words Crystallography, Modulation, Intermetallics		
Classification system and/or index terms (if any)		
Supplementary bibliographical information		Language English
ISSN and key title		ISBN 978-91-7422-698-0 (print) 978-91-7422-699-7 (pdf)
Recipient's notes	Number of pages 194	Price
	Security classification	

I, the undersigned, being the copyright owner of the abstract of the above-mentioned dissertation, hereby grant to all reference sources the permission to publish and disseminate the abstract of the above-mentioned dissertation.

Signature 

Date 2019-10-24

# Temperature Dependent *in situ* Studies of two Simple Structure Types Revealing Modulation

Or The Art of making Glitter

by Laura Christina Folkers



**LUND**  
UNIVERSITY

**Cover illustration front:** “From the X-ray Tube to the Diffraction Pattern”. Drawing by Gerd Folkers 2019.

**Cover illustration back:** “A Laboratory Restored”, Artist unknown. Inv 99027 © History of Science Museum, University of Oxford.

**Funding information:** The thesis work was financially supported by the Swedish Research Council, Westlings Minnesfond and the Physiographic Society of Lund.

© Laura Christina Folkers 2019

Faculty of Engineering, Department of Chemistry

ISBN: 978-91-7422-698-0 (print)

ISBN: 978-91-7422-699-7 (pdf)

Printed in Sweden by Media-Tryck, Lund University, Lund 2019



Media-Tryck is an environmentally certified and ISO 14001:2015 certified provider of printed material. Read more about our environmental work at [www.mediatryck.lu.se](http://www.mediatryck.lu.se)

**MADE IN SWEDEN** 

*Der Festkörper ist das Grab der Chemie ...  
aber in diesem Grab kann ganz schön viel los sein! - R. Nesper*

# Contents

List of publications . . . . .	iv
Acknowledgements . . . . .	vi
Popular summary in English . . . . .	viii
Populärwissenschaftliche Zusammenfassung auf Deutsch . . . . .	x
Populärvetenskaplig sammanfattning på svenska . . . . .	xii
Lists of used Abbreviations and Symbols . . . . .	xiv
Abbreviations . . . . .	xiv
Structure Symbols . . . . .	xiv
Physical Symbols . . . . .	xiv
<b>Temperature Dependent in situ Studies of two Simple Structure Types Revealing Modulation: Or The Art of making Glitter</b>	<b>1</b>
1 Disclaimer . . . . .	1
2 Introduction* . . . . .	2
2.1 Intermetallics* . . . . .	2
2.2 The Thallium-Iodide Structure Type . . . . .	2
2.2.1 Gold-Indium* . . . . .	5
2.2.2 Palladium-Bismuth . . . . .	6
2.2.3 Palladium-Lead . . . . .	7
2.3 The NaCl Structure Type . . . . .	8
2.3.1 Tin-Antimony* . . . . .	10
2.4 Short Overview of 3D Crystallography* . . . . .	13
2.5 Introduction to Higher Dimensional Crystallography* . . . . .	16
2.6 The 3D- $\Delta$ Pair Distribution Function . . . . .	18
3 Motivation and Hypothesis . . . . .	21
4 Used Techniques* . . . . .	23
4.1 Synthesis . . . . .	23
4.2 Thermal Analysis . . . . .	25
4.3 X-ray Sources . . . . .	26
4.4 Single Crystal X-ray Diffraction* . . . . .	30
4.5 Powder Diffraction* . . . . .	31
4.6 Synchrotron X-ray Diffraction* . . . . .	34

	4.6.1	CRISTAL Beam Line at Synchrotron SOLEIL . . .	35
	4.6.2	I19 Beam Line at Synchrotron Diamond . . . . .	35
	4.7	Anomalous Dispersion . . . . .	35
5		Main Results of the Research Papers . . . . .	37
	5.1	AuIn* . . . . .	37
	5.1.1	Experimental* . . . . .	37
	5.1.2	Results and Discussion* . . . . .	38
	5.2	PdBi . . . . .	49
	5.2.1	Experimental . . . . .	49
	5.2.2	Results and Discussion . . . . .	49
	5.3	PdPb . . . . .	57
	5.3.1	Experimental . . . . .	57
	5.3.2	Results and Discussion . . . . .	58
	5.4	Postulation of TII's Subgroup IIa . . . . .	61
	5.4.1	Thermal Analyses . . . . .	61
	5.4.2	Structural Shape . . . . .	64
	5.4.3	Diffuse scattering . . . . .	64
	5.5	Sn <sub>3</sub> Sb <sub>2</sub> * . . . . .	65
	5.5.1	Experimental* . . . . .	65
	5.5.2	Results and Discussion* . . . . .	67
6		Outlook* . . . . .	71
7		References . . . . .	72
<b>Scientific publications</b>			77
	Author contributions . . . . .		77
	Paper I: The Mystery of the AuIn 1:1 Phase and its Incommensurate Structural Variations . . . . .		77
	Paper II: Incommensurability in Entangled Bonding Networks: Temperature-Dependent Structural Variations in PdBi . . . . .		77
	Paper III: PdPb: The Incommensurately modulated structure of another TII type compound . . . . .		77
	Paper IV: <i>In situ</i> synthesis and single crystal synchrotron X-ray diffraction study of ht-Sn <sub>3</sub> Sb <sub>2</sub> . . . . .		78
	Paper I: The Mystery of the AuIn 1:1 Phase and its Incommensurate Structural Variations . . . . .		79
	Paper II: Incommensurability in Entangled Bonding Networks: Temperature-Dependent Structural Variations in PdBi . . . . .		87
	Paper III: PdPb: The Incommensurately modulated structure of another TII type compound . . . . .		101
	Paper IV: <i>In situ</i> synthesis and single crystal synchrotron X-ray diffraction study of ht-Sn <sub>3</sub> Sb <sub>2</sub> . . . . .		111



## List of publications

This thesis is based on the following publications, referred to by their Roman numerals:

- I **The Mystery of the AuIn 1:1 Phase and its Incommensurate Structural Variations**  
L. C. Folkers, A. Simonov, F. Wang, S. Lidin  
Inorganic Chemistry, 2018 57 (5), pp. 2791-2796  
DOI: 10.1021/acs.inorgchem.7b03206
  
- II **Incommensurability in Entangled Bonding Networks: Temperature-Dependent Structural Variations in PdBi**  
L. C. Folkers, H. E. Mitchell Warden, D. C. Fredrickson, S. Lidin  
Manuscript in preparation
  
- III **PdPb: The Incommensurately modulated structure of another TII type compound**  
L. C. Folkers, S. Lidin  
Manuscript in preparation
  
- IV **In situ synthesis and single crystal synchrotron X-ray diffraction study of ht-Sn<sub>3</sub>Sb<sub>2</sub>**  
S. Lidin, L. C. Folkers  
Accounts of Chemical Research, 2018 51 (2), pp. 223-229  
DOI: 10.1021/acs.accounts.7b00508

All papers are reproduced with permission of their respective publishers.

Publications not included in this thesis:

**Allotwinning and OD-structures – the example of malonamide**

D. Strand, L. Folkers, S. Lidin

Zeitschrift für Kristallographie - Crystalline Materials, 2016 231 (10), pp. 2791-2796

DOI: 10.1515/zkri-2016-1969

**Variations in the Composition of the Phases Lead to the Differences in the Optoelectronic Properties of MAPbBr<sub>3</sub> Thin Films and Crystals**

Q. Shi, S. Ghosh, P. Kumar, L. C. Folkers, S. K. Pal, T. Pullerits, K. J. Karki

The Journal of Physical Chemistry C, 2018 122 (38), pp. 21817-21823

DOI: 10.1021/acs.jpcc.8b06937

**Y<sub>3</sub>Ru<sub>(2-x)</sub> — A Representative of a Composite Modulated Family of Intermetallics**

S. Lidin, L. Folkers

Crystals, 2019 9 (4), pp. 189

DOI: 10.3390/cryst9040189

**Antibacterial Effect of Silver Nanoparticles (AgNPs) Synthesized from Trichoderma Harzianum against Clavibacter Michiganensis**

A. Noshad, M. Iqbal, L. C. Folkers, C. Hetherington, A. Khan, M. Numan, S. Ullah

Journal of Nano Research, 2019 58, pp. 10-19

DOI: 10.4028/www.scientific.net/JNanoR.58.10

## Acknowledgements

First of all I want to thank my supervisor Sven Lidin. Thank you so much for always finding time for discussions and answering emails no matter the time of day or the continent you are currently on! Also you have always given me the freedom to work when, where and on whatever I wanted, giving me the chance to follow my own interests and learn from my mistakes. Moreover you always believed in my work and offered advice whenever I needed it. All in all: thank you for a wonderful PhD experience!

Jan-Olle Malm, thank you for giving great advice during teaching, but also in many other situations!

I would like to extend my gratitude to Joke Hadermann who kindly agreed to be my faculty opponent. It is a great pleasure to have an excellent role model for young female scientists as an opponent.

Also, I am thankful to the committee members Lars Eriksson, Johanna Rosén, Lars Öhrström and Ola Wendt for having agreed to read and scrutinise this thesis and also join us at the thesis defence for discussing this work.

Thank you, Reine Wallenberg for volunteering to read the first version of this thesis and helping so much with all the admin parts!

Further on I am greatly indebted to the beam line scientist at SOLEIL, Pierre Ferte, the beam line scientists at Diamond, Harriott Nowell and David Allan, our co-authors Arkadiy Simonov, Fei Wang, Hillary Mitchell Warden and Daniel Fredrickson, and also Hossein Sina for his help with the DSC measurements.

To the PolyMat lunch group (Andrit, Axel, Crispin, Dong, Hannes, Huong, Joel, Monika, Niklas, Nitin, Olivier, Pegah, Ping, Robin, Sathiyaraj, Smita, Xiaoya): Thank you for a lot fun during lunch time, game and pub nights! It was a wonderful time!

Maria: Thank you so much for always having time for my questions, even if I ask the same thing for the hundredth time! Even more so it is great fun to come to your office and just enjoy a nice Star Wars and pun laden chat.

Katarina: Thank you for being Santa's little helper and bringing all the things we order to our office and labs! And also for digging out age old quotations that I suddenly need and scouting for unusual materials I wanted to order.

To all CAS: Thank you all for making this a great and inspiring work environment!

Thank you to my master and internship students Joel Mattsson and Juliette Beunat: I have learnt a lot about supervising thanks to the two of you!

Also thank you to all the students in my courses for being my Guinea pigs and enduring all my dad jokes. I always enjoyed teaching a lot and know that I am lucky to have had students that were interested in the topics and motivated to learn.

Clara: It is wonderful to know that you are my friend no matter what happens. Your personality and your drive are a complete inspiration to me!

Vicky: Actually, it is kind of crazy that we met by mere coincidence and I wonder some times if our paths had crossed if we hadn't both lived in Möllevångsvägen. I am more than glad however that we did meet! Over the last four and a half years you became such an invaluable friend and have morally supported me through so much of this PhD journey.

Cassandra and the rest of the knitting club: It is great to share the passion for crafting (and cheese!) with you and have the chance to take my mind off of work!

Cinthia, Margarida, Ella, Lucy, Paul, Frank, Pablo, Arkadiy and all the other lovely people I met at conferences over the last few years: thank you for always taking me along and making travelling alone much more fun!

Nina, Paul, Andy, Alex, Jolanda, Jens, Roli: Danke dass ich immernoch ein Teil der "Gang" bin, auch wenn ich so weit weg wohne. Es ist wunderbar jedes Jahr heim zu kommen und mit euch allen Sylvester zu feiern!

Anna, Linnéa, Christina, Erik, Abbe och Sivan: Tack så mycket för att ni har välkomnat mig så varmt i familjen.

Christoffer: Thank you for being you! Your personality, your humour, your ideas for the future just click together with mine, like cogwheels.

Mama und Papa: Danke, dass ihr mich immer gefördert und gefordert habt und mir nie das Gefühl gegeben habt, dass ich etwas nicht erreichen könnte. Ohne eure Liebe und eure guten Ratschläge wäre ich nicht wo ich heute bin!

## Popular summary in English

This thesis is from the area of fundamental science and any possible industrial applications of the here discussed alloys are still far ahead in the future. So be warned, here be dragons.

When hearing the term crystal, many may think of the beautiful quartz or amethyst geodes one sees in natural history museums, which are crystals indeed and were the kinds of crystals that the first crystallographic studies were conducted on. In the time when crystallography started, researchers were bound to work with large enough specimens that clearly exhibited their inherent order so that it was visible by the naked eye. Nowadays, thanks to modern tools, the sample size has been reduced to submillimetre size - think the width of your hair - while the amount of specimens studied, that exhibit unusual effects, has increased. As the research below revolves around aperiodic or modulated crystals, you will find yourself reading mostly about those rather unusual specimens. Before defining what that is, let us start by the definition of what a crystal is. When Häuy formulated the mathematical theory of crystallography at the end of the 18<sup>th</sup> century, he based it on the premise that atoms must be ordered periodically (in the same reoccurring pattern) to produce a crystal [1]. As Dan Shechtman discovered quasicrystals - crystals that show global, but aperiodic order - a paradigm shift had to occur and the new definition of a crystal according to the International Union of Crystallography (IUCr) is as follows: "A material is a crystal if it has essentially a sharp diffraction pattern. The word essentially means that most of the intensity of the diffraction is concentrated in relatively sharp Bragg peaks, besides the always present diffuse scattering" [2]. A diffraction pattern is the Bragg spot pattern that emerges when light of a wavelength similar to interatomic distances is shone onto a crystal and the diffracted rays are collected by a detector. As found by father and son Bragg, X-rays possess the correct wavelength to produce those patterns. The patterns are essentially arrangements of maxima of constructive interference that give information about particular distances found within the crystal.

IUCr's new definition is also more welcoming to the incommensurately modulated structures that will be discussed in this thesis, which however already show a certain amount of inherent order. Incommensurability means that the considered crystals do not show translational symmetry, which is sloppily said, the traditional way to receive long range order (the feature required to obtain discrete Bragg spots). In incommensurate structures long range order is produced from something called modulation. In the easiest case this can be pictured by an atom which is, instead of sitting always at exactly the same position in the unit cell - the smallest building block of a crystal -, seemingly arbitrarily moved away from its, let's call it, original position. Most importantly this difference to its original position is a bit different in every unit cell. If a few unit cells are depicted together, it can be seen that the displacement of the atom

will follow a pattern, for example a sinusoidal wave.

Essentially this work will be split in two sections with the first concerning work on thallium iodide (TII) type alloys and the second concerning work on the high temperature structure of tin antimony ( $\text{Sn}_3\text{Sb}_2$ ). Work on the TII type alloys started out by investigating gold indium (AuIn), which did not crystallise as easily as was expected of it. Thermal analyses and diffraction studies at elevated temperatures uncovered a modulated structure undergoing various structural transformations. While working with AuIn, it was found that also palladium bismuth (PdBi) and palladium lead (PdPb) behave in a similar way, which lead to additionally investigating those structures. Emerging were three alloys that deviate all in a similar fashion from their originally postulated structures, which lead to the hypothesis that there exists a whole subgroup of structures behaving this way.

Previous work on  $\text{Sn}_3\text{Sb}_2$  had uncovered, that this compound undergoes an unquenchable phase transition and hence making its structure inaccessible to any room temperature measurement. Excitingly, it could be synthesised *in situ* from SnSb and excess Sn directly during synchrotron measurements, revealing that the  $\text{Sn}_3\text{Sb}_2$  structure can soak up tin like a sponge. Analysis of the resulting data uncovered an extraordinarily rare aperiodic crystal structure.

What binds together the two parts described above is their fascinating and exceptional nature: both exhibit modulation of simple underlying type structures, where the modulation can be accessed by *in situ* temperature dependent X-ray diffraction!

## Populärwissenschaftliche Zusammenfassung auf Deutsch

Die in dieser Dissertation beschriebenen Untersuchungen sind alle dem Themengebiet der Grundlagenforschung zuzuordnen. Mögliche Verwendung der Phasen für die Industrie sind bisher noch unerforscht. Daher sei der\*die Leser\*in von hier an gewarnt: “*Hic sunt dracones*”.

Bei dem Wort Kristall denken viele an die hübschen Amethyste oder Bergkristalle, die in vielen naturhistorischen Museen ausgestellt sind. Diese Art von Kristallen sind auch tatsächlich diejenigen, an denen die ersten kristallographischen Studien durchgeführt wurden. Da entsprechende Gerätschaften noch nicht erfunden worden waren, mussten Proben verwendet werden, die gross genug waren, um sie von Auge zu inspizieren. Dank moderner Technik können heutzutage Proben von der Gröszenordnung der Breite eines menschlichen Haares untersucht werden. Ausserdem ermöglicht sowohl die Entwicklung moderner Software als auch moderner Maschinen, dass ungewöhnliche Effekte besser aufgelöst und modelliert werden können. Da die hier vorgestellten Forschungsergebnisse zum Themengebiet der aperiodischen respektive modullierten Kristallstrukturen gehören, werden Sie als Leser sich in eben dieser Gegend der ungewöhnlichen Effekte bewegen. Doch bevor wir darüber sprechen, lassen Sie uns mit der Definition eines “gewöhnlichen” Kristalls beginnen. Als Haüy am Ende des 18. Jahrhunderts seine mathematische Theorie der Kristallographie formulierte, legte er dieser die Voraussetzung zugrunde, dass Atome periodisch (nach dem gleichen, wiederkehrenden Muster) geordnet sein müssen, um einen Kristall zu bilden [1]. Dan Shechtmans Entdeckung der Quasikristalle - Kristalle die nur lokale Ordnung zeigen - forderte einen Paradigmenwechsel ein, der zu folgender neuer Definition eines Kristalls führte: “A material is a crystal if it has essentially a sharp diffraction pattern. The word essentially means that most of the intensity of the diffraction is concentrated in relatively sharp Bragg peaks, besides the always present diffuse scattering.” [2]. (Ein Material ist ein Kristall, wenn es grundsätzlich ein scharfes Beugungsmuster zeigt. Das Wort grundsätzlich ist hier so zu verstehen, dass die meiste Beugungsintensität in relativ scharfen Bragg Punkten zu finden ist, neben der immer anwesenden diffusen Streuung. Freie Übersetzung der Autorin.) Ein Beugungsmuster entsteht, wenn Licht mit einer Wellenlänge ähnlich des Abstandes zweier Atome im Festkörper auf einen Kristall trifft und die vom Kristall gebeugten Strahlen von einem Detektor erfasst werden. Wie von Vater und Sohn Bragg festgestellt, haben Röntgenstrahlen die richtige Wellenlänge, um dieses Punktmuster zu produzieren. Die Punkte selbst sind im Grunde ein Interferenzmuster, das Aufschluss über Distanzen zwischen den Atomen im Kristall gibt.

Die neue Definition eines Kristalls eröffnet ausserdem die Möglichkeit, die hier diskutierten inkommensurat modulierten Strukturen als Kristalle zu bezeichnen, wobei diese bereits eine gewisse inhärente Ordnung zeigen. Inkommensurabilität bedeutet,

dass die entsprechenden Kristalle keine Translationssymmetrie zeigen, welche salopp gesagt, die traditionelle Art ist, Fernordnung zu erhalten (die Eigenschaft, die nötig ist, um diskrete Bragg Punkte zu erhalten). Inkommensurate Strukturen erhalten ihre Fernordnung durch die sogenannte Modulation. Diese lässt sich im einfachsten Fall durch ein Atom darstellen, das in jeder benachbarten Elementarzelle - der kleinsten Baueinheit eines Kristalls - scheinbar arbiträr von seiner, nennen wir sie originalen, Position verschoben wurde. Wichtig ist, dass die Distanz, um die das Atom verschoben wurde, in jeder Elementarzelle ein bisschen anders ist. Werden ein paar Elementarzellen nebeneinander dargestellt, kann man erkennen, dass die Verschiebung des Atoms zum Beispiel einer Sinuskurve folgt.

Die vorgelegte Dissertation ist in zwei Teile unterteilt, wobei der erste Teil von der Arbeit über die Legierungen des Thalliumiodidtyps (TII) und der zweite Teil von der Arbeit an der Hochtemperaturstruktur des Zinnantimonids ( $\text{Sn}_3\text{Sb}_2$ ) handelt. Die Arbeit an den TII-typ Legierungen begann mit Untersuchungen an Gold Indium (AuIn), das interessant wurde, da es nicht so einfach Kristalle bildete wie erwartet. Thermische Analysen und Beugungsstudien bei hohen Temperaturen zeigten, dass AuIn eine modulierte Struktur bildet, die verschiedene Phasenübergänge durchläuft. Währenddessen wurde entdeckt, dass sich Palladium Bismut (PdBi) und Palladium Blei (PdPb) ähnlich verhalten. Daher wurden auch diese Strukturen untersucht, was zu drei Legierungen führte, die alle auf ähnliche Weise von ihren ursprünglich postulierten Strukturen abweichen. Dies wiederum führte zu der Hypothese, dass tatsächlich eine ganze Untergruppe der TII-typ Strukturen existiert, die sich ähnlich verhalten.

Frühere Arbeiten an  $\text{Sn}_3\text{Sb}_2$  hatten gezeigt, dass diese Legierung einen Phasenübergang aufweist, der nicht zu umgehen ist. Daher ist die entsprechende Struktur mit jeglichen Analysemethoden bei Raumtemperatur nicht zu erreichen. Aufregenderweise zeigte sich in dieser Arbeit, dass es möglich war, diese Struktur *in situ* aus SnSb und überschüssigem Sn direkt während der Messung herzustellen. Damit wurde auch gezeigt, dass  $\text{Sn}_3\text{Sb}_2$  wie ein Schwamm Zinn aufsaugen kann. Die Analyse der erhaltenen Daten zeigte eine extrem seltene aperiodische Kristallstruktur.

Was die beiden oben beschriebenen Projekte verbindet, ist ihre faszinierende Aussergewöhnlichkeit: Beide Fälle zeigen modulierte Strukturen denen einfache Strukturtypen zugrunde liegen. Diese modulierte Strukturen können ausserdem *in situ* mit temperaturabhängiger Röntgenbeugung gemessen werden!



## Populärvetenskaplig sammanfattning på svenska

Den här avhandlingen berör grundläggande vetenskap, och möjliga industriella applikationer av legeringarna diskuterade häri ligger fortfarande långt i framtiden. Så känn dig varnad, *hic sunt dracones*.

När man hör ordet kristall tänker kanske många på de fina kvarts- eller ametistgeoderna som visas i naturhistoriska muséer, som faktiskt är kristaller och det var de som man gjorde de första kristallografiska undersökningarna på. I kristallografins barndom var det nödvändigt att arbeta med prover som var tillräckligt stora, så att man kunde se dem med blotta ögat. Numera, tack vare modern teknik, har provstorleken minskats till submillimeterstorlek - tänk bredden av ett hårstrå - medan mängden av studerade prover med ovanliga egenskaper har ökat. Eftersom forskningen du kommer att läsa om nedan handlar om modulerade eller aperiodiska kristaller, är det dessa ovanliga prover vi kommer att prata om. Men innan vi definerar vad ordet "aperiodisk" betyder, ska vi börja med definitionen av en kristall. När Haiüy formulerade den matematiska teorin för kristallografi i slutet av 1700-talet, baserade han den på premissen att atomerna måste vara ordnade periodiskt (i samma återkommande mönster) för att producera en kristall [1]. När Dan Shechtman upptäckte kvasikristaller - kristaller som visar global men aperiodisk ordning - skedde ett paradigmskifte. Den nya definitionen av en kristall enligt the International Union of Crystallography (IUCr) är: "A material is a crystal if it has essentially a sharp diffraction pattern. The word essentially means that most of the intensity of the diffraction is concentrated in relatively sharp Bragg peaks, besides the always present diffuse scattering." [2]. Ett diffraktionsmönster (diffraction pattern) är det Braggtoppmönster som uppstår när ljus av en våglängd liknande avståndet mellan atomerna skiner på en kristall och de böjda strålarna samlas upp av en detektor. Som upptäckt av far och son Bragg, har röntgenstrålar den korrekta våglängden för att producera dessa mönster. Mönstren är faktiskt interferenser som ger information om särskilda avstånd i kristallen.

IUCr's nya definition är också mer inkluderande för de inkommensurat modulerade strukturerna som diskuteras i den här avhandlingen, som har ett visst mått av ordning. Inkommensurabilitet betyder att de betraktade kristallerna inte visar någon translationssymmetri, som enkelt uttryckt är det traditionella sättet att erhålla ordning på lång skala (egenskapen som behövs för att erhålla diskreta Braggtoppar). I inkommensurata strukturer produceras ordning på lång skala av något som kallas modulering. I det enklaste fallet kan man föreställa sig en atom som, i stället för att alltid sitta på samma ställe i enhetscellen - den minsta byggstenen i en kristall - till synes godtyckligt flyttas bort från dess originala position. Viktigast är att den skillnaden från dess originala position är olika i varje enhetscell. Avbildar man några enhetsceller tillsammans, ser man att förskjutningen av atomerna följer ett mönster, till exempel en sinusformad våg.

Väsentligen delas den här avhandlingen in i två sektioner varav den första handlar om talliumjodidtyplegeringar (TII) och den andra handlar om tennantimons högtemperaturstruktur ( $\text{Sn}_3\text{Sb}_2$ ). Arbetet med TII-typlegeringar började med att undersöka guldindium ( $\text{AuIn}$ ), som inte kristalliserade så enkelt som man skulle förvänta sig. Termiska analyser och diffraktionsstudier vid förhöjda temperaturer påvisade en modulerad struktur som genomgick olika strukturella omvandlingar. Under arbetet med  $\text{AuIn}$ , upptäcktes också att palladiumbismut ( $\text{PdBi}$ ) och palladiumbly ( $\text{PdPb}$ ) betedde sig på liknande sätt, vilket ledde till att även deras strukturer undersöktes. Som resultat fanns tre legeringar som alla avvek på samma sätt från deras ursprungligen postulerade strukturer. Det ledde till hypotesen att det finns en hel undergrupp av strukturer som uppför sig på samma sätt.

Spännande är att högtemperaturformen av tennantimon ( $\text{Sn}_3\text{Sb}_2$ ), som man inte kan syntetisera på annat sätt, kunde syntetiseras *in situ* av  $\text{SnSb}$  och överskott av tenn direkt under mätningen. Analysen av de resulterande data påvisade en utomordentligt sällsynt aperiodisk kristallstruktur.

Det som anknyter dessa båda delar är att båda rör enkla typstrukturer som uppvisar modulation vilket man kan observera med *in situ* temperaturberoende röntgendiffraktometri.

# Lists of used Abbreviations and Symbols

## Abbreviations

ADP	Atomic displacement parameter
CCD	Charge coupled device
CCP	Cubic close packed
DSC	Differential scanning calorimetry
DTA	Differential thermal analysis
FCC	Face centred cubic
GOF	Goodness of fit
IUCr	International Union of Crystallography
Linac	Linear accelerator
PDF	Pair distribution function
PXRD	Powder X-ray diffraction
XRD	X-ray diffraction

## Structure Symbols

AuIn	Gold indium
CrB	Chromium boride
FeB	Iron boride
PdBi	Palladium bismuth
PdPb	Palladium lead
SnSb	Tin antimony
TII	Thallium iodide

## Physical Symbols

$E_F$	Fermi energy level
$R_{\text{int}}$	Internal R value
$R_{\text{obs}}$	R value over all observed reflections

# Temperature Dependent in situ Studies of two Simple Structure Types Revealing Modulation: Or The Art of making Glitter

## 1 Disclaimer

I have written and defended a Licenciate thesis in March 2018, as is common in Sweden. The Licenciate contained most of the theoretical chapters, that will be found in this dissertation, as well as the chapters about AuIn and Sn<sub>3</sub>Sb<sub>2</sub>. Since the fundamental theory behind my work did not change and the research on AuIn and Sn<sub>3</sub>Sb<sub>2</sub> are essential parts, similarities to the licenciate may well occur. Figures may simply be reused but will be cited appropriately. Even text may sometimes be reused verbatim and will also be cited appropriately. The title of chapters that are prone to show a lot of similarities to the licenciate thesis are marked with an asterisk (\*).

The licenciate thesis can be downloaded from Lund University's research portal in the research output section, [or directly here](#) [3].

## 2 Introduction\*

I should not like to leave an impression that all structural problems can be settled by X-ray analysis or that all crystal structures are easy to solve. I seem to have spent much more of my life not solving structures than solving them.

---

Dorothy Hodgkin

Following here is work that deals with two simple and fundamental structure types - sodium chloride and thallium iodide, both of which have been known for a long time. However, this thesis will detail that with certain elements and temperatures these structure types can exhibit modulation.

### 2.1 Intermetallics\*

Intermetallics are intimate mixtures of two or more distinct metals, that solidify in a different structure than their pure parent metals [4]. Preparation and search for new intermetallic materials dates back to antiquity and has been one of the driving forces for civilisation in general and chemistry in particular. With the advent of structural investigations, for example via X-ray diffraction, the vastness of chemical systems and their structure-property relationships began to be appreciated [5]. Indeed the first investigation of an intermetallic compound known to the author was executed by Kurnakov *et al.* in 1916 [6].

In recent times intermetallics are mainly sought after for their physical properties, to engineer novel materials or to understand the behaviour of materials currently in use. Based on the most cited and most downloaded articles in the Journal “Intermetallics”, the current hot topic is high entropy alloys and their physical and mechanical properties [7].

### 2.2 The Thallium-Iodide Structure Type

Lindsay Helmholz first published the thallium iodide 1:1 phase in 1936 as an orthorhombic structure with space group  $Cmcm$  and lattice parameters  $a = 4.57(2) \text{ \AA}$ ,  $b = 12.92(1) \text{ \AA}$ ,  $c = 5.24(2) \text{ \AA}$  [8]. The atomic positions in this lattice are displayed in Figure 1 and will be important for later comparisons. Noteworthy is that thallium has a much lower electronegativity than iodine and hence has the charge “+1”, also indicating that TII is an ionic compound. Hence the atoms are drawn without any inter-atomic contacts.

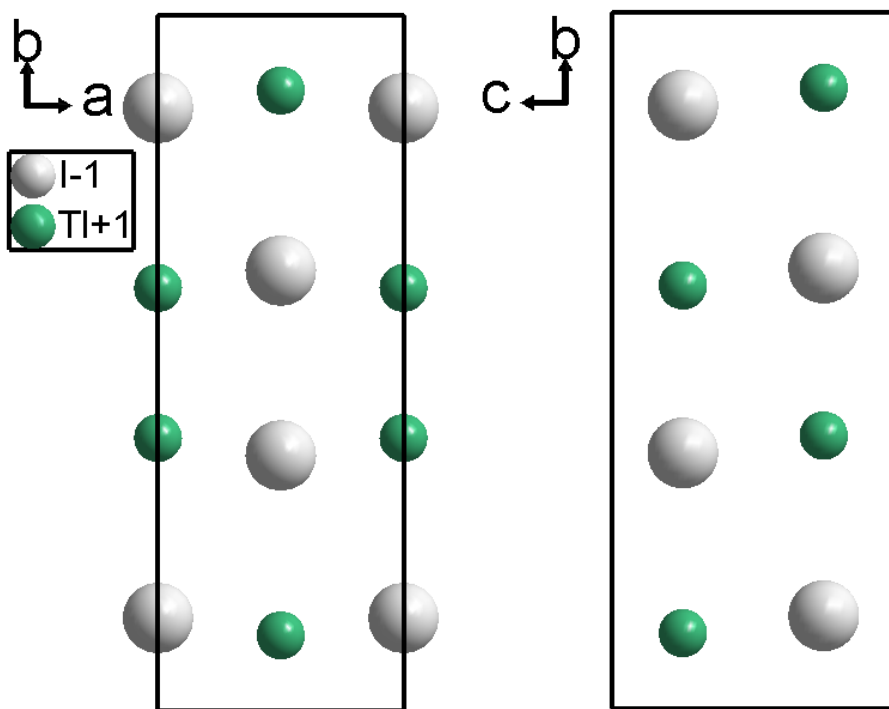


**Figure 1:** The unit cell of TII depicting the atomic arrangement looking down the  $c$ -axis (left) and down the  $a$ -axis (right). Picture adapted from [8].

Since there is a multitude of compounds crystallising with similar lattice parameters and in the same space group (a quick search of the ICSD finds 232 binary and pseudo binary structures while 63 binary and ternary borides are reported to adopt the CrB type [9]), TII has been adopted as a structure type. Due to a great similarity to the CrB structure and alloys of that structure type, the TII-type and the CrB-type have sometimes been used as synonyms [10]. The only clear difference between the TII-type and the CrB-type is that the CrB-type structures seem to have generally smaller unit cell parameters (e.g.  $a = 2.9782 \text{ \AA}$ ,  $b = 7.870 \text{ \AA}$ ,  $c = 2.9346 \text{ \AA}$  for CrB [11]). Schob and Parthé additionally identified subgroups of the TII family depending on lattice parameters and elements that constitute the respective alloy [10] (see Table 1).

**Table 1:** Table of different compositions found in TII compounds, adapted from Schob and Parthé [10]. Also note that the CrB-type borides here belong to group 1, while they are tabulated separately in the ICSD [9]

Group I	A: Alkaline earth metals or transition metals B: B, Al, Ga, Si, Ge, Sn, Pb	a/b= 0.38 a/c= 1.03
Group II	A: Alkaline earth metals or transition metals of 3 <sup>rd</sup> or 4 <sup>th</sup> group B: Transition metal of 8 <sup>th</sup> group or metal of Cu group	a/b= 0.35 a/c= 0.88
Group III	A: In or Tl B: Halogen elements	a/b= 0.36 a/c= 0.93
Group IV	A: Alkali elements B: Hydroxyl group	a/b= 0.34 a/c= 1.02

Furthermore, according to Schob and Parthé [10] groups I and II are metallic while III and IV are ionic.

Iron boride (FeB) is another orthorhombic structure type that is similar to TII. Unlike TII, it displays the space group  $Pnma$  and lattice parameters look typically like:  $a = 5.5060 \text{ \AA}$ ,  $b = 2.9520 \text{ \AA}$  and  $c = 4.0610 \text{ \AA}$  (FeB [12]). FeB and TII (CrB) both contain a trigonal prism as a common structural unit, that is built of A-type atoms and has zig-zag rows of B-type atoms in its centre. Those prisms build rows by sharing their rectangular sides, with the only difference between the TII and FeB type being the arrangement of the prism rows with respect to each other. Hence they can be graphically transformed into each other by a shift of approximately 19% along the a-b diagonal of the TII unit cell, which results in the FeB type cell (see Figure 2).

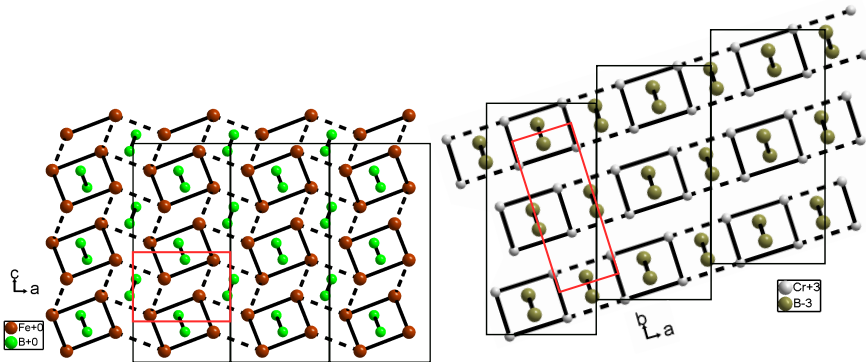


**Figure 2:** On the left an array of FeB unit cells is drawn compared to a similar array of CrB unit cells on the right. The image underlines how similar both cells are and how easily they can be transformed into each other. Image adapted from [13].

## 2.2.1 Gold-Indium\*

Gold is one of the metals, longest known to man. It has been utilised by cultures back to the stone age and it was used as money even before it was introduced as coinage [14]. In modern times, gold is a valuable catalyst for growing nanowires and a valued material for being chemically close to inert, as well as a good conductor of heat and electricity [3] [15].

Indium was discovered in 1863 by flame spectroscopy, where it showed a bright indigo blue line and hence was named after the latin word *indicum* [14]. Nowadays it is used in low-temperature solders and III-V semiconductors [3] [15] [14].

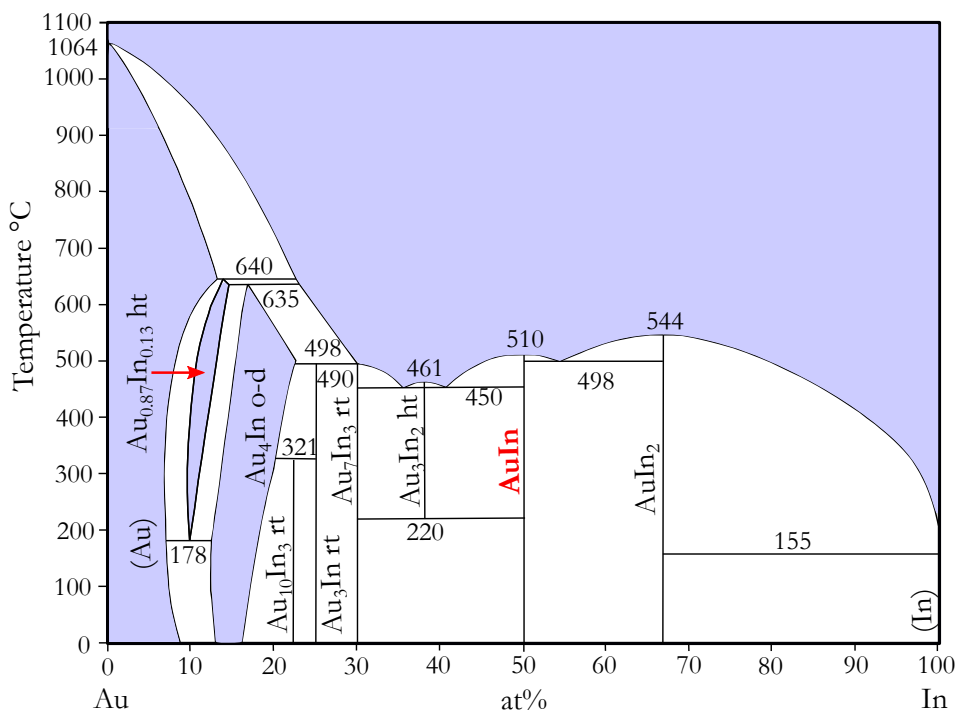


**Figure 3:** Phase diagram of AuIn, adapted from [16]. The gold indium 1:1 phase is highlighted with red writing. Also found in the Licenciate thesis [3].

According to the Inorganic Crystal Structure Database (ICSD [9]) and the Inorganic Material Database [17] all phases that can be seen in the gold indium phase diagram (Figure 3) have been elucidated, except for the 1:1 AuIn alloy. More in depth literature searches however find reports on the AuIn 1:1 structure. Most of these references claim that AuIn crystallizes in the TII-type structure with a *Cmcm* space group and measurements were either taken by powder diffraction or electron



diffraction [18–22]. Schubert *et al.* nonetheless have quite probably - the text is not clear on that - measured single crystal diffraction and even write about having seen superstructural reflections, which they subsequently ignore. Hence they find a pseudo orthorhombic structure of the thallium iodide type [18].

Another strong point that makes AuIn intriguing to study, is that intermetallic 1:1 alloys usually crystallise in very high symmetric space groups (cubic or tetragonal), whereas here an orthorhombic structure is suggested.

Gold indium alloys may be found in solder joints, where an indium containing solder is used to connect a gold component to a circuit board. In connections like those it is crucial to know the physical properties of all crystalline structures that might appear so that the stability of the joint can be estimated. An example study of unexpected solder ruptures can be found in a NASA Advisory document by H. Leidecker [23].

### 2.2.2 Palladium-Bismuth

Palladium was first described by W. H. Wollaston in 1803. He isolated it from the mother liquor that resulted after precipitating  $(\text{NH}_4)_2\text{PtCl}_6$  out of an aqua regia solution [14]. It was named palladium after the newly found asteroid Pallas, respectively the Greek goddess of wisdom, Palladion.

Bismuth alloys were used to cast type from around 1450 and the pure metal was known latest from 1480. Its name originates from the German “Wismuth”, meaning “white metal” or “meadow mines” and was latinised to *bisemutum* by G. Bauer [14].

The 1:1 alloy of PdBi has recently been found to be a noncentrosymmetric superconductor, showing a transition temperature of 3.8K [24]. However, the superconductivity appears to rely on a slight understoichiometry of Bi which might explain why this thesis finds the PdBi structure to be centrosymmetric instead (See section 5.2). Moreover PdBi is used as a catalyst on N-doped graphene for the oxidation reaction of formic acid [25]. In both of these applications knowledge of the crystal structure of PdBi can enable strategic process design optimisation.

The first report of PdBi was published by Zhuravlev in 1957, where he found the space group  $Cmc2_1$ , which is rather low in symmetry for a 1:1 intermetallic compound [26]. A more recent publication by Bhatt *et al.* finds the space group  $P2_1$  which is even lower in symmetry [27]. This report also states that at 210°C it transforms into a high temperature TII type structure through a displacive phase transition, which is also indicated in the phase diagram in Figure 4.

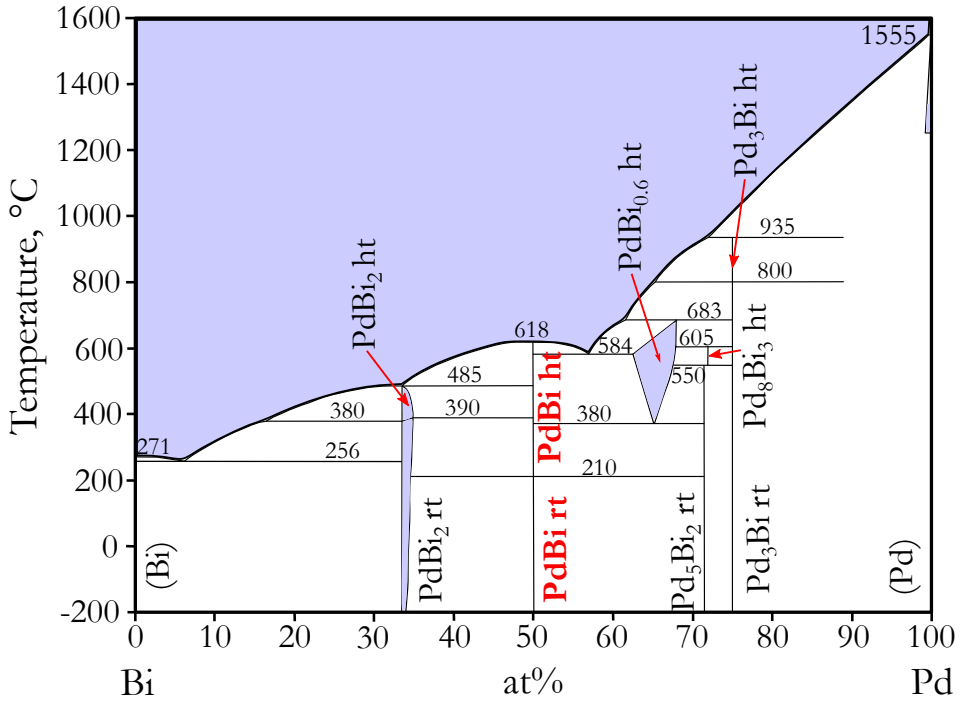
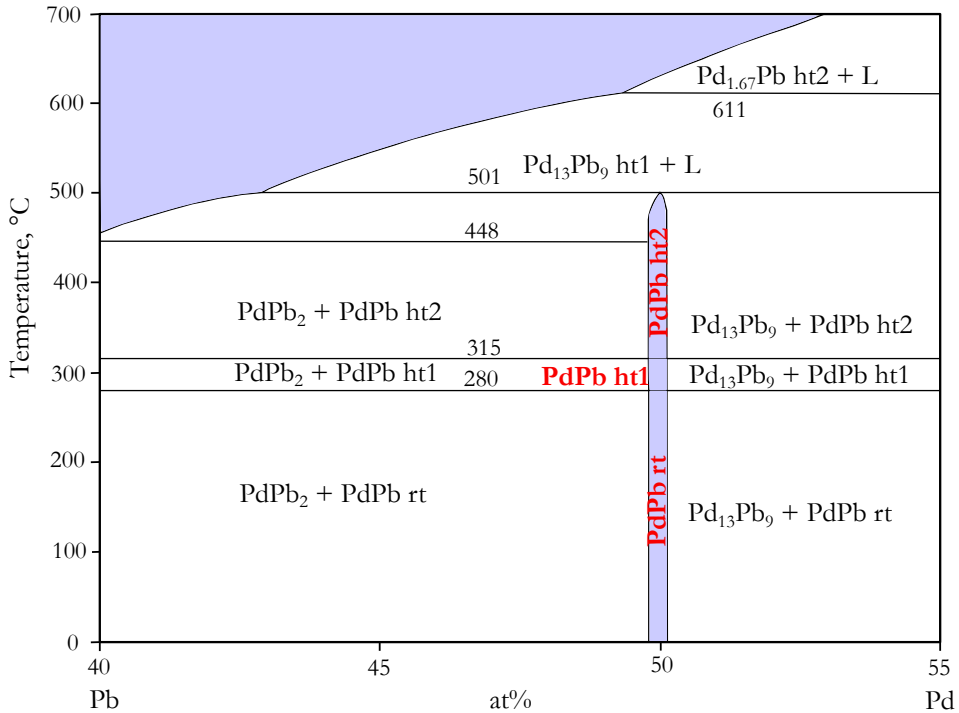


Figure 4: Phase diagram of Pd and Bi adapted from [28], with the PdBi 1:1 phase highlighted in red. Notice that in a slightly palladium-rich environment phase transformations can be found at 210°C, 380°C and 584°C.

### 2.2.3 Palladium-Lead

Lead also belongs to the group of metals known to man since archaic times and was used by the ancient Egyptians for glazing pottery and by the Romans for water-pipes and plumbing. Its chemical symbol originates from its Latin name *plumbum* and it is recognised as a heavy-metal poison, affecting *inter alia* the haem synthesis in the body [14].

As can be seen in the phase diagram of PdPb (Figure 5) the 1:1 phase of PdPb has a small phase width around 50 at%. In addition, two phase transformations are shown at 280°C and at 315°C. Above 501°C PdPb ht2 peritectically decomposes into Pd<sub>13</sub>Pb<sub>9</sub> and liquid. The publication discussing this phase diagram indicates that PdPb, just like PdBi, is part of a family of “displacive variants of TII” [29]. Moreover the above reported phase transformations are stated to be unquenchable and only the room temperature structure of PdPb could be further investigated. This structure shows the space group  $F\bar{1}$  with lattice parameters  $a = 7.152 \text{ \AA}$ ,  $b = 8.519 \text{ \AA}$ ,  $c = 42.38 \text{ \AA}$ ,  $\alpha = 90.06^\circ$ ,  $\beta = 90.42^\circ$ ,  $\gamma = 89.80^\circ$ .



**Figure 5:** The phase diagram of Pd and Pb between 40 and 55 at% of Pd is shown, with the PdPb 1:1 phase highlighted in red. As can be seen, this phase diagram indicates two structural transformations in PdPb at elevated temperatures. Diagram adapted from [29].

### 2.3 The NaCl Structure Type

Rock salt or sodium chloride has been known to man since a very long time and its structure has been elucidated before the end of the 19<sup>th</sup> century (oldest reference found by the author is by W. H. and W. L. Bragg from 1913, where NaCl was used as a reference standard [30]). The ICSD data base finds over 3800 entries of binary or pseudo binary compounds with the NaCl structure [9], making this one of the most common structure types known. Enticing is furthermore the simplicity of this structure type, as it is built from two atoms only, which are arranged in a face centred cubic (fcc) fashion with all octahedral voids filled and tetrahedral voids empty (see Figure 6). In NaCl the anion ( $\text{Cl}^-$ ) is making the close packing array, while the cation ( $\text{Na}^+$ ) sits in the octahedral voids. With this arrangement every Na atom is surrounded by six Cl atoms and every Cl atom is surrounded by six Na atoms, resulting in a network of edge sharing octahedra. This kind of arrangement is also called “cubic close packed”(ccp), filling 74% of space, *i.e.* the highest percentage possible to fill with spheres [31]. The structure type is mostly adopted by ionic com-

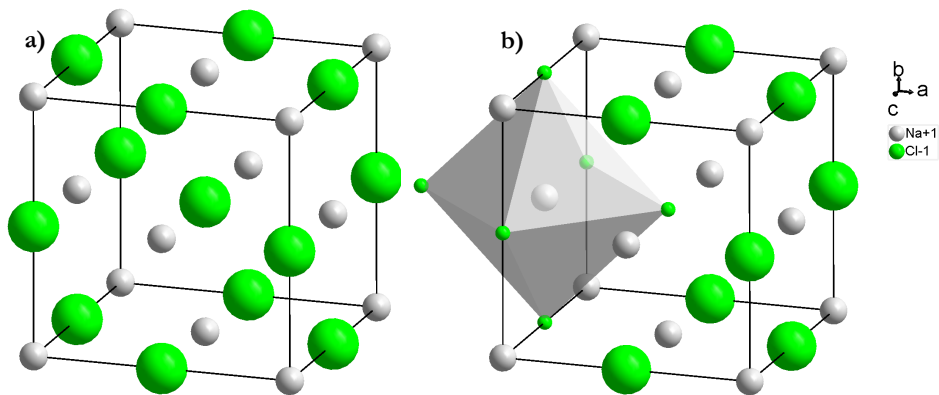


**Figure 6:** The left side of this image shows the NaCl unit cell where the green spheres are Na and the gray spheres are Cl. The right side shows the same unit cell with an octahedron indicating that Na fills the octahedral voids in this structure. Pictures adapted from Swanson *et al.*. [33]

pounds like halides and hydrides of the alkali metals but also by metallic or covalent compounds [32].

### 2.3.1 Tin-Antimony\*

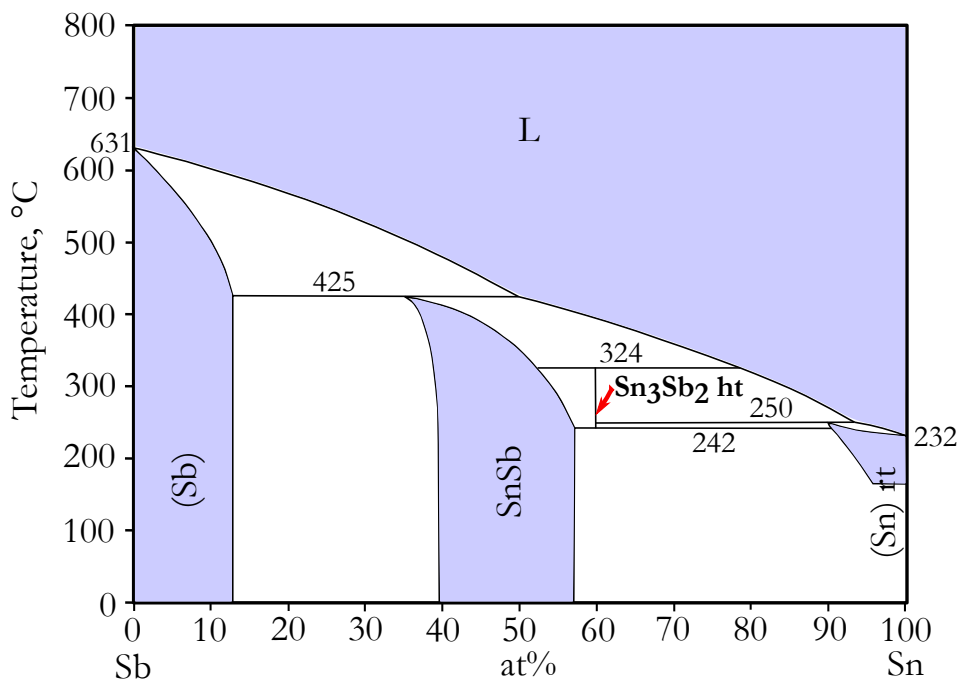


**Figure 7:** SnSb's phase diagram according to [34] is displayed. The here discussed high temperature structure  $\text{Sn}_3\text{Sb}_2$  is indicated by a red arrow. Also found in the Licenciate thesis [3].

Tin and antimony are both post-transition metals with pure tin and compounds of antimony being known since ancient times [14] [15]. While tin is non-toxic, pure antimony powder and some antimony compounds show effects on human health [35].

Recently a study on the alloys featured in the Sn - Sb phase diagram has been published [36], discussing the whole range of alloys including  $\text{Sn}_3\text{Sb}_2$ , which is marked with a red arrow in the phase diagram in Figure 7. The  $\text{Sn}_3\text{Sb}_2$  structure undergoes an unquenchable phase transition as soon as its temperature is lowered below 250°C, and hence is only accessible with great difficulty. How to obtain data of this alloy and its crystal structure will be discussed in chapter 2.3.1.

The other mixed compounds range from 35.6 at% Sn to 54.1 at% Sn and thus have the stoichiometries  $\text{Sn}_9\text{Sb}_{11}$ ,  $\text{SnSb}$ ,  $\text{Sn}_3\text{Sb}_2$  and  $\text{Sn}_5\text{Sb}_2$ . All of those structures can be described in the rhombohedral incommensurate  $R\bar{3}m(00\gamma)$  space group with the  $\gamma$  component of the q-vector depending on the tin concentration of the respective crystal. This dependence can be expressed by the following formula [36]:

$$\gamma = \frac{3}{2} \left(1 - \frac{[\text{Sn}]}{4}\right) \quad (1)$$

While pure antimony has been reported to show the  $R\bar{3}m$  space group [37], it can also be described as a commensurate modulation in the structure used for the other Sn - Sb samples. Both descriptions lead to the structure shown in Figure 8 a. The displayed Sb network can be characterised as a distorted cubic network, with inter layer contacts having either been shortened or elongated along the c-axis.

Once a high enough amount of Sn is added, blocks appear which contain seven alternating layers of tin and antimony, mimicking a NaCl-type structure. Those blocks begin and end with a layer of Sn and are interleaved by a certain amount of pure Sb layers (see Figure 8 b). At a relatively high Sn content double layers of Sb are alternating with double blocks of NaCl-type (see Figure 8 c). Figure 8 d shows the structure of the most Sn rich phase, where one seven layer block meets the next without interleaving Sb layers.

Diffraction data of the sample which formed from the synthesis of ht- $\text{Sn}_3\text{Sb}_2$  exhibiting twinning and extra reflections originating from pure  $\beta$ -Sn [36] is shown in Figure 9.

The extra reflections of  $\beta$ -Sn are a strong indicator that at higher temperatures a structure was present that contained a larger amount of tin. Therefore those reflections would corroborate that  $\text{Sn}_3\text{Sb}_2$  was present, which decomposed to  $\text{SnSb}$  and  $\beta$ -Sn. Furthermore the twinning patterns seen in  $\text{SnSb}$  and  $\beta$ -Sn mimic a cubic pattern, implying that both originate from a cubic structure.

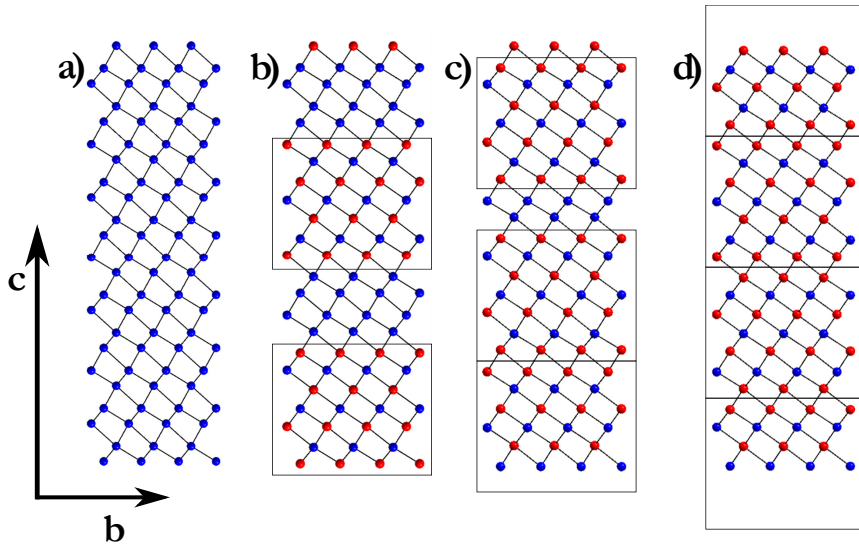


**Figure 8:** Structures from the phase diagram of Sn and Sb, all being built of NaCl-type seven layers interrupted by a varying amount of Sb. Sb is coloured blue, while Sn is coloured red. a) Pure Antimony. b)  $\text{Sb}_2\text{Sn}$ . c)  $\text{SbSn}$ . d)  $\text{Sb}_3\text{Sn}_4$ . Picture taken from [36]. Also found in the Licenciate thesis [3].

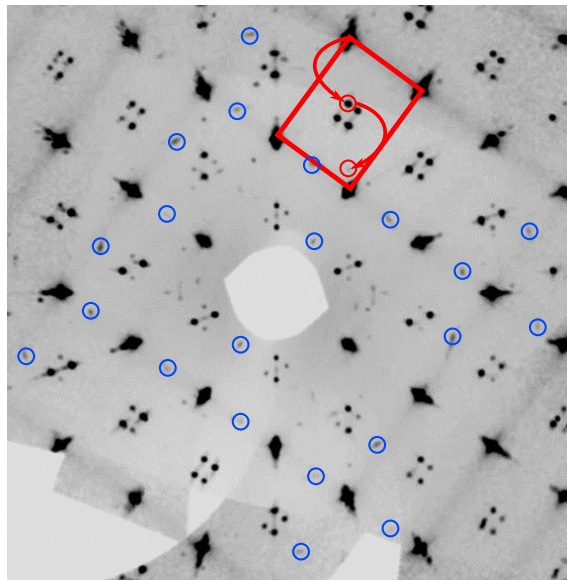


**Figure 9:** Diffraction image of  $\text{Sn}_3\text{Sb}_2$  quenched to room temperature, with blue circles marking reflections from  $\beta$ -tin, red circles marking first and second order satellites and the red rectangle indicating the unit cell. Image by courtesy of Sven Lidin [36]. Also found in the Licenciate thesis [3].

## 2.4 Short Overview of 3D Crystallography\*

With Max von Laue's publication on the diffraction of X-rays by zinc blende, the interest of William and Lawrence Bragg, father and son, was sparked. Shortly thereafter at a meeting of the Cambridge Philosophical Society, they presented their paper "The Diffraction of Short Electromagnetic Waves by a Crystal" in which they declare their famous equation in its early form of:  $\lambda = 2d\cos(\theta)$ . In this version of the equation, theta is the complement of the  $2\theta$  angle that is used in the modern version of the Bragg equation [38].

The International Union of Crystallography (IUCr) defines a crystal as a material that "[...] has essentially a sharp diffraction pattern. The word essentially means that most of the intensity of the diffraction is concentrated in relatively sharp Bragg peaks, besides the always present diffuse scattering. [...]" [2]. A sharp Bragg peak arises under the condition that a family of lattice planes in the crystal lies in the correct angle with respect to the incident beam, *i.e.* so that the diffracted rays interfere constructively. More precisely this is formulated by the Bragg equation:

$$n\lambda = 2d\sin(\theta) \quad (2)$$

Where  $n$  is the order of diffraction,  $\lambda$  is the wavelength,  $d$  is the spacing between two lattice planes and  $\theta$  is the incident angle [39]. Graphically this is illustrated by the Ewald construction in Figure 10 a, respectively an enlarged version showing only the geometrical interaction of the X-rays with the lattice planes can be seen in Figure 10 b. Note however that lattice planes are again constructions to help the understanding of scattering theory, in reality the X-rays are scattered by the electron cloud around the atoms.

The resulting diffraction pattern is then indexed and integrated. By indexing a diffraction pattern the positions of the Bragg reflections are used to calculate the lengths and angles of lattice parameters ( $a, b, c, \alpha, \beta, \gamma$ ) and to assign one of the 14 Bravais lattices to it.

Integration treats the intensity of the reflections. The intensity of Bragg reflections gives insight to the elements contained in a crystal, as it is equal to the absolute value of the square of the structure factor ( $F_{hkl}$ , Eq. 3). This in turn is the vector sum of the single atom form factors ( $f_n$ ) and their phases ( $\Phi = 2\pi[hx_n + ky_n + lz_n]$ ) (Fig. 11), which are element specific and tabulated in the International Tables for Crystallography [40].

$$F_{hkl} = \sum_n f_n \exp(i2\pi[hx_n + ky_n + lz_n]) \quad (3)$$

$$\rho(x, y, z) = \frac{1}{V} \sum_{hkl} F_{hkl} \exp(-2i\pi[hx + ky + lz]) \quad (4)$$



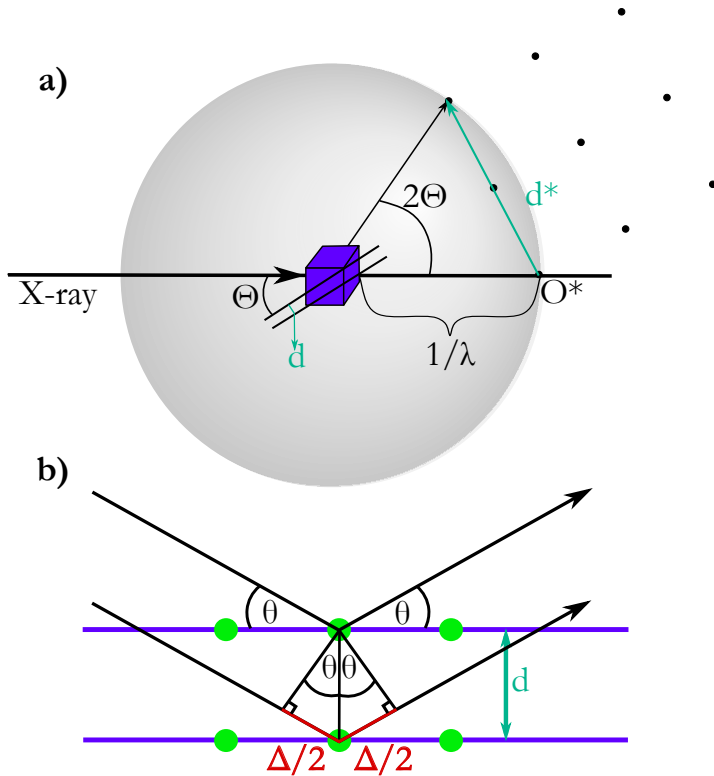


**Figure 10:** a) The Ewald construction illustrates how an incident X-ray beam is scattered by the lattice planes in a crystal (purple cube) and the resulting diffraction spots land on a spherical surface. Also found in the Licenciante thesis [3]. b) Zoomed graphic of the diffraction of an X-ray beam on two lattice planes. Highlighted in blue and labelled with  $\Delta/2$  is the path difference and the green circles indicate atoms sitting on the lattice plane. If the two outgoing rays interfere constructively, a Bragg spot will appear on the detector.

Therefore it should be relatively straight forward to calculate the electron density from the measured intensity. However, since the intensity is the *absolute value of the square* of the observed structure factor, the phase can not be recovered. This constitutes the most central problem in crystallography and is called the “Phase Problem”. Consequently, the main task of most structure solution programs is to find a reasonable set of initial phases. Commonly programs start by assigning random phases to the structure factors and converting the result into electron density. The resulting calculated electron density ( $\rho_{calc}$ ) can then be optimised until the difference between observed ( $\rho_{obs}$ ) and calculated ( $\rho_{calc}$ ) electron density is small.

To optimise  $\rho_{calc}$  a number of parameters of the motif can be changed. Among them are: atomic positions, atomic displacement parameters (ADP), twinning, extinction and occupancy. To give the quality of match between model and measure-

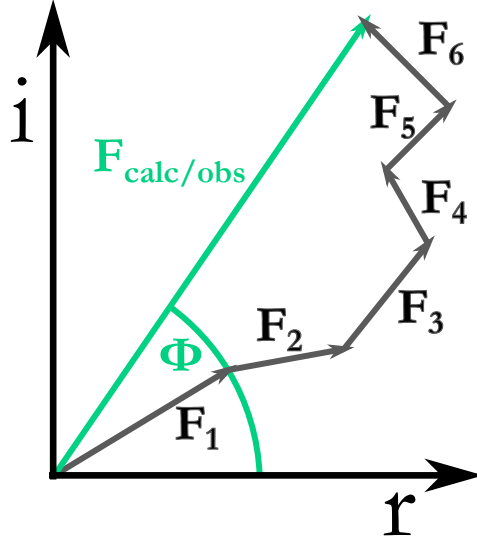


**Figure 11:** A real ( $r$ ) versus imaginary ( $i$ ) space plot, depicting the single atomic form factors adding up to the observed or calculated structure factor  $F_{calc/obs}$ . The form factors are element specific and originate from the atom positions in the unit cell. Indicated by  $\Theta$  is the phase of the structure factor, which cannot be recovered from experimental data due to  $I = |F|^2$ . Also found in the Licenciate thesis [3].

ment a number, the so called “R-factor” is used, that is calculated from  $F_{obs}$  and  $F_{calc}$  (see Equation 5).

$$R = \frac{\sum_{hkl} ||F_{obs}| - |F_{calc}||}{\sum_{hkl} |F_{obs}|} \quad (5)$$

The above discussion mainly focused on the treatment of single crystal data. If a powder diffraction study is conducted as finger printing method, the resulting data is treated as described next:

In a fingerprinting scenario, indexation and integration are skipped and the measured pattern is directly refined against a reference pattern. This reference pattern is chosen by the operators assumption on what phases the measured pattern contains, optical comparison to theoretical patterns or search - match algorithms in respective programs. The lattice parameters ( $a, b, c, \alpha, \beta, \gamma$ ) and space group of the reference pattern are used as starting points for the so called “Le Bail decomposition”. With a least squares algorithm the initial values are adjusted until the powder pattern calculated from those values is as close as possible to the measured pattern. Further parameters that can be refined but do not have starting values from a theoretical pattern are *inter alia*: back ground parameters, peak shape function parameters and shift parameters. Note that a Le Bail decomposition does not account for atomic positions and hence only peak positions and not peak intensities are treated. The quality of the

resulting fit is indicated, as for single crystal diffraction, with the “R-factor” introduced in equation 5.

As many powder patterns comprise more than one phase it is quite usual to add more than one literature pattern to the collection of parameters to be refined. Here it is however recommendable to not refine all possible values at the same time, since correlations between the individual values can make refinements unstable.

## 2.5 Introduction to Higher Dimensional Crystallography\*

The main difference between aperiodic and periodic structures is that the former - as indicated by their name - do not show lattice periodicity. Nonetheless, they do show a sharp diffraction pattern, as those structures still have long range order. Moreover they even feature additional reflections, called satellites. Satellites sit at coordinates in the reciprocal lattice, that have at least one non-integer Miller index. Their position can be described by  $(h+\sigma_1, k+\sigma_2, l+\sigma_3)$ , where  $(\sigma_1, \sigma_2, \sigma_3)$  are the vector components in reciprocal space of the so called  $q$ -vector.

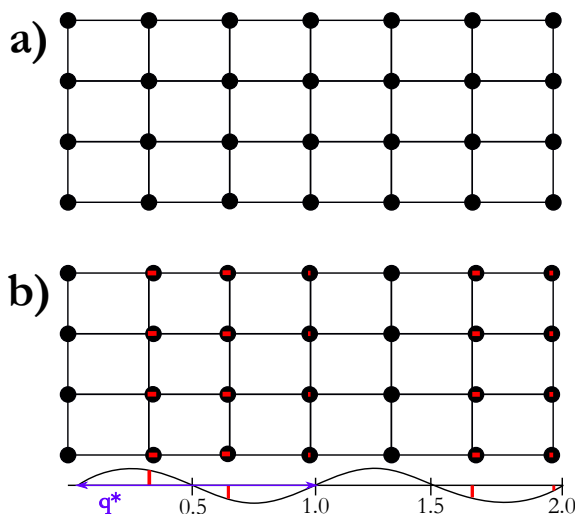


**Figure 12:** a) Depiction of a 3x6 periodic lattice. The black circles denote atomic positions. b) Here the atoms were moved away from their original positions by a distance that is never exactly the same in two unit cells. The purple double arrow shows the  $q^*$ -vector in this lattice, which determines the length of the modulation wave. Picture adapted from [41] and also found in the Licenciate thesis [3].

As shown in Figure 12 the  $q$ -vector determines the length and direction of the modulation wave. In addition the amplitude of the wave determines how much the modulation changes the underlying basic structure. Any descriptor of the motif may show modulation: positional modulation, where the amplitude determines how far

the atom is displaced from its average position; occupational modulation, where the amplitude indicates the amount of occupation on an atomic position and modulation of the ADP parameters which changes the temperature ellipsoids on atoms in different amplitude over the course of various unit cells. Mathematically, modulation can be expressed as follows [41] :

$$\bar{x}_4 = t + q \cdot \bar{x} \quad (6)$$

$$u_i^\mu(\bar{x}_4) = \sum_{n=1}^{\infty} A_i^n(\mu) \sin(2\pi n \bar{x}_4) + B_i^n(\mu) \cos(2\pi n \bar{x}_4) \quad (7)$$

Equation 6 shows the connection of the argument of the modulation function ( $\bar{x}_4$ ) to the q-vector, the initial phase t and the structural position of the atom in the average structure  $\bar{x}$ .  $u_i^\mu(\bar{x}_4)$  in Equation 7 denotes the modulation function itself, with A and B being the Fourier amplitudes, n being their order and  $\mu$  labelling the atom under consideration.

In a more visual way the q-vector can be imagined as an additional axis of the coordinate system, turning a three dimensional space into a 3+1 dimensional space. It should however be clearly emphasised that dimensions being added by q-vectors, is a purely mathematical concept and has no counterpart in the physical world.

Depending on the evidence in the diffraction pattern, some indexing might require more than one q-vector. However structures featuring two q-vectors ((3+2)D) are rare and structures featuring three q-vectors ((3+3)D) are absolutely scarce [42].

With the additional dimensions, the understanding of atoms also changes. While in the standard 3D world atoms are thought of as zero dimensional points, in higher dimensions they become lines ((3+1)D), surfaces ((3+2)D) or volumes ((3+3)D). This is depicted in Figure 13, where **R** indicates the axis which groups the real space axes together. Note that the q-vector(s) stand(s) orthogonal to the real space axes.

There exist a handful of programs allowing for the refinement of modulated structures and for this thesis the program of choice is JANA2006 [43]. To conduct an aperiodic refinement, together with the basic structure, the number and type of modulation waves are refined. The number of modulation waves that can be used depends on the order of reflections found in the diffraction pattern, while the type of modulation function is one of the three above mentioned positional, occupational or ADP or various combinations thereof. Likewise the modulation function itself does not necessarily need to be of sinusoidal shape as implied by equation 7. Saw-tooth or block waves are also supported by the program JANA2006 and other forms can be scripted if required. Which kind of function to use is best spotted by inspecting an  $x_4$  vs  $x_n$  ( $n = 1, 2, 3$ ) electron density plot of the atom in question.

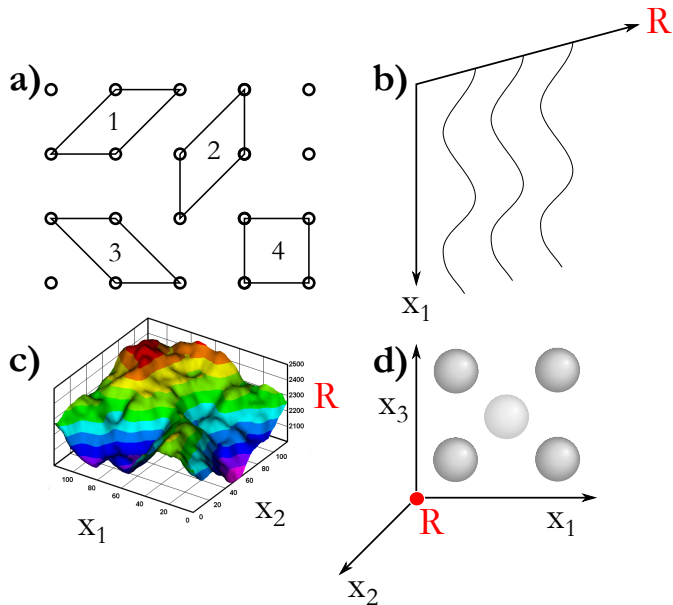


**Figure 13:** a) Depiction of atoms in three dimensions as zero dimensional dots. Figure taken from [39]. No red R is shown in this part, as only real space is depicted. b) In (3+1)D atoms are thought of as lines. c) In (3+2)D atoms are imagined as surface areas stretching the over the two additional dimensions. (Plot adapted from: [44]) d) In (3+3)D atoms are three dimensional volumes, containing another 3D volume at each infinitesimal point in space. Also found in the Licenciate thesis [3].

## 2.6 The 3D- $\Delta$ Pair Distribution Function

The 3D- $\Delta$  pair distribution function (PDF) is applied to understand and model diffuse scattering in single crystal measurements.

The function itself is the Fourier transformation of all the diffracted intensity, which is called a total 3D-PDF and includes Bragg diffraction intensity; or alternatively of all the diffracted intensity *minus* the Bragg diffraction intensity, which then is called 3D- $\Delta$ PDF. A Fourier transformation of the Bragg diffraction intensity without any phase information is also known as the Patterson function. It results in maxima that emerge from the origin of the Patterson map and correspond to endpoints of interatomic vectors. Thus a Patterson map shows all interatomic distances between each atom in the unit cell  $m$  with each other atom  $n$  and itself. This makes the Patterson function an autocorrelation function of the average crystal.

The Pair distribution or total scattering function is also an autocorrelation function and hence the difference of the two can be calculated, leaving behind only the Fourier transformed diffuse scattering intensity. Conveniently this shows only features of the real structure, that have not yet been represented by the average structure, also result-

ing in a smaller general amount of peaks in the PDF space.

Positive 3D- $\Delta$  PDF peaks indicate that the probability of finding scattering densities with the respective distance is higher than in the average structure, while negative 3D- $\Delta$  PDF peaks indicate that the probability of finding scattering densities with the respective distance is lower than in the average structure [45].



### 3 Motivation and Hypothesis

The best and safest method of philosophising seems to be first to inquire diligently into the properties of things, and establishing those properties by experiments, and then to proceed more slowly to hypotheses for the explanation of them.

---

Isaac Newton

Both of the here discussed compound groups relate to structure types that are very simple. Thallium iodide in the case of AuIn, PdBi and PdPb, and sodium chloride in the case of Sn<sub>3</sub>Sb<sub>2</sub>. Structures as simple as this usually have a straightforward crystallisation procedure, which results in large, high quality single crystals. This is however not the case for AuIn and its relatives PdBi and PdPb, nor for Sn<sub>3</sub>Sb<sub>2</sub>.

AuIn additionally corroborates that its solid structure is under some sort of strain by undergoing amorphisation upon grinding. Moreover AuIn and PdBi show two endothermic but only one exothermic peak in their differential thermal analysis (DTA) curves (see Figure 14 for an example of a DTA measurement of AuIn). A pattern like this can indicate that these compounds contain a substructure that does not form from the melt. The impossibility to form from the melt can originate from a phase transformation that is diffusion free, *i.e.* so fast that it is unquenchable.



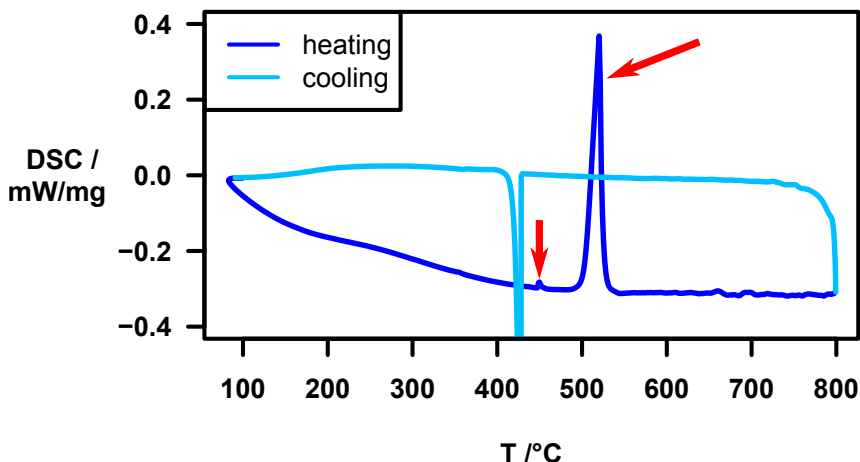


Figure 14: DSC of AuIn with red arrows indicating the two endothermic peaks, where the one lower in temperature indicates the melting of a superstructure. Also found in the Licenciate thesis [3].

A paper by Lidin *et al.* [36] reveals that  $\text{Sn}_3\text{Sb}_2$  undergoes a non quenchable phase transformation to twinned rhombohedral stistaite and pure tin. This transformation happens instantly at the precise moment when the temperature of the crystals is lowered below  $250^\circ\text{C}$  (see Sn-Sb phase diagram in Figure 7), which can only occur due to fast structural dynamics. Likewise the instantaneous loss of tin indicates short diffusion pathways in the sample.

As discussed above, both groups of compounds exhibit non trivial crystal structures and undergo fast structural dynamics with unquenchable phase transitions. In the quest to access the structures before the transformation and understand what happens during the transformations, the following hypotheses were formed:

- While based on simple structure types, the compounds discussed below show more intricate crystal structures than previously expected.
- A large portion of the structural information in the here discussed compounds can only be probed with temperature dependent *in situ* measurements.
- *In situ* high temperature measurements enable the studies of fast phase transformations of intermetallic compounds.

## 4 Used Techniques\*

Big bada boom

---

Leeloominaï Lektariba  
Lamina-Tchai Ekbat De Sebat

### 4.1 Synthesis

In all cases the pure metals were used as starting materials.

Table 2: Specifications of the used materials.

Metal	Description
Au	Used from unlabelled container
In	ABCR, 99.999%
Pd	Alfa Aesar, -22 mesh, 99.995%
Bi	KEBO, min. 99.8%
Pb	British Drug Houses (BDH)
Sn	Kistner, min 99.7%
Sb	ABCR, shot, 99.999%

For the thallium iodide phases, equiatomic amounts were weighed into a quartz ampule. The quartz ampule was evacuated, sealed off and placed in a muffle furnace for homogenisation at  $T_{\text{hom}}$  (see Table 3). Furthermore all samples were annealed in two steps at  $T_{\text{a1}}$  and  $T_{\text{a2}}$  (Table 3, for an image of such an ampule see Figure 16). Afterwards the product was quenched into air and the resulting ingot could be cracked open with a pellet press. Crystals could be found in the resulting crumble.

The annealing temperatures were chosen with the help of the respective phase diagrams and differential scanning calorimetry (DSC) measurements. For the respective phase diagrams see chapters 2.2.1 (AuIn), 2.2.2 (PdBi) and 2.2.3; and for the respective DSC or DTA measurements see 5.1 (AuIn), 5.2 (PdBi) and 5.3 (PdPb).

Table 3: An overview of the homogenisation and annealing steps used for the synthesis of AuIn and PdBi single crystals.

Sample	$T_{\text{hom}}$ [°C]	$T_{\text{a1}}$ [°C]	$T_{\text{a2}}$ [°C]
AuIn	1000	400	200
PdBi	800	580	200

If samples were produced for powder diffraction, ideally the ingot had been ground into a powder between  $T_{\text{hom}}$  and  $T_{\text{a1}}$ . As grinding induces a certain amount of

thermal energy into the material, in these phases, it results in amorphisation of the structure.

The sample for PdPb was prepared in the same fashion as the other TII samples, but followed a slightly different tempering route according to Mayer and Schubert [29], which is illustrated in Figure 15:

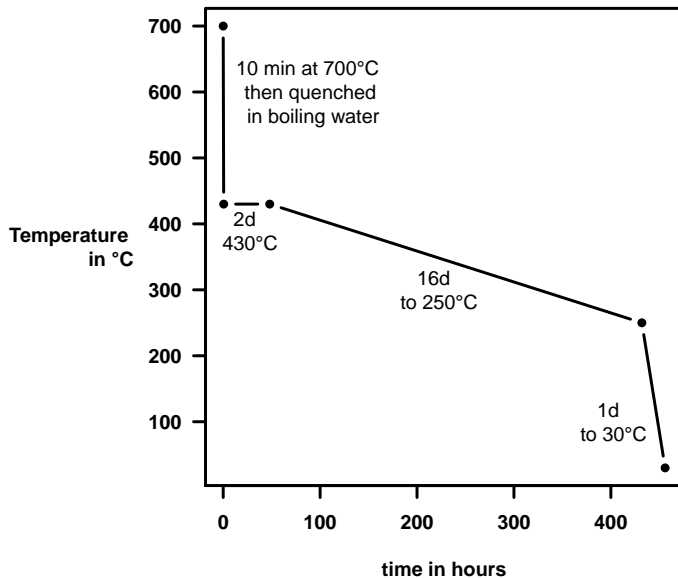


Figure 15: Diagram showing the annealing temperatures used for production of PdPb single crystals.



Figure 16: Example of a quartz ampule with a synthesised ingot inside.

Samples of  $\text{Sn}_3\text{Sb}_2$  were produced according to the procedure described in Lidin et. al. [36]. As tin was used not only as a reactant but also as a solvent, Sn was added in overstoichiometry (20 at% Sb, 80 at% Sn). Additionally quartz wool and quartz shards were added. The respectively filled quartz tubes were evacuated, sealed off and placed into a muffle furnace for homogenisation at  $690^\circ\text{C}$ . Before they were left for annealing at  $300^\circ\text{C}$ , the quartz tubes were placed in a larger iron centrifugation tube, stuffed with quartz wool. After the last annealing step, the tubes were turned upside down and centrifuged immediately at 1000 rpm for ten minutes to separate the excess amount of tin before it solidified. This resulted in separation of the excess tin and single crystals could be found sitting on top of the quartz wool inside the evacuated tube (See Figure 17 for an example).



**Figure 17:** Example of a quartz ampule containing (from left to right) crystalline sample, quartz wool, quartz shards and excess tin.

## 4.2 Thermal Analysis

Thermal analyses are an essential part of this thesis and were used to understand and locate the phase transitions in the alloys described below.

A thermal analysis is generally defined as the measurement of chemical or physical properties as a function of temperature. The two techniques employed here are DTA, which measures the temperature difference between a sample and an inert reference, and DSC which quantitatively measures the occurring enthalpy changes.

For DTA, the sample holder containing the sample and the empty reference sample holder are heated in the same chamber (Figure 18). Thermocouples record the net voltage output which only deviates from zero if the sample temperature either rises quicker than the reference (exothermic) or stops raising for a finite amount of time (endothermic). In the following work an exothermic peak usually indicates crystallisation and an endothermic peak indicates melting of a compound.

DSC measurements use the same setup with a slightly different design of the sample

chamber. Some setups measure the extra heat that needs to be put into the sample or the reference to maintain both at the same temperature, while others work exactly the same as DTA, but measure the calorimetric response of the slightly different sample chambers [32].

The instrument used for both experiment types in this thesis was a NETZSCH STA 449 F3 Jupiter with a silicon carbide furnace ( $T_{\max} = 1550^{\circ}\text{C}$ ) and crucibles made of aluminium oxide. Measurements were taken with argon as protective and purge gas.

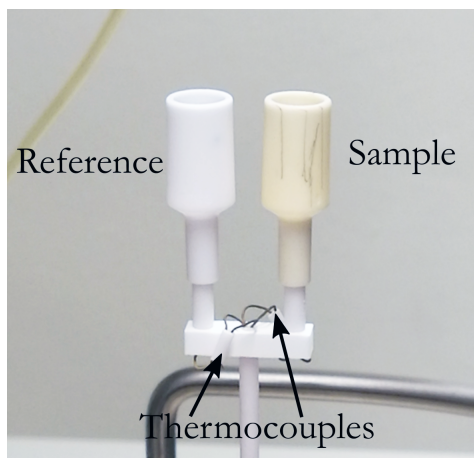


**Figure 18:** A photograph of the setup of the reference crucible and the sample crucible as used in the DTA setup. Indicated are also the two thermocouples under the respective crucibles.

### 4.3 X-ray Sources

In this thesis, two types of X-ray sources were used, of which one is a sealed tube and the other one a synchrotron source.

A sealed tube produces radiation by applying a voltage of 30 - 60 kV to a cathode resulting in electrons that bombard a highly pure metal target made of copper or molybdenum. This prompts electrons to be expelled for example from the K-shell, which in turn triggers an electron from a higher shell (for example the L-shell) to fall down to fill the gap and thereby releasing X-ray photons of a defined wavelength. Due to the selection rules and the energy level opening in the L-shell, the emitted radiation is a  $K_{\alpha 1}$ ,  $K_{\alpha 2}$  doublet. Additionally, the kinetic energy of the electrons slowing down on the target is partially converted into the so called “Bremsstrahlung”. Figure 19 shows the typical wavelength spectrum of a molybdenum tube, which generates a wavelength of  $\lambda \approx 0.71 \text{ \AA}$ .

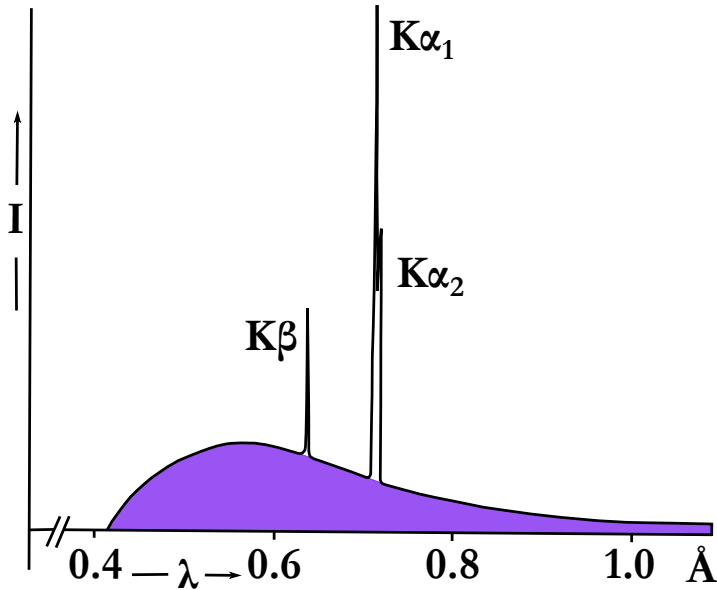
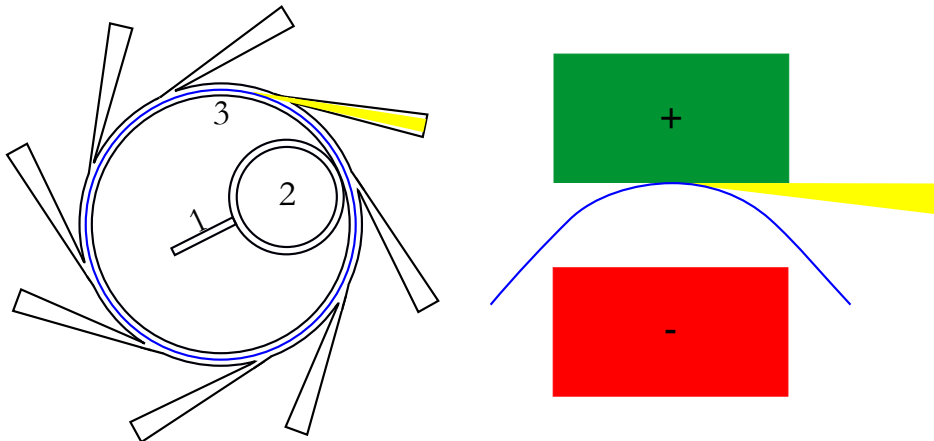


**Figure 19:** Plot showing the typical spectrum of a molybdenum X-ray tube, with the purple shaded area indicating the “Bremsstrahlung”. Figure taken from [39]

The so produced radiation passes through beryllium windows and is then monochromated by a graphite crystal monochromator (there exist also germanium crystal monochromators and other types for example mirrors or filters, which however are out of the scope of the thesis), to filter out the additional “Bremsstrahlung” and  $K_{\beta}$  radiation.

In a synchrotron, electrons are generated in an electron gun, accelerated in the so called “Linac” (linear accelerator), fed into an accelerator ring, and finally into a large storage ring, where they cycle close to the speed of light (see Figure 20). To keep the electrons on the circular path, bending magnets are placed at regular intervals around the storage ring. When electrons are bent by a magnetic field, their trajectory is changed and they also emit photons tangential to their path. Other magnetic structures found in a storage ring are the so called “undulators” or “wigglers” which are series of magnets that send the electrons on a sinusoidal path, generating radiation with an even higher brilliance than bending magnets [46]. The stability of the incident beam in a synchrotron is time dependent and decays gradually due to electron losses. To prevent a too weak beam, electrons are replenished into the storage ring at set intervals of time, some synchrotrons continuously feed electrons into the system, while others have two replenishment times a day [47].



1 Linac, 2 Accelerator Ring, 3 Storage Ring

**Figure 20:** a) Schematic of a synchrotron. Electrons are produced in the Linac, accelerated in the accelerator ring and then injected in the storage ring. From there the actual beamlines lead the photons out in a tangential trajectory. b) Schematics of a bending magnet. The blue line shows the trajectory of the electrons, perpendicular to which the photons are ejected. Also found in the Licenciate thesis [3].

The beam line hutches are located downstream from the respective magnetic structures, where the first hutch after the storage ring contains the beam line optics. Those optics monochromate and focus the beam by using monochromator crystals, X-ray mirrors, slits and filters [46]. Most of the equipment is fixed when the beam line is built, but some beam lines allow changes of the employed wavelength by slight readjustment of optical parts or magnets in the storage ring. With the respective wavelength set, the beam can be lead into the experimental hutch, where it hits the sample and the diffracted rays are captured by the detector. Note that the electrons and photons travel in ultra high vacuum within most of the synchrotron to prevent them from scattering in air.

Synchrotron sources come with many benefits compared to a laboratory source, the first of them is that they have an about ten orders of magnitude higher brilliance. Brilliance is defined as the photon flux per irradiated angle area and determines the smallest spot onto which an X-ray beam can be focused [46]. Reasons for the brilliance being so much higher at a synchrotron are that they have a much higher photon flux and much better focusing optics. Since the synchrotron radiation is more intense, the beam can also be better monochromated. This high quality beam also allows for measuring smaller sample specimens than an in house diffractometer does. Most importantly for the research below is that a lot of beam lines also offer the option of changing the employed wavelength according to specific requirements. Furthermore synchrotron beam lines are usually equipped with excellent, highly sensitive detectors

and very precise goniometer stages. These features allow for much faster measurements that still result in more and higher quality data, also featuring higher resolution compared to an in house diffractometer. Moreover synchrotron setups often allow for measurements at non-ambient conditions. For the case of the later discussed studies, this comprises the possibility to measure higher orders of satellite reflections, that are better distinguished from the background noise, as well as being able to gather data at elevated temperatures.

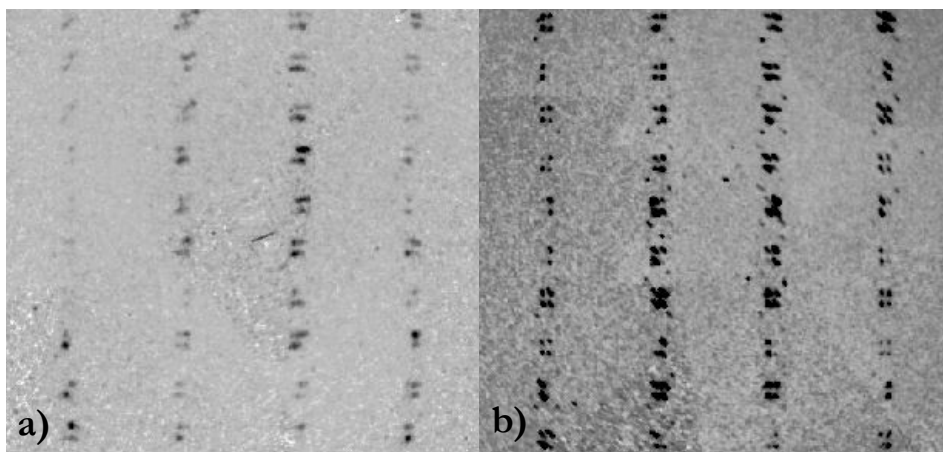


**Figure 21:** Two reconstructed diffraction patterns from a crystal of the same sample batch, both showing the same (1.5, k, l) orientation. a) Reconstructed pattern from a measurement recorded at a home source equipped with a molybdenum tube and exposure time 60s. b) Reconstructed pattern from measurements at synchrotron SOLEIL at a wavelength  $\lambda = 0.42484 \text{ \AA}$  and exposure time 1s.

Figure 21 shows two diffraction patterns in the same orientation, measured on a sample from the same batch, but the left image is recorded at an in-house source while the right image is recorded at synchrotron SOLEIL. The data was treated in the exact same way to produce both images, but the lightness of the left image was set to level 3 and the lightness of the right image was set to level 8 to produce comparable images (scale from 1-13, where 13 is the lightest and 1 the darkest image). Nevertheless it is clearly discernible how much blurrier and lighter the image to the left is. Moreover in the left image only first order satellites can be seen, while the right image exposes up to third order satellites.



#### 4.4 Single Crystal X-ray Diffraction\*

*O*n a single crystal diffractometer, the radiation is diffracted by the sample specimen, that is placed on a goniometer, then the diffracted rays pass through a beryllium window on the charge coupled device (CCD) detector. Afterwards X-ray photons are converted into visible light on a  $\text{GdO}_2\text{S}_2$  phosphor sheet, so that the CCD chip laying behind the phosphor can capture the information [48]. The information on the CCD chip can now be read out by respective software, CrysAlisPro [49] in this case, to convert the information to a diffraction pattern [47].

Most single crystal diffractometers are so called “four circle” diffractometers, as they have four moving circles, that ensure the possibility to irradiate a crystal specimen from every possible angle . This is necessary to capture as many reflections as possible to measure a high quality data set that can be treated easily.

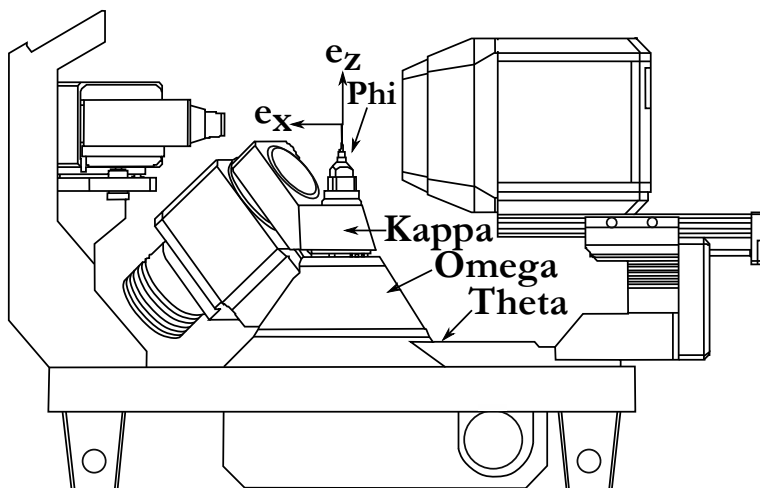


**Figure 22:** Image showing the geometrical setup of a four circle goniometer. The image is taken from Oxford Diffraction’s user manual [50].

Figure 22 displays the diffractometer geometry used here, while there are other possible geometries a discussion of those would be outside the scope of this thesis. The outer most circle, the Theta circle, rotates the detector, while the Omega, Kappa and Phi circles solely rotate the sample. Although this gives the option to measure all angles to cover the whole Ewald sphere of reflections, such an extensive measurement is rarely conducted for the sake of time efficiency. Instead fractions of the sphere (full sphere, half sphere or octant) or fractions according to the expected Laue symmetry are measured, which theoretically still results in a complete data set.

The single crystalline samples are usually chosen by visually selecting an adequate piece of sample under a light microscope. When measuring translucent samples, po-

larisation filters on the microscope can give insight to the quality of a sample by checking if the crystal changes from allowing light to pass to blocking light every  $90^\circ$  of rotation. Metallic samples, like the ones discussed here, are judged by the shininess of their surfaces. If a specimen has at least one surface with a mirror like appearance, it is deemed good enough quality to attempt an experiment.

The selected crystal can then either be glued onto a glass fibre, picked up with some parathone oil and a micro mount, or encapsulated between two quartz tubes. The latter is the method of choice when measuring at elevated temperatures, to prevent oxidation of the sample.

While the diffractometer software (CrysAlisPro) can be used to steer the diffractometer, it is also the software used to index and integrate the recorded diffraction patterns. To solve diffraction patterns the program Superflip [51] was employed as inbuilt in the used refinement program JANA2006 [43].

## 4.5 Powder Diffraction\*

Powder diffraction is a widely used technique that measures the bulk of a sample, making it possible to investigate the total composition of phases produced by a given synthesis. It is a powerful technique since it is fast, non-destructive, easy to use and does not require a large grain size or large quantity of samples. Furthermore in powder diffraction an entire diffraction pattern can be measured simultaneously, such that temperature dependent studies can be carried out in real time. However indexing a powder pattern of a complicated unknown sample, as the ones discussed below, can be demanding. Besides, while very precise cell parameters can be measured, the amount of information on other parameters such as atomic positions is small.

Contrary to its name, samples do not necessarily have to be in powder form, although this might be the most common sample type. Further possibilities comprise for example polymer films, chunks of materials or wafers. Samples are prepared by, in the case of powder, grinding them up and fixing them onto Mylar foil or scotch tape. The resulting foil or film is clamped between a masking disk, guiding the radiation to only penetrate a selected area, and a sample holder. Another option, mainly used to prepare samples for synchrotron powder diffraction, is to fill the powders in amorphous silica tubes that are sealed shut. Polymer or other film samples can also be directly clamped between the masking disk and the sample holder (Figure 23 left). Samples that are not thin enough to fit in this setup and can't be ground up can be measured by gluing them on a sample holder disk and measuring them in reflection mode (Figure 23 middle). When measuring a highly absorbing probe, this technique allows only to measure the surface of the sample, since radiation does not penetrate through the whole body of the probe. With a weakly absorbing probe, the beam can penetrate through the whole sample body, which however leads to peak broadening.

For preparations of synchrotron measurements or for air sensitive samples, a capillary setup can be used. Therefore the ground sample is filled in a glass or quartz capillary that can be sealed at the bottom. The respective sample holder (Figure 23 right) features a small hole in which the capillary can be fixed. Capillary measurements are also conducted with the beam transmitting through the whole sample.

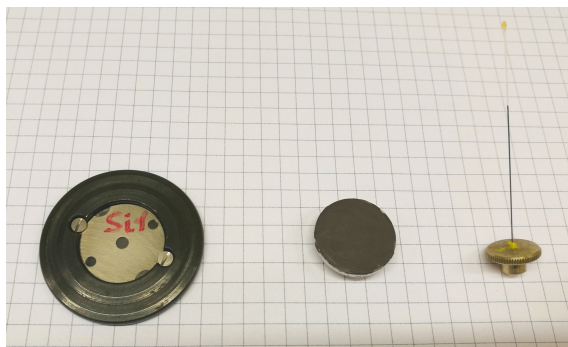


**Figure 23:** The photograph shows the three possible sample holders for the Stoe STADI MP machine. From left to right those are a flat plate for transmission, a disk for reflection and a capillary holder.

Once the sample is prepared, it is placed into the machine in the respective geometry. To ensure even better statistics of the sample homogeneity, samples are spun around their centre point.

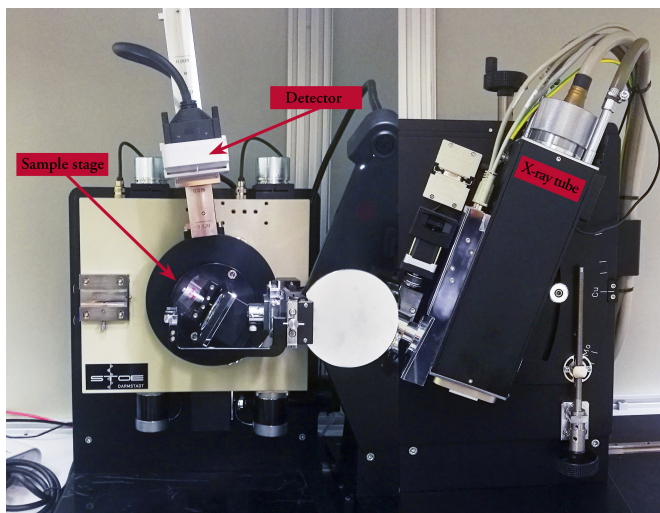


**Figure 24:** Photograph of the STOE stadi MP machine in its transmission setup with detector, sample stage and detector indicated.

While single crystal and powder machines are quite similar in their setup, it is worth to take a look at the components of a powder diffractometer separately.

While a single crystal machine has four moving circles, a powder machine has only two (see Figure 24). For the Stoe STADI MP those are the Kappa (detector arm) and Omega (sample holder) circles, while the X-ray source is stationary. Depending on if the setup is in transmission, reflection or capillary mode, the movement of the two circles is connected, separate or the sample holder is fixed to a single position. The detector (Mythen 1K) is a so called “silicon strip detector”, which records intensity and  $2\theta$  position. The origin of the powder pattern is very similar to the origin of the single crystal pattern, just instead of points, powders produce so called Debye rings due to the overlay of the diffraction spots from the vast amount of tiny crystallites. If a powder pattern would be measured on a two dimensional detector, the images would show concentric rings. On the 1D detector however, the classic powder pattern is displayed (see Figure 25).

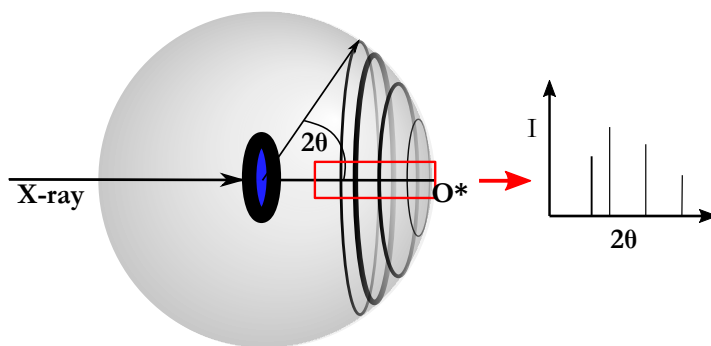


**Figure 25:** Graphic depicting how powder diffraction patterns come about with the help of the Ewald sphere. The round disk in the middle indicates the transmission sample and the rings on the right half of the sphere are the resulting Debye rings. A red rectangle indicates the portion of this sphere that is picked up by the detector and the right side of the graphic shows a sketch of a resulting diffraction pattern. Picture adapted from [47] and a similar graphic is also found in the Licentiate thesis [3].

The mentioned overlay of diffraction spots is the reason why the powder diffraction method is inherently one dimensional: it results in diffracted intensity being homogeneous in two out of three spacial directions [52]. Nevertheless, the resulting powder diffraction pattern contains a lot of information, that is best described in Table 4, that is reproduced from V. Pecharskys and P. Zavalijš “Fundamentals of Powder Diffraction and Structural Characterization of Materials” [47].

**Table 4:** The table explains how the three pattern components are influenced by the respective sample, structure and machine parameters. Bold written parameters are key and italicised parameters may have a significant influence. The table is copied verbatim from [47].

Pattern component	Crystal structure	Specimen property	Instrumental parameter
Peak position	<b>Unit cell parameters:</b> <i>a, b, c, <math>\alpha, \beta, \gamma</math></i>	<i>Absorption</i> <i>Porosity</i>	<b>Radiation (wavelength)</b> <i>Instrument / sample alignment</i> Axial divergence of the beam
Peak intensity	<b>Atomic parameters</b> ( <i>x, y, z, B, etc</i> )	<i>preferred orientation</i> Absorption <i>Porosity</i>	Geometry and configuration <b>Radiation (Lorentz and polarization)</b>
Peak shape	<i>Crystallinity</i> Disorder Defects	<i>Grain size</i> <i>Strain</i> <i>Stress</i>	<b>Radiation (spectral purity)</b> <b>Geometry</b> <b>Beam conditioning</b>

Once a powder pattern is recorded, again the program JANA2006 [43] is used to refine the measured pattern against a standard pattern. In the present case only the method of pattern fitting, a so called LeBail decomposition, which was introduced in chapter 2.4, is used.

## 4.6 Synchrotron X-ray Diffraction\*

In the year 1981 the first dedicated synchrotron radiation source opened its doors to user operation in Daresbury, England. Ever since, synchrotron facilities have developed many new experiments and setups for even more detailed insights into research [46]. The three major topics of measurement types offered at synchrotron sources are: diffraction, imaging and spectroscopy, and the beam lines discussed below are all diffraction beam lines.

The general setup of a diffractometer in a synchrotron is not different from an in house source, but they are usually capable of higher precision and may have additional features.

#### 4.6.1 CRISTAL Beam Line at Synchrotron SOLEIL

Synchrotron SOLEIL, the french national synchrotron, is located on the Plateau de Saclay in Saint Aubin, Essonne, close to Paris. It is a third generation synchrotron with a storage ring of 453 m circumference, that operates at 2.75 GeV. Furthermore it features 29 beam lines of which the CRISTAL beam line, located at a U20 undulator, is the dedicated single crystal beam line. The wavelengths are chosen with two silicon double crystal monochromators in orientation (111) and (311) and the range of possible energies lies between 4 - 30 keV (the here used energy was:  $0.42484 \text{ \AA} \approx 29.154 \text{ keV}$ ). While the beam line also offers a two- and a six-circle diffractometer, for the measurements discussed below a four-circle diffractometer was used. The diffractometer is produced by Newport, while detector (Agilent 2D CCD) and software are of Rigaku's origin. Additionally for those measurements a hot gas blower from Cyberstar was used as fitted to the beam line setup [53].

#### 4.6.2 I19 Beam Line at Synchrotron Diamond

The Diamond light source is also a synchrotron of third generation with a storage ring of 562 m circumference and an energy of 3 GeV. It features 32 beam lines of which I19 is the dedicated single crystal beam line. It offers two experimental hutches, one equipped with a three-circle diffractometer and a Pilatus 2M detector, the other equipped with a four-circle diffractometer and a Pilatus 300K detector. Moreover measurements can be conducted at energies between 5 - 25 keV, where the experiments discussed below were conducted in the latter experimental hutch and used an energy of approximately 25 keV ( $0.4859 \text{ \AA}$ ). Additionally a hot air blower was set up to measure diffraction at temperatures up to  $300^\circ\text{C}$  [54].

### 4.7 Anomalous Dispersion

With standard diffraction wavelengths  $S_n$  and  $S_b$  cannot be distinguished as  $S_b$  has only one more electron in its shell and hence their form factors are very similar. Therefore a wavelength close to the absorption edge of tin was chosen to measure the structure of  $\text{Sn}_3\text{Sb}_2$ .

By using a wavelength close to the absorption edge of Sn, some of the X-ray photons can ionise the tin atoms in the lattice. This results in the diffracted radiation being slightly changed in amplitude and phase, impacting the structure factor equation (see equation 3) as seen in equation 8.

$$f_{new} = f \pm \Delta f' + \Delta f'' \quad (8)$$

Where  $\Delta f'$  is the real part and  $\Delta f''$  is the imaginary part of the contribution. As indicated by the  $\pm$  sign, the real part of the contribution can be positive or negative,

whereas the imaginary part is always positive. Values for  $\Delta f'$  and  $\Delta f''$  can be found in the International Tables for Crystallography Volume C: Mathematical, physical and chemical tables [40] and have to be taken into account at the end of the structural refinement.

The effect of anomalous dispersion is not dependent on the angle of diffraction, therefore its effects on the intensity distribution in the diffraction pattern can be seen better at higher angles. One slight draw back of this method is the produced non-directional  $K_{\alpha}$  radiation, subsequently leading to a larger amount of background radiation.

As a result in the case described below, the diffraction intensity originating from the tin atom, is clearly different from the intensity of the antimony atom, and hence the positions of those atoms in the structure can be distinguished [39].

## 5 Main Results of the Research Papers

Out of chaos comes order.

Friedrich Nietzsche

### 5.1 AuIn\*

#### 5.1.1 Experimental\*

To establish a tempering routine that results in high quality single crystals a DTA measurement was conducted and according to the results (Figure 26) tempering points at 200°C and 400°C were chosen. The step at 400°C was chosen to establish the structure, adopted right after solidification, while the sample was tempered at 200°C to more carefully anneal the room temperature structure, which has proven to work excellent for powder samples. The samples were homogenised beforehand at 1000°C for two days and the annealing steps took 5 days each.

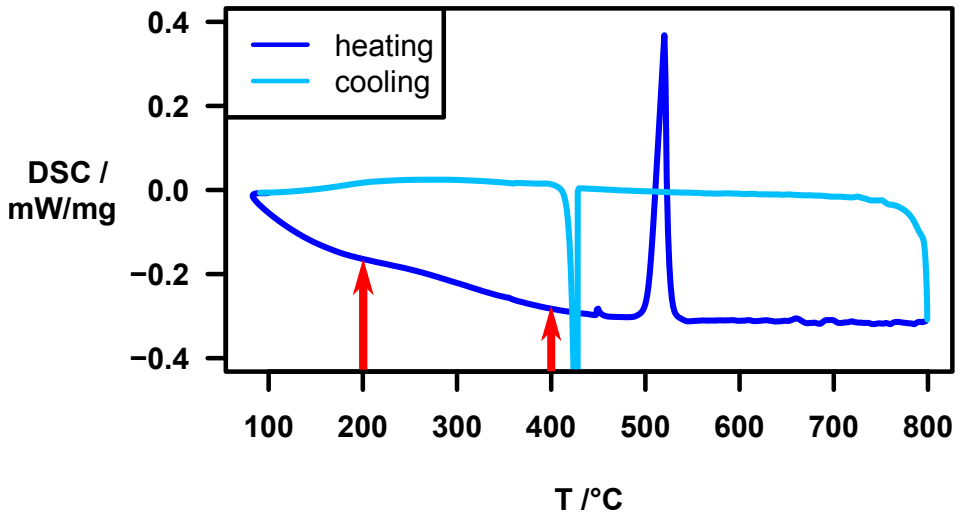


Figure 26: DSC measurement of AuIn, with two red arrows indicating the temperatures at which the crystals were annealed. Also found in the Licenciate thesis [3].

Synthetically, the samples were prepared as discussed in section 4.1. Resulting from this were silver coloured ingots with a metallic lustre, which could be cracked into small shards. Some of those shards proved to be high quality single crystals, which were subsequently taken to synchrotron SOLEIL, where samples were measured at



their CRISTAL beam line, additionally featuring the option of elevated temperatures. To prevent oxidation during the measurement, the crystals were wedged between two quartz capillaries. Diffraction measurements were taken at room temperature, 300°C and 400°C with a wavelength  $\lambda = 0.4248 \text{ \AA}$  and a special sequence of rotations to prevent the goniometer crashing into the heat blower.

### 5.1.2 Results and Discussion\*

Resulting from the above described measurements, the reciprocal space images seen in Figure 27 were reconstructed.

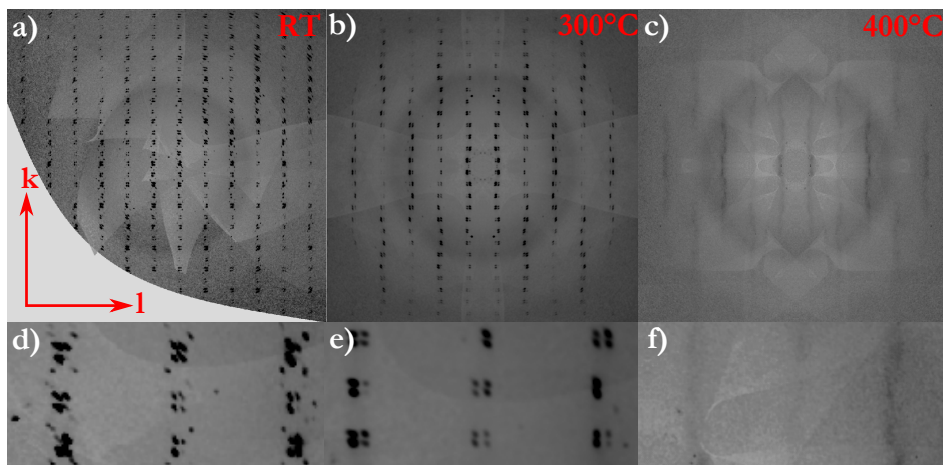


**Figure 27:** a)-c) Full images of reciprocal space reconstructions at room temperature, 300°C and 400°C (left to right) in (1.5kl) orientation. d)-f) Zoomed in versions of the above reconstructions showcasing the change of the amount and sharpness of the satellite reflections. Note that the patterns seen in the background originate from these images being pieced together from various single diffraction frames, whose background intensity slightly varies.

Starting at the left most image (Figure 27 a and d) with the situation at room temperature, close examination shows satellites up to third order that appear in rectangles along lines parallel to the  $k$  direction. At 300°C the lines of rectangles persist, however the maximum order of reflections is only one. Also note how the lines parallel to the  $k$  direction become more wavy. In the right most image of the 400°C measurement, the satellite reflections have disappeared and been replaced by diffuse scattering at the same position.

If the structure at 400°C is solved and refined, the space group  $Cmcm$  (63) with lattice parameters  $a = 3.6213(8) \text{ \AA}$ ,  $b = 10.6431(16) \text{ \AA}$ ,  $c = 4.3936(6) \text{ \AA}$  emerges [55]. Also the atomic positions - modelled by a single position for gold and a single position

for indium without taking the diffuse scattering into account - mimic the TII structure precisely. The atomic displacement parameters (ADP) however were elongated along the **a**- (Au) and **c**-axes (In), which indicated that both atomic positions had to be split. To ensure a physically reasonable structure, only one of the two positions can be occupied, *i.e.* at each point in space one of the positions has to be chosen over the other. A first clue on the choice of positions comes from the placement of the diffuse streaks, which can be found at  $(h + 0.5, k, l + 0.5)$ , indicating a doubling of the **a**- and **c**-axis. For a more in depth understanding the diffuse scattering was interpreted by the three dimensional delta pair distribution function (3D- $\Delta$ PDF). The 3D- $\Delta$ PDF works similarly to the Patterson function and hence returns a map of interatomic vectors giving insight to local structural phenomena. As the 3D- $\Delta$ PDF is calculated from the difference of the Patterson function and the full pair distribution function, it accentuates the effects that can only be seen in a PDF map. Diffuse frames were reconstructed using the program “Meerkat” [45] and the respective intensity extracted to remove any contribution from Bragg scattering. The diffuse scattering was integrated and Fourier transformed by a fast Fourier transform (FFT) function and lastly plotted in the program “Yell”. A Mexican hat shape of the intensity spots is discernible in the resulting plots (example in Figure 28), which can indicate an atomic displacement disorder [45]. Moreover the networks of gold and indium at lower temperatures gave a starting point to model the structure at 400°C. This idea was again programmed with “Yell” culminating in a 3D- $\Delta$ PDF, which compared excellently to the raw data 3D- $\Delta$ PDF map (see Figure 28b).

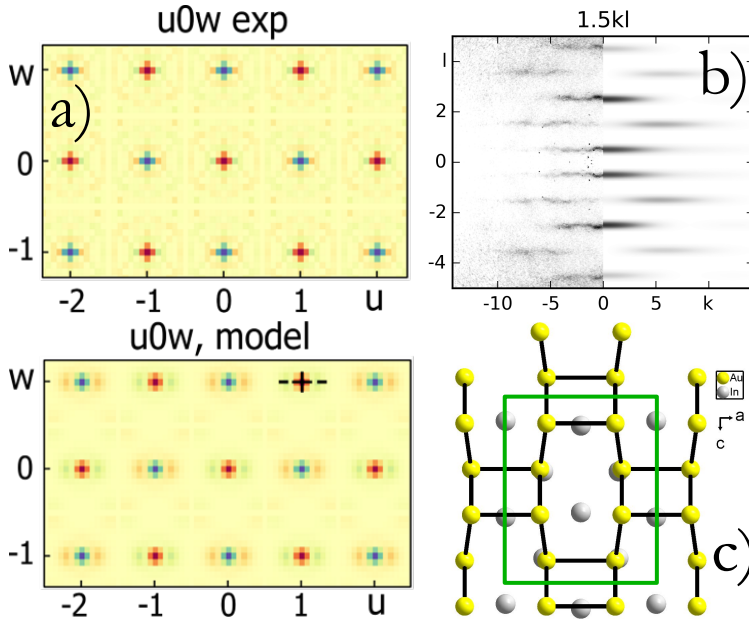


**Figure 28:** a) Yell plot of the measured data (upper panel) and the model (lower panel) showing the Mexican hat shape features. b) Measured (left) and modelled (right) diffuse scattering. c) Resulting network of AuIn, where the green rectangle indicates the unit cell after doubling the  $a$ - and  $c$ -axes. Also found in the Licenciata thesis [3].

Lastly Figure 28 c) shows a plot of the new AuIn lattice, with the expanded unit cell in green. Comparing the gold lattice directly to the thallium lattice in TII or the earlier proposed gold lattice, it is discoverable that the distances between the gold atoms have undergone a rearrangement from being all equidistant to now exhibiting a “short - long - short - long” pattern along the  $a$ -axis. This kind of pattern is strongly reminiscent of the typical Peierls distortion pattern (see Figure 29).

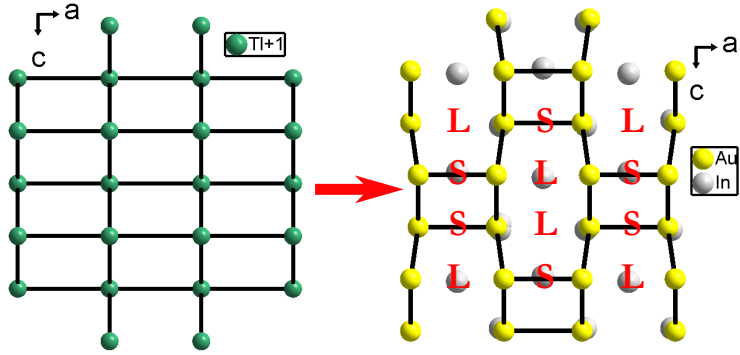


**Figure 29:** Image showing the distortion from the thallium network in thallium iodide (data from [8]), to the Peierls distorted version of the gold network in gold indium. Red capital “S” and “L” in the right image indicate short and long interatomic distances between two gold atoms.

To understand if the distortion is indeed of Peierls type, the band structure and electronic properties of AuIn were computationally analysed <sup>1</sup> [55]. Therefore two models were set up: One that represents the original TII type structure (I) and another one as a commensurate approximant ( $q = 0.5 \ 0.5 \ 0.5$ ) of the later described incommensurate structure (II). The two models with their respective band structures can be seen in Figure 30.

<sup>1</sup>Analyses were conducted by Fei Wang, not by the author

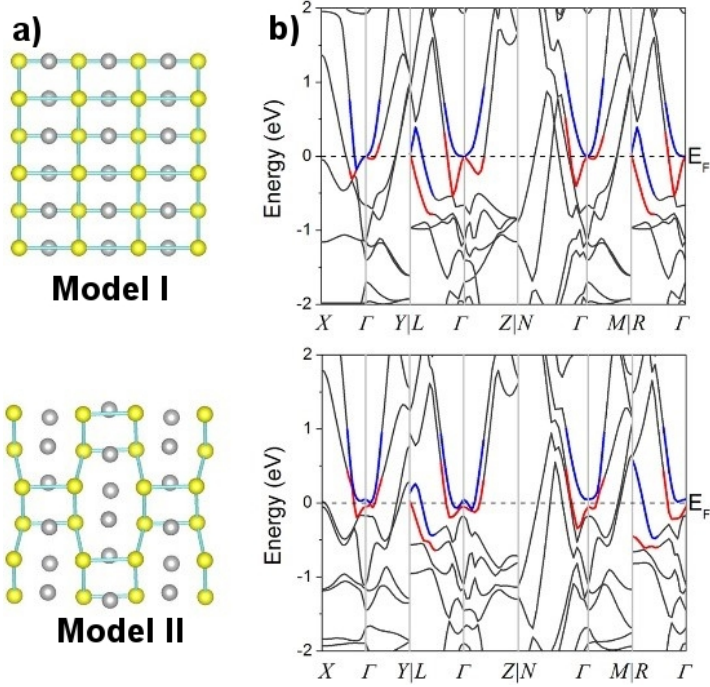


**Figure 30:** a) TII type model I (upper panel) and approximant model II (lower panel). b) The calculated band structures belonging to model I (upper panel) and model II (lower panel). The bands of interest are highlighted in blue (higher energy) and red (lower energy). Figure and calculations made by Fei Wang and also found in the Licenciate thesis [3].

Comparing the red and blue highlighted bands at the Fermi level ( $E_F$ ) of both models shows that the degeneracy is lower in model II. Furthermore the total energy of both models was calculated as indicated in Table 5.

**Table 5:** Calculated total energy values in electron volts per cell or formula unit, respectively [55]. The stabilising energy is small but significant.

	$E_{\text{total}}$ (eV/cell)	Relative $E_{\text{total}}$ (eV/fu)
Model I	-25.080441	0
Model II	-25.108235	-0.0069485

Even though the energy lowering from model I to model II is small, it is significant and together with the opening of band gaps at the Fermi level, these findings corroborate the preference of the Peierls distorted model.

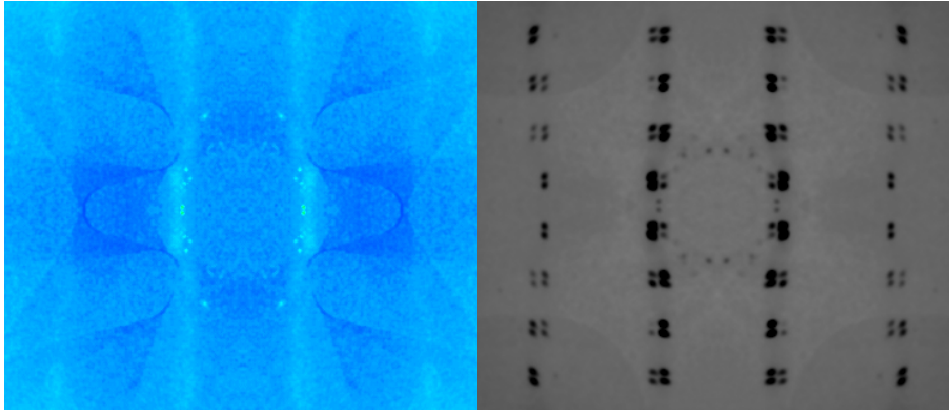


**Figure 31:** The left side shows the diffuse scattering found at 400°C, whereas the right side shows the exactly same reconstructed image at 300°C. As can be seen, the diffuse scattering condenses into first order satellites on cooling. Both Figures are in 1.5kl orientation. Also found in the Licenciate thesis [3].

At 300°C the diffuse scattering has condensed into first order satellite reflections, that are grouped into rectangles (see right side of Figure 31). To account for the additional reflections the crystal structure is now modelled with the triclinic, incommensurate space group  $C\bar{1}(\alpha\beta\gamma)0$  and the q-vector  $q = (0.5009(11), 0.435(4), 0.5294(17))$ . There are three atomic positions in this description, of which one is the indium atom, modelled by a sinusoidal position and an ADP wave and two gold positions, each being half occupied and modelled by a crenel occupancy function and a sinusoidal ADP wave.

The description of the gold atomic positions is a slightly special case, that needs more attention. When looking at the electron density function of gold (Figure 32a), a sinusoidal model would be regarded as more appropriate for this electron density. While it does result in a decent description with reasonable ellipsoids, the use of a crenel function has been preferred for the model (Figure 32b). This is because a crenel function is better at exhibiting the nature of the effect of an atom at one lattice point being either in position A or B. It is never found to be in an intermediate position or even at both points at the same time, which would be indicated by the sinusoidal model. The correctness of the crenel model is also corroborated by its appearance in the room temperature structure, where a sinusoidal model is clearly out of question. Moreover, explaining the condensation of diffuse scattering into satellites is more reasonable by being thought of as an increase of domain size and hence order. If the sinusoidal description was favoured, a gradual movement from a TII - type network to a Peierls distorted TII - type network would have to be assumed, where intermediate bond lengths would need to be stabilised.

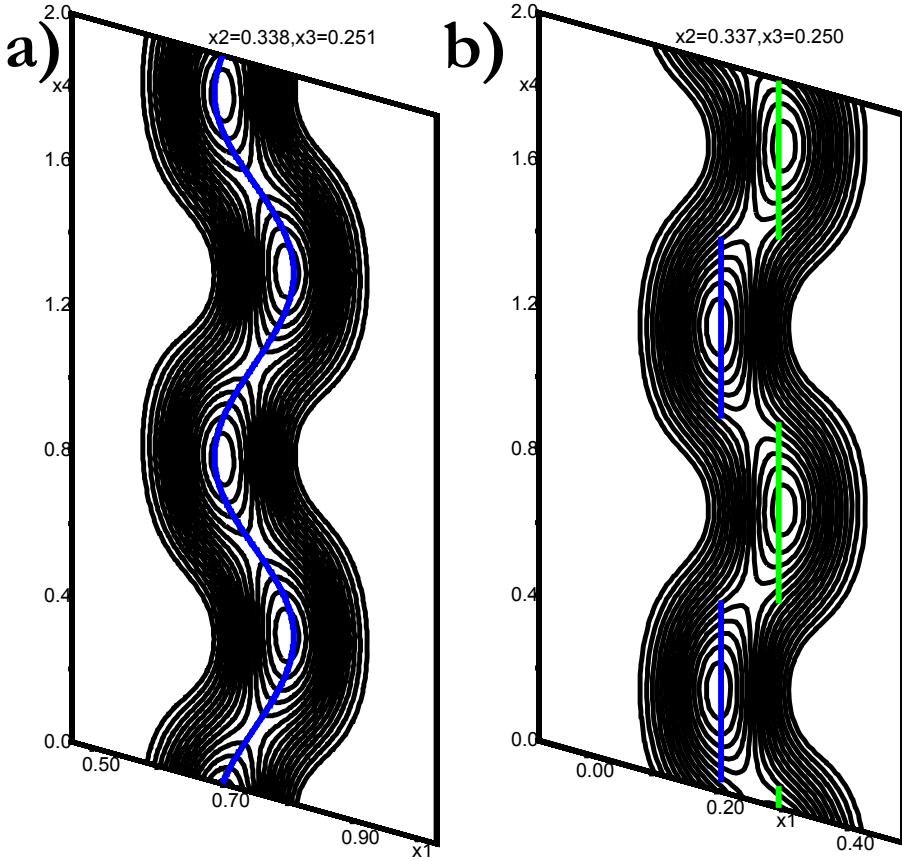


**Figure 32:** Two different attempts at modelling the electron density of gold at 300°C. a) Sinusoidal description, with the blue line depicting the atomic position. b) Crenel description with the two half occupied atomic positions depicted by blue and green lines. Also found in the Licenciate thesis [3].

Finally this results in a unit cell looking precisely like what is found at 400°C with the same 8484-network.

The lowest temperature measurement was taken at room temperature, where satellite reflections up to third order can be found. This upsurge of satellites indicates an increase of order in the structure and also manifests in a slight change in the  $\beta$  position of the q-vector. Where  $q_{300^\circ C} = (0.5009(11), 0.435(4), 0.5294(17))$  and  $q_{RT} = (0.4987(9), 0.378(2), 0.4753(11))$ , *i.e.* the difference in  $\beta = 0.057(4)$ , which is significant. Structurally, this difference results in a changed stacking order of gold layers along the **b**-axis. Figure 33 shows the gold layers found at 300°C, which repeat their pattern after approximately every 14<sup>th</sup> layer. At room temperature a repetition of the stacking pattern can only be found after approximately 42 layers of gold, which

originates from a shearing of the q-vector in its  $\beta$  direction. Note that the numbers of repeat are only approximate since this structure is incommensurate, *i.e.* there is no integer multiplier that produces an exact repeat of the structure.

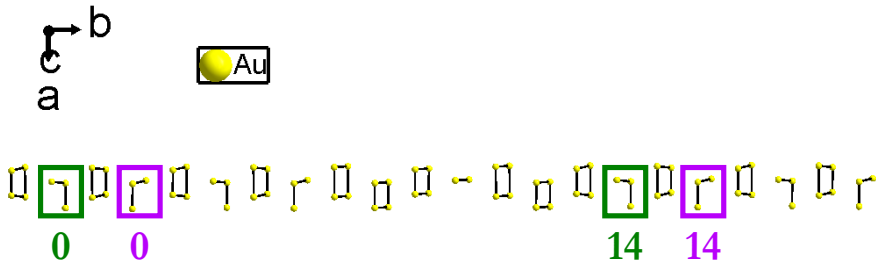


**Figure 33:** The Figure shows slabs of gold layers at  $300^{\circ}\text{C}$  stacked along the  $b$ -axis, with green and red rectangles indicating at what point the same rectangular pattern is recovered. Here the repeat is 14 fold, while at room temperature 42 stacks are required to recover the same rectangular pattern. Also found in the Licenciate thesis [3].



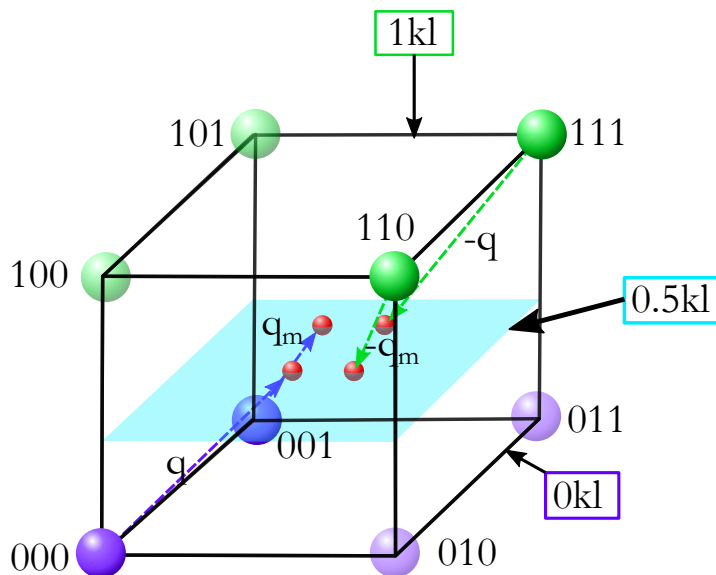


**Figure 34:** A hypothetical cubic unit cell with allowed main reflections in green ( $h = 1$  layer) and purple ( $h = 0$  layer), where the transparent spheres indicate the extinct reflections. Red spheres show first order satellites in a hypothetical  $h = 0.5$  layer. Green and purple dashed arrows indicate the main reflections that produce the respective satellites.  $q_m$  and  $-q_m$  indicate  $q$ -vectors with their respective satellite reflections that originate from twinning, which is only observable in the satellite reflections. Also found in the Licenciate thesis [3].

Generally, the origin of the intriguing rectangular satellite pattern found here can be explained as follows. Satellites can only be found in layers of type  $h + 0.5$  and originate from main reflections in the  $h$  layers above or below. This produces the two satellites pointed at by the arrows “ $q$ ” and “ $-q$ ” in Figure 34, “ $q_m$ ” and “ $-q_m$ ” originate from a mirror operation inducing twinning in the satellites. Moreover if a second iteration of the original  $q$ -vector is added to the position of the satellite that it points to, it is clear that it would end up very close to what is labelled as the (111) reflection in Figure 34. Two reflections that lie so close together cannot be separated by programs indexing diffraction reflections, especially in this case where one reflection is clearly lower in intensity than the other. Furthermore this impacts the refinement, as second order satellites cannot be used, *i.e.* a quite large amount of information is inaccessible. This is however not a problem, since the electron density for gold and indium shows a crenel shape (see Figure 35). Since crenel functions only use odd amplitude terms, second order satellites would most probably be weak. The final structure at this temperature comes about with very uniform ellipsoids and the same shape as discussed at higher temperatures.

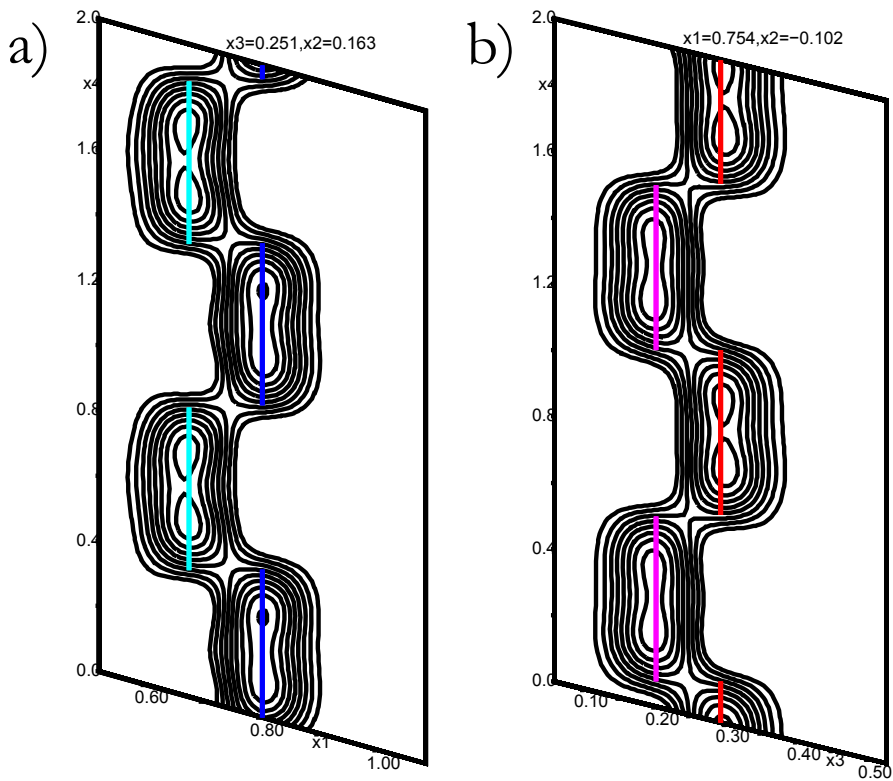


**Figure 35:** a) Electron density of gold at room temperature, with the two atomic positions in blue and green. b) Electron density of indium at room temperature with the two atomic positions in magenta and red.

Before suitable single crystals were grown, this structure was also studied by powder diffraction.

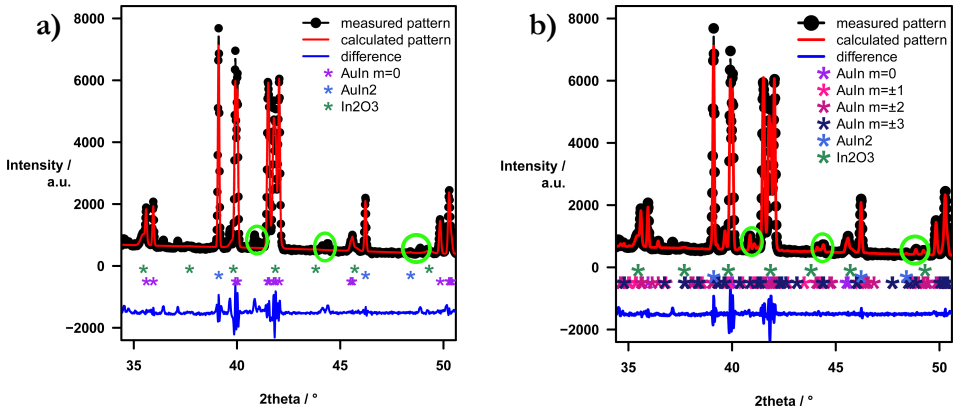


**Figure 36:** Zoomed plots of powder diffraction from an AuIn sample, refined with the two impurity phases  $\text{AuIn}_2$  and  $\text{In}_2\text{O}_3$ . a) Shows the refinement if AuIn is handled as a 3D structure. b) Shows the same refinement when a modulated approach with satellites up to third order is used. As can be seen, the peaks that are not treated in a) are accounted for in b). Also found in the Licenciate thesis [3].

A zoomed plot of a powder diffraction pattern is shown in Figure 36, where a) shows a 3D refinement and b) a modulated refinement. As indicated by three neon green circles, Figure 36 a) exhibits a number of peaks that are not accounted for by the AuIn structure, nor by any of the impurity phases  $\text{AuIn}_2$  and  $\text{In}_2\text{O}_3$ , whereas in Figure 36 b) those peaks are indexed by satellite reflections.

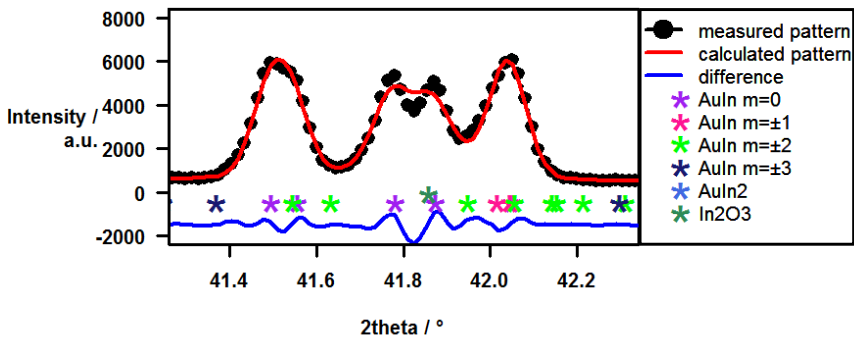


**Figure 37:** Zoom of the area around  $2\theta = 42^\circ$  showing how main reflections overlap with second order satellite reflections. Also found in the Licenciate thesis [3].

The diffraction peak at  $2\theta = 41.55^\circ$  in Figure 37 showcases another corroboration that second order satellites and main reflections coincide in a form that they cannot be indexed separately.

## 5.2 PdBi

### 5.2.1 Experimental

According to DSC results, tempering points at 200°C and 580°C were chosen (Figure 38). Here the sample was first allowed to establish its basic order at 200°C, before it was given additional thermal energy at 580°C to anneal the superstructure. Beforehand, the sample was homogenised at 800°C.

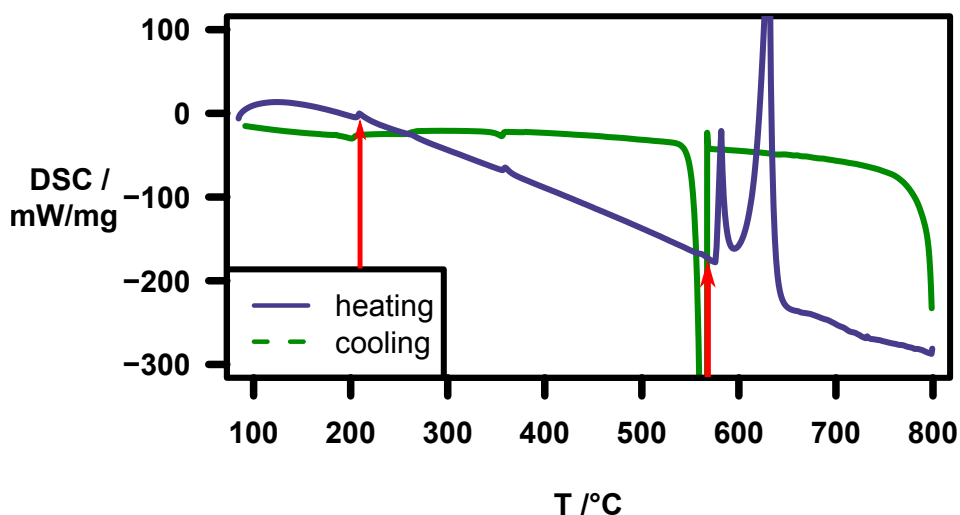


Figure 38: This plot shows the PdBi DSC curve, indicating the heating run in blue and the cooling run in green. The heating curve shows two endothermic peaks at 583°C and 628°C, while the cooling curve shows an exothermic feature at 563°C. Additional small endo- and exothermic features are discernible at 210°C.

PdBi crystals were prepared through a simple shake and bake routine as discussed in section 4.1. As a result small dark needles with a metallic lustre were found in the cracked ingot, which were wedged between two quartz capillaries and taken to the I19 beam line of synchrotron Diamond. These crystals were measured at room temperature, 200°C, 220°C and 250°C to observe the structural transformations undergone by this material.

### 5.2.2 Results and Discussion

At room temperature, the resulting diffraction patterns on first glance opt for a non-modulated orthorhombic description with lattice parameters approximately  $a = 7.5 \text{ \AA}$ ,  $b = 10 \text{ \AA}$ ,  $c = 8 \text{ \AA}$  and  $\alpha = \beta = \gamma = 90^\circ$ . If the  $a$ -axis is halved the new lattice parameters read  $a = 3.6155(2) \text{ \AA}$ ,  $b = 10.7047(6) \text{ \AA}$ ,  $c = 8.7588(6) \text{ \AA}$ ,

$\alpha = 90^\circ$ ,  $\beta = 90.144(5)^\circ$ ,  $\gamma = 90^\circ$  and resemble the TII structure. Furthermore this reveals satellite reflections at  $(h + \sigma_1, k, l)$ . The development of those reflections with temperature can be seen in Figure 39.

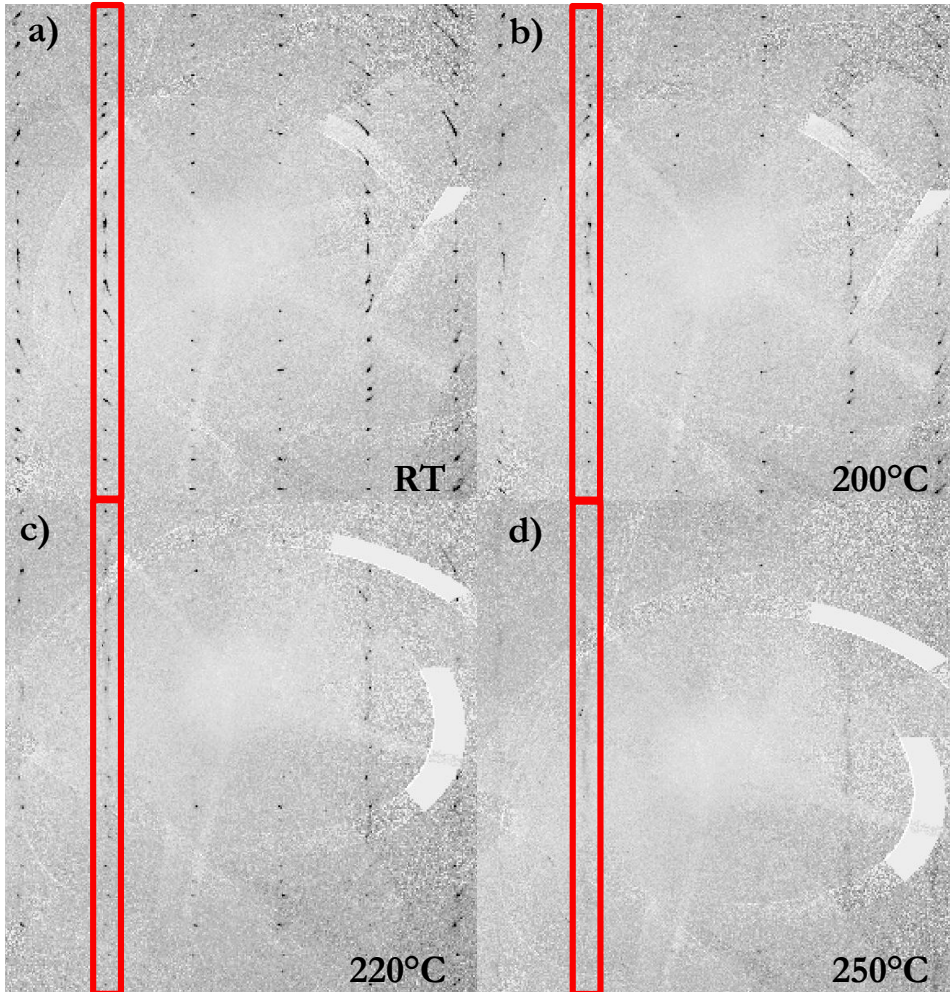


**Figure 39:** Reconstructed diffraction images of PdBi, all in  $hk1$  orientation. a) At room temperature the satellites lie precisely on a line at  $h + 0.5$ , one of them being highlighted by a red square. b) At  $200^\circ\text{C}$  the satellite reflections have moved slightly away from this line, *i.e.*  $q = (0.4848, 0, 0)$ . This deviation is however nearly impossible to see here and will be clearer in a later image. c) At  $220^\circ\text{C}$  satellites start to lose intensity, indicating their decay. d) At  $250^\circ\text{C}$  only diffuse scattering is left.

For the room temperature measurement  $\sigma_1 = 0.5$ , *i.e.* satellites are found at precisely  $(h + 0.5, k, l)$ , which can either indicate a commensurate modulation or a non-

modulated structure. While both options are possible and result in solutions of similar quality, assigning the correct space group is more difficult. This is underscored by the fact that previous publications of PdBi report three different space groups. Zhuravlev - who reported the structure first - finds the orthorhombic space group  $Cmc2_1$  [26], Bayliss even solves the structure as hexagonal with space group  $P6_3/mmc$  [56] while Bhatt and Schubert report the monoclinic space group  $P12_11$  [27]. Moreover Ionov *et al.* index their data also with a monoclinic space group, but different lattice parameters and a different cell setting to be  $P112_1$  [57].

The here presented results agree with Bhatt and Schubert, finding that there is a monoclinic distortion discernible in the data, even though the  $\beta$  angle is artificially close to  $90^\circ$  due to twinning. This leads to the question of which space group should be assigned. Assuming that the basic space group, ignoring all distortion effects, is  $Cmcm$ , an analysis was conducted to find subgroups that appear on doubling the  $a$ - and  $c$ -axes simultaneously. Doubling the  $a$ -axis violates the  $C$ -centring, the  $2_1$  screw along  $a$ , the  $n$ -glide perpendicular to  $b$  and the  $n$ -glide perpendicular to  $c$ . Accordingly the doubling of the  $c$ -axis also violates the  $C$ -centring, the  $n$ -glide and the  $c$ -glide perpendicular to  $b$  and the  $2_1$  screw axis along  $c$  [58] (Figure 40a). Note also that it is important that the  $a$ - and  $c$ -axes are doubled simultaneously, otherwise the centring, which is clearly visible in the diffraction data, cannot be restored (Figure 40b).

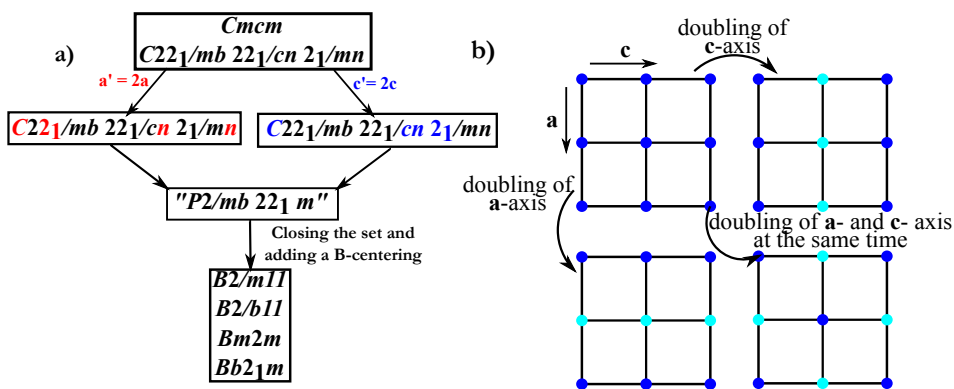


**Figure 40:** a) Graphical representation of the space group analysis required to understand which possible space groups could be used to describe the PdBi room temperature structure. Blue and red labelled symmetry elements on the second level are violated by the axis doubling. b) Image explaining why only a simultaneous doubling of  $a$  and  $c$  results in a new centring. Dark blue dots represent preserved atomic positions while light blue dots represent extinct atomic positions.

The space group analysis leaves the options  $B2/m11$ ,  $B2/b11$ ,  $Bm2m$  and  $Bb2_1m$ . Since the diffraction data requires to have precisely one mirror plane in the space group symmetry, the options reduce to  $B2/m11$  and  $Bb2_1m$ . Both alternatives were tested,

but a stable refinement could only be achieved by using the monoclinic  $B2/m11$  space group. Additional extinction conditions imposed by the satellite reflections are:  $l + m = 2n$ ,  $h + k = 2n$  and to close the set  $h + k + l + m = 2n$ . Those induce an X centring and hence the final super space group reads  $X12/m1(\alpha 00)00$ . Note that the setting in this space group uses a unique **b**-axis, and while this is the standard setting for monoclinic space groups, the 200°C structure will use a setting with a unique **a**-axis.

To understand this fact, quite a few approaches had to be tested and many pitfalls were found. Some are described below together with a list of choices that eventually lead to the correct solution.

- modulated or non-modulated?
- orthorhombic or monoclinic?
- $C2/c$  or  $X2/m$ ?
- a unique or b unique?

The room temperature PdBi structure could also be modelled in a non-modulated structure, since this is a commensurate case, resulting at first glance in an excellent goodness of fit (GOF) and  $R_{\text{obs}}(\text{all})$  but on closer inspection showcasing a terrible  $R_{\text{int}}$  and nonphysical ADP parameters. Moreover it is more elegant to describe it as a modulated structure for the ease of comparability to the other TII type structures discussed in this thesis and the high temperature PdBi structure.

As written above, the deviation from 90° is small but in this case significant and corroborated by the symmetry analysis. Hence the second question is answered by having to chose a monoclinic space group.

While  $X2/m$  can be excluded in a non-modulated description, because the X-centring originates from implications given by the satellites,  $C2/c$  is still an option in a modulated approach if the q-vector is chosen to be of the type  $q = (\alpha, 0, \gamma)$ , *i.e.* the **c**-axis is also halved, resembling even more the lattice parameters found in TII and AuIn. Indeed this results in a misleadingly good refinement, with the only drawback of a rather poor  $R_{\text{int}}$  (17.54%). This could be attributed to the poor crystal quality: the crystals are all tiny, needle shaped and produce, in addition to the single crystal reflections, visible Debye contribution in the diffraction patterns. However, the internal R value of the high temperature data (7.95%) was so massively better, that the difference could not simply be explained by amelioration of the crystal due to heating. Hence a different setup of the unit cell was employed resulting in a much better  $R_{\text{int}}$  (9.37%).

While previously a setup with a unique **a**-axis together with a balanced (50:50) twin model was used, the structure was transformed to employ a unique **b**-axis and an imbalanced twin model, with specimen 1 accounting for 87% and specimen 2 accounting only for 13% of the data.

The bar plot in Figure 41 graphically underlines how the several refinements compare in their refinement values.

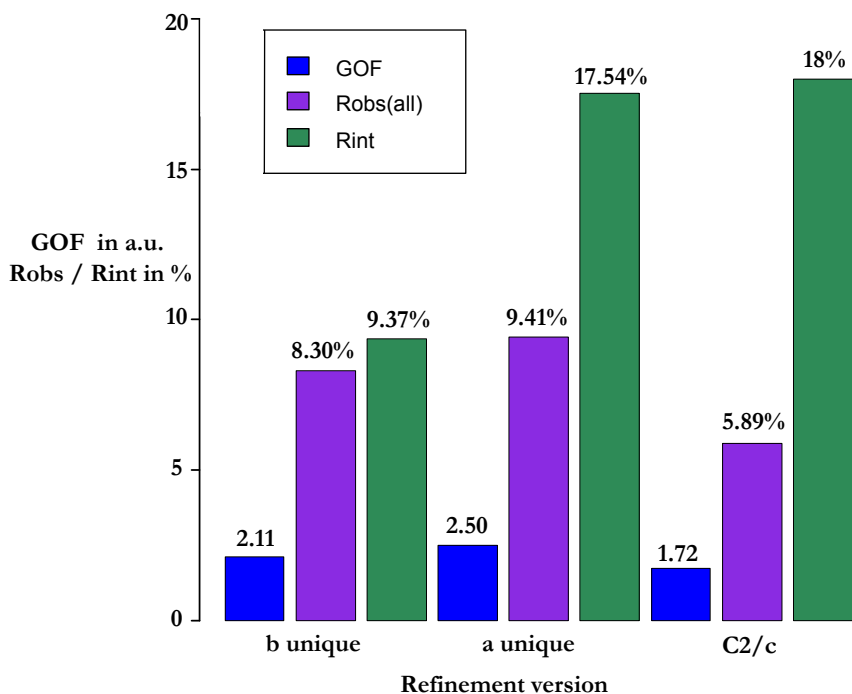


**Figure 41:** Bar plot of the refinement parameters  $R_{\text{obs}}(\text{all})$  and  $R_{\text{int}}$  in percent and GOF in arbitrary units. All of the values are shown for a refinement strategy in the  $X12/m1(\alpha 00)00$  space group for a unique **a**-axis, a unique **b**-axis and for the 3D space group  $C2/c$ , respectively.

In  $X12/m1(\alpha 00)00$ , the structure can be modelled with one bismuth and one palladium atom. Bismuth is described by two sinusoidal positional waves and palladium is described by one sinusoidal positional wave and one crenel occupational wave.

Subsequently the resulting structural picture is similar to what has been seen in the case of AuIn (section 5.1). Palladium exhibits the Peierls type distorted eight and four ring pattern extending in the **ac**-plane and stacking layers of those zig-zagged networks along the **b**-axis (see Figure 42).



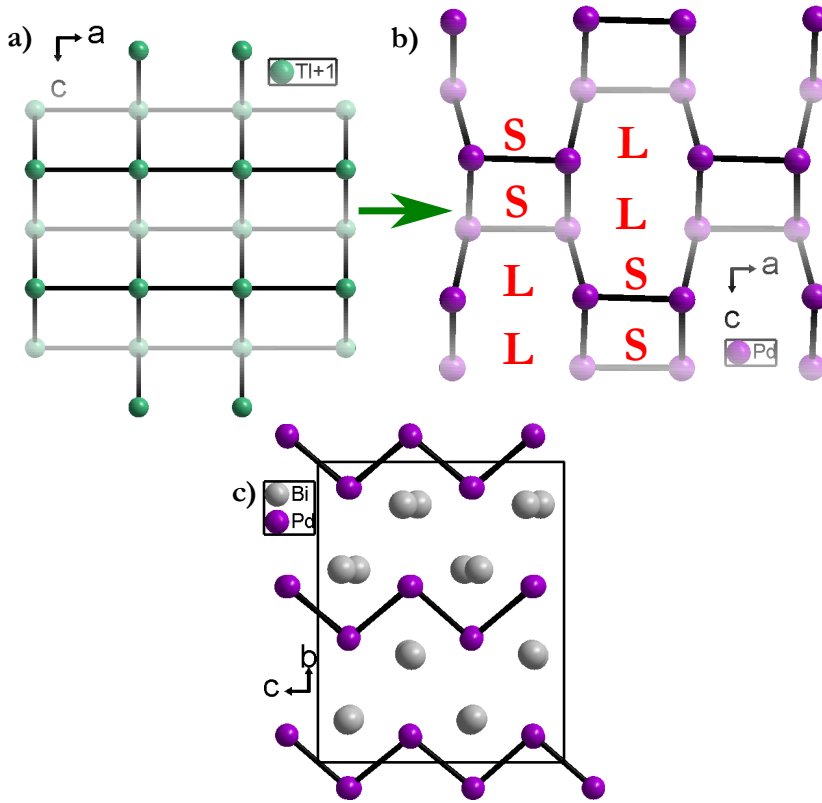


**Figure 42:** The palladium bismuth structure at room temperature. a) The thallium network in the original TII structure [8]. b) The Palladium network in the ac-plane as it adopts the Peierls type distorted version of the thallium network. c) View of the PdBi unit cell in the bc-plane, showcasing its zig-zag layers.

If the crystal is measured at 200°C the satellite reflections discommensurate *i.e.* they move away from their positions at  $h + 0.5$  to  $h + 0.4848$ . While this was already indicated in Figure 39, Figure 43 shows the discommensuration in more detail. The left upper panel in this Figure shows a reconstruction of the measurement in  $hk1$  orientation at room temperature, where the red line as guide to the eye indicates that all satellite reflections lie on the same position. In the upper right panel the same situation is displayed, but with all the satellite intensity and position sampled along the  $a^*$ -axis. This histogram plot clearly only shows one peak position. In the lower left panel a reconstruction of an  $hk1$  image is shown at 200°C, where it is discernible, emphasised by red arrows, that the satellite reflections have moved away from the red line. In the corresponding histogram plot, what was previously a single peak has now split into two positions at  $a^* = 0.4848$  and  $a^* = 1 - 0.4848$ , respectively.

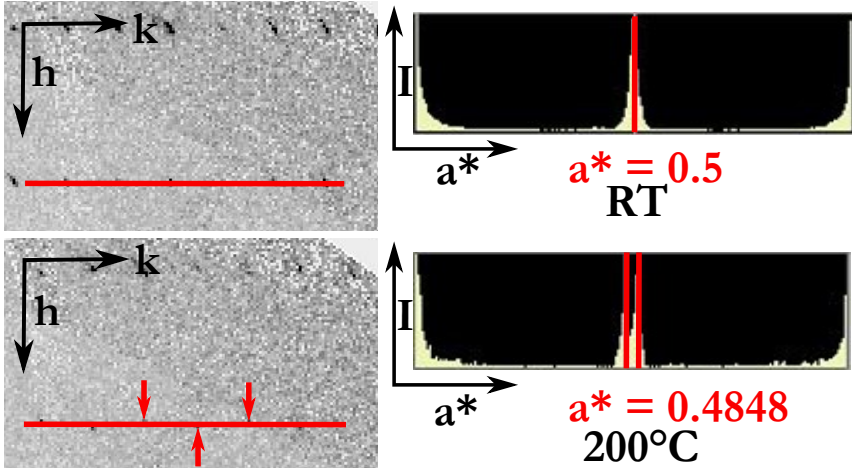


Figure 43: The left upper panel shows a reconstructed diffraction image of PdBi in  $hk1$  orientation at room temperature. With a red line it is indicated, that the satellite reflections visible here all lie on one line. This is corroborated by the histogram plot in the upper right panel, which shows the sampled satellite intensity at  $a^* = 0.5$ . The left lower panel also shows a reconstructed diffraction image in  $hk1$  orientation, but at  $200^\circ\text{C}$ . Inspecting the red line here, it is indicated with the red arrows that the satellite reflections have moved away from the line. This is better visible in the histogram plot on the lower right side, where the single peak position visible above has split into two positions.

From a modelling perspective this induces a quite subtle, yet extraordinary change: While the space group stays the same, the orientation is changed so that the unique axis is now the  $a$ -axis. The current working theory for the reason behind this is, that there is a phase transformation around  $200^\circ\text{C}$  which is the origin for this rearrangement. This phase transformation has previously been noted by Bhatt and Schubert [27] as a displacive transition transforming an orthorhombic structure in to a monoclinic structure (see chapter 2.2.2). Moreover it can also be seen in the here presented DSC study in Figure 38.

Structurally, no changes can be seen and the atomic arrangements are still the same as in Figure 42.

In the high temperature structure of PdBi stacking faults, similar to the ones in AuIn can be found. Since the direction of the modulation is parallel to the  $a$ -axis, the faults appear along this axis and after every 33 atoms. However the difference between  $q_{RT} = (0.5, 0, 0)$  and  $q_{200^\circ\text{C}} = (0.4848, 0, 0)$  requires a 66-fold superstructure as indicated by equation 9, which exquisitely highlights the two fold superstructure nature found in this alloy.

$$\frac{1}{q_{RT} - q_{200^\circ\text{C}}} \approx 66 \quad (9)$$

Intriguingly the structure undergoes a continuous change in interatomic distances between two faults. Beginning with a TII type network, where all interatomic distances are equally long, the distances condense or elongate, respectively, progressively along the *a*-axis until they reach their minimum / maximum. At that point the trend reverts until the TII-type structure is reached again (Figure 44).

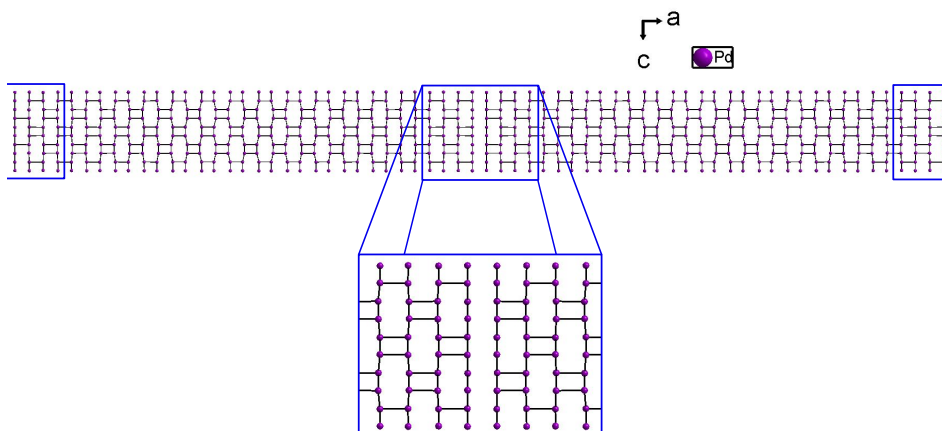


**Figure 44:** Plot of palladium positions at 200°C in the *ac*-plane. Enlarged is one occurrence of the stacking faults that can also be seen at the right and left ends highlighted in blue rectangles. In between those it can be seen how the structure rearranges from a TII type network, to a 8484-network and back to a TII type network over a period of 33 atoms.

When temperatures are raised above 200°C satellites begin to disintegrate to become diffuse scattering. This is also indicated in Figure 39, where images c) and d) show satellite reflections are becoming weak at 220°C (c) and then disintegrating at 250°C to produce diffuse scattering (d). The diffuse scattering in these measurements has not been interpreted yet.

## 5.3 PdPb

### 5.3.1 Experimental

For the growth of PdPb crystals, a previously published tempering routine was used, as discussed above (section 4.1). Nevertheless a DTA pattern was recorded for comparison with the two other TII-type phases discussed. Figure 45 displays this pattern and as can be seen it is similar to what was identified in AuIn and PdBi. Beginning with the purple cooling curve, two endothermic events can be seen at 442°C and 495°C. Comparing those temperatures to the phase diagram, the first peak matches the melting temperature of PdPb<sub>2</sub> while the second peak matches the peritectic decomposition of PdPb into Pd<sub>13</sub>Pb<sub>9</sub>. At a temperature of 604°C a small endothermic peak can be seen which is attributed to the decomposition of Pd<sub>13</sub>Pb<sub>9</sub>. Following the green cooling curve, the first exothermic peak can be seen at 593°C, respectively corresponding to the crystallisation of Pd<sub>13</sub>Pb<sub>9</sub>. Further exothermal peaks appear at 446°C and 436°C indicating the crystallisation of PdPb and PdPb<sub>2</sub>.

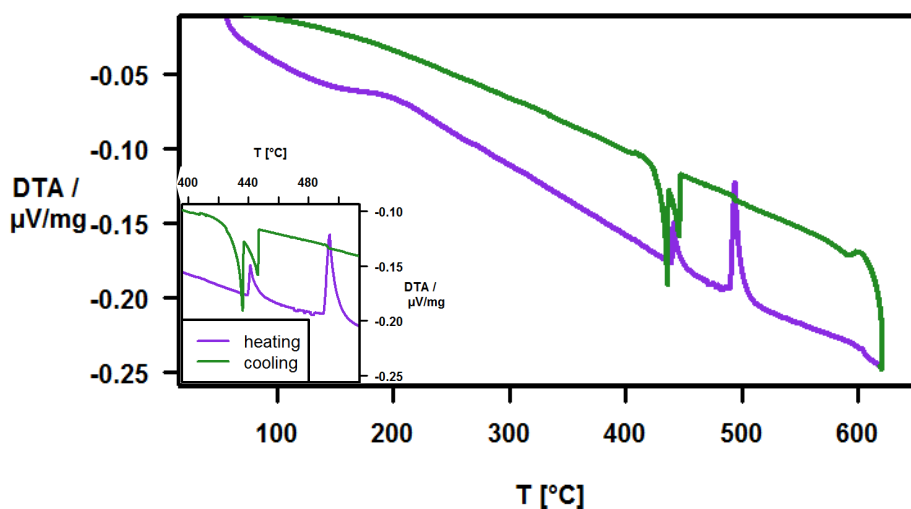


**Figure 45:** DTA plot of PdPb measured with a heating speed of 5K per minute. In the purple heating curve, peaks can be seen at temperatures of 442°C, 495°C and 604°C. Correspondingly peaks are seen in the green cooling curve at 593°C, 446°C and 436°C.

Crystals resulting from the synthesis were silver coloured metallic shards. Room temperature measurements were taken on an Xcalibur E machine equipped with a molybdenum tube. Measurements at higher temperature have not been performed yet.

### 5.3.2 Results and Discussion

The first peak in the heating curve at  $442^{\circ}\text{C}$  corresponds well to the melting temperature of  $\text{PdPb}_2$  at  $448^{\circ}\text{C}$  in the phase diagram. This indicates that the sample contained  $\text{PdPb}_2$  as a parasitic phase.

At present, only in-house room temperature data exists for this structure. This however looks promising, as it recovers the 8484-network, seen in the previously discussed structures and in this case even in an earlier report on this structure [29].

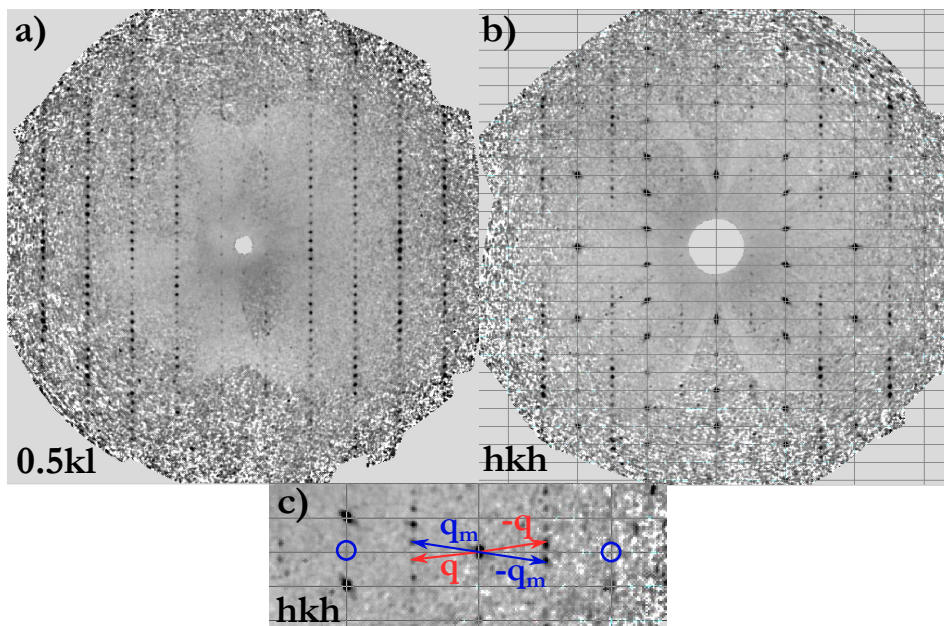


**Figure 46:** a) A reconstruction of the diffraction data in the  $(0.5, k, l)$  plane showcasing first order satellites. b) A reconstruction in the  $(h, k, h)$  plane showcasing first order satellites and main reflections. c) Zoom of the  $(h, k, h)$  reconstruction indicating the origin of the satellites. The red arrow denoted by “ $q$ ” is the original  $q$ -vector with its satellite reflection. The arrow denoted by “ $-q$ ” is its inverse which also originates from the main reflection in their middle. “ $q_m$ ” and “ $-q_m$ ” coloured in blue are the mirror images of the red  $q$ -vectors, which produce satellites that would otherwise stem from main reflections situated at the positions indicated by blue circles. These main reflections are extinct due to the apparent C-centring and hence the satellites are present only due to the twinning.

However starting with the underlying diffraction images, first order satellite reflections at a position of approximately  $(h + 0.5, k + 0.25, l + 0.5)$  are noticeable (see Figure 46). Trying to understand these satellite positions, it was uncovered that the data contains twinning that can only be seen in the  $q$ -vector and is responsible for

satellite reflections whose main reflections are extinct due to the C-centring. It is best seen when looking at an (h, k, h) reconstruction of the data as displayed in Figure 46 b. The grid in this image illustrates the orientation of the unit cells in reciprocal space. This results in a q-vector = (1/2, 0.245, 1/2), lattice parameters  $a = 3.5776$  (4) Å,  $b = 10.6056$  (14) Å,  $c = 4.261$  (10) Å,  $\alpha = 89.972$  (10)°,  $\beta = 90.122$  (9)°,  $\gamma = 89.999$  (10)° and a space group  $C\bar{1}(\alpha, \beta, \gamma)0$ , which is noteworthy the same as the one found in AuIn (section 5.1). The twinning in this structure is also unique, as it originates from four individuals that are improperly rotated around the three spacial axes and all have fractions that differ from 25%. More precisely two major (43% and 30%) and two minor (7 % and 20%) individuals are present. Inequivalent twinning fractions usually indicate that some satellite reflections should appear stronger than the others. Since this is not the case here, it is assumed that these inequivalent twinning fractions originate from disorder in the satellites or a small domain size.

The model consists of two atomic positions, where each atom is modelled with one sinusoidal position wave. The resulting electron density with the respective atomic positions can be seen in Figure 47.

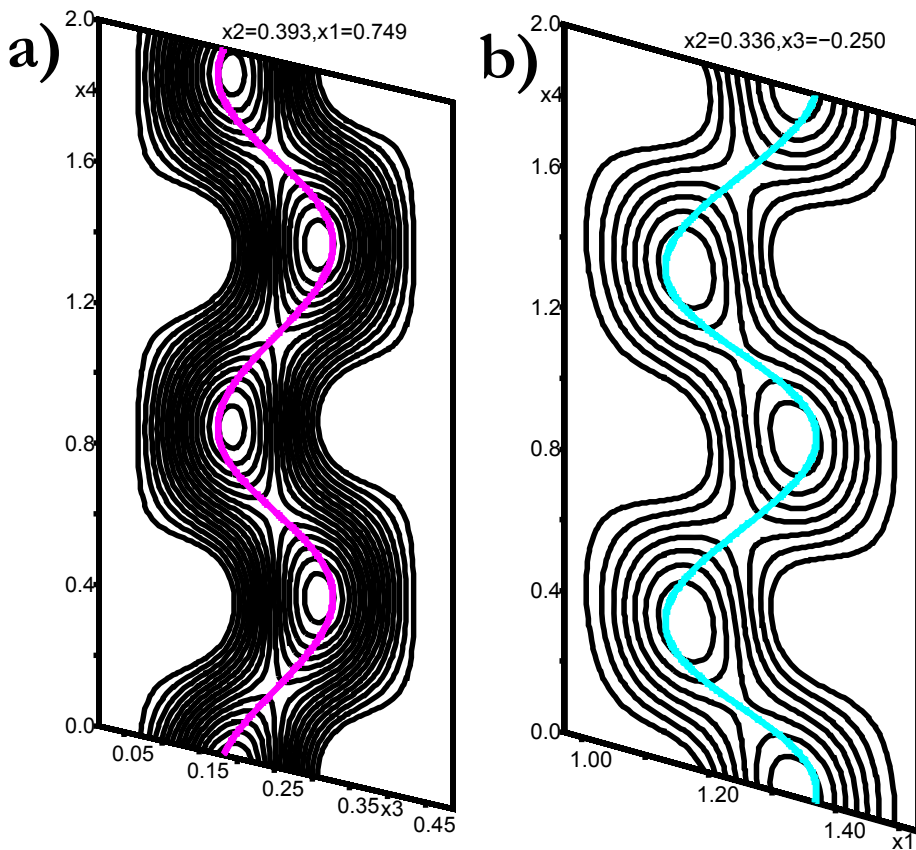


**Figure 47:** a) Electron density of the palladium atom with the atomic position marked in pink. b) Electron density of the lead atom with the atomic position marked in cyan.

As written above, this allows the recovery of the 8484-network as can be seen in Figure 48 a). Also the zig-zag layers are present in this structure as seen in Figure 48 b).

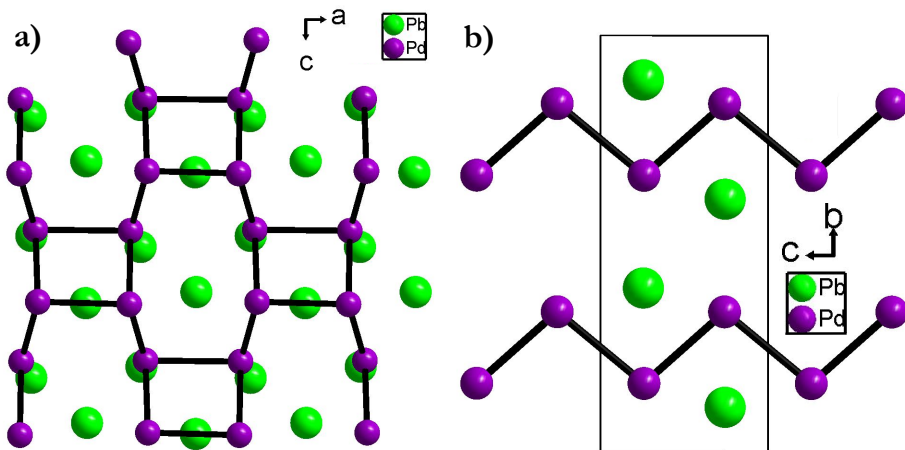


**Figure 48:** a) 8484-network of palladium (purple) with lead positions (green) in the  $ac$ -plane.  
 b) Average PdPb unit cell in the  $bc$ -plane, showcasing the zigzag layers formed by palladium.

## 5.4 Postulation of TII's Subgroup IIa

As discussed in chapter 2.2, Schob and Parthé had postulated various subgroups of the TII structure type. Those subgroups depend on the elements and unit cell axis ratios of the respective compounds [10] from which the here presented compounds slightly but significantly deviate. Moreover the respective alloys discussed in this thesis present modulated structures. As a consequence a group IIa is postulated that is defined in Table 6:

**Table 6:** Addition to Schob and Parthés [10] table of TII type compounds.

Group IIa	A: Cu or Ni group metals B: Post-transition metal or lanthanide.	$a/b = 0.34$ $a/c = 0.83$
-----------	---	------------------------------

While in the above chapters the structures have all been discussed separately, the following sub-chapters shall expand on three important points, that appear likewise in AuIn, PdBi and PdPb. Some can even be seen in preliminary measurements on other alloys that are predicted to behave similarly.

### 5.4.1 Thermal Analyses

To find a good way to grow XRD suitable single crystals of AuIn, a DTA measurement was recorded, that withheld more than just information on adequate tempering steps. In fact, it presented a phase transition, that was not accounted for in the phase



diagrams that can be found in literature [16] (AuIn) [34] (PdBi). This transition manifests in a small endothermic peak located a few tens of degrees below another endothermic peak that is larger and corresponds in temperature to the melting point of AuIn given in literature. Surprisingly, there is no corresponding exothermic peak for the small first peak and the peak persists independent of the method of cycling.

As this route had proved useful for finding a good tempering routine, the same experiment was conducted for PdBi, which also shows the characteristic double peak. PdPb also shows two endothermic peaks in the heating curve, but contrary to the other alloys also shows two exothermic peaks in the cooling curves. All DTA and DSC measurements are displayed in Figure 49 highlighting their similarities in peak occurrences.

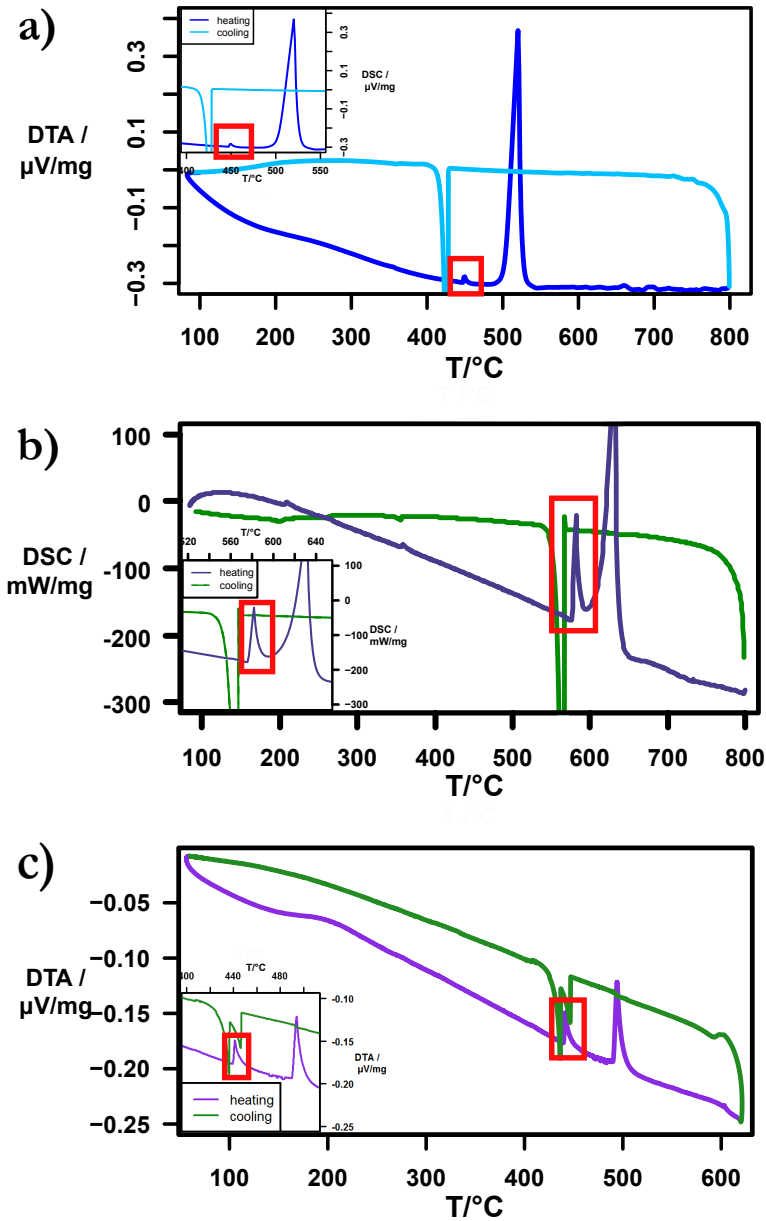


**Figure 49:** a) The ever so often displayed DSC measurement of AuIn where the zoomed area in the right upper corner shows the two characteristic endothermic peaks. Also found in the Licenciate thesis [3]. b) DSC measurement of the PdBi sample with the zoom in the lower left corner showing its characteristic endothermic peaks. c) DTA measurement of PdPb with the zoomed graph in the lower left corner showing the characteristic endothermic, and the two exothermic peaks.

### 5.4.2 Structural Shape

A second distinctive feature of these structures are their unit cells and lattices. While the unit cells all generally replicate the thallium iodide unit cell - exceptions are doubling of axes - the atomic positions deviate from the positions their thallium and iodine counterparts occupy, respectively. The way in which they deviate is again rather similar between the three here presented compounds: Au and Pd show a Peierls type like distorted version of the thallium network in all three structures (see Figure 50).

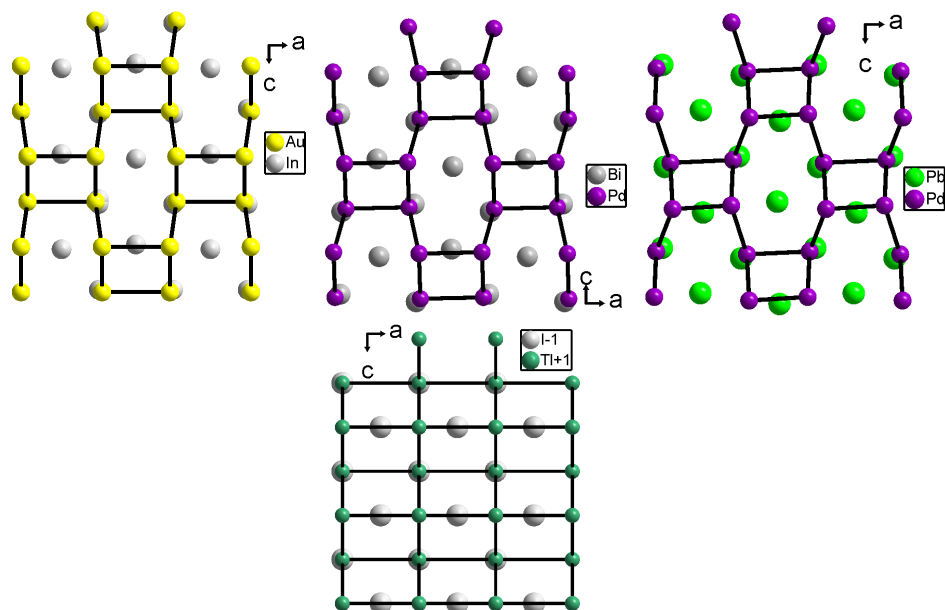


**Figure 50:** All three structures AuIn, PdBi and PdPb side by side, illustrating how similar all the structures are. The row below shows the original thallium iodide structure according to L. Helmholz [8]

### 5.4.3 Diffuse scattering

Lastly also the diffuse scattering found at higher temperatures, usually around 200°C, is reproducible in AuIn and PdBi (note that high temperature measurements for PdPb have not yet been conducted). Diffuse scattering starts appearing as a background on the satellite positions and gradually becomes stronger until it has completely replaced the satellites. In both cases diffuse rods extend along the  $k$ -axis, while they are sharp in the two other directions. Figure 51 shows the occurrences of diffuse scattering in both compounds, underlining their similarity once more.

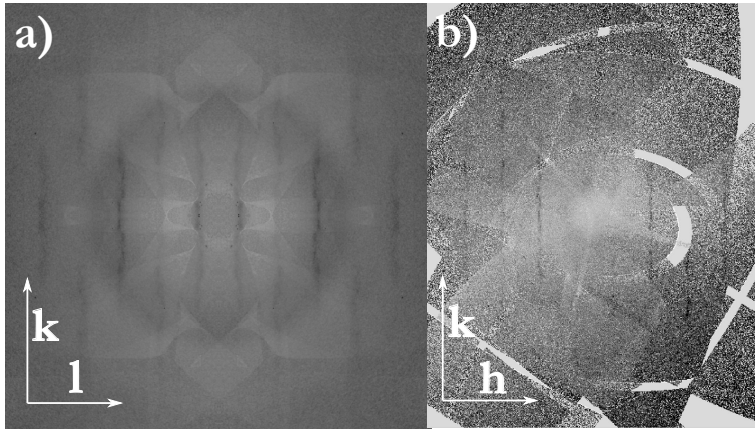


**Figure 51:** a) Diffuse intensity found in the  $kl$ -plane as found in AuIn. b) Diffuse scattering in the  $hk$ -plane as found in PdBi.

## 5.5 $\text{Sn}_3\text{Sb}_2^*$

### 5.5.1 Experimental\*

Crystals of  $\text{Sn}_3\text{Sb}_2$  were grown by a procedure, that was a little more involved, where to a given amount of antimony an overstoichiometry of tin was added. Furthermore the reagents were topped by quartz wool and some quartz shards before the quartz tube was sealed under vacuum. Subsequently the sample was homogenised at  $690^\circ\text{C}$  and annealed at  $300^\circ\text{C}$ . After the annealing step the sample was quenched to air, immediately turned upside down and transferred to a centrifuge, where it was spun at 1000 rpm. The last step separates the tin that hasn't reacted from the crystals which end up lying on top of the quartz wool.



**Figure 52:** a) Evacuated quartz tube after synthesis filled with crystals, quartz wool, quartz shards, and left over tin (from left to right). b) A cubic crystallite with a small on-growth. This is what the samples are supposed to look like. (Pictures and caption copied verbatim from the Licenciate thesis [3].)

The resulting crystals show a distinct cubic shape and were taken for single crystal diffraction studies to the CRISTAL beam line at synchrotron SOLEIL. A high quality sample was wedged between two quartz capillaries together with an additional piece

of tin. As  $\text{Sn}_3\text{Sb}_2$  loses tin and transforms to twinned  $\text{SnSb}$  while cooling down, it needs tin in its surroundings that can be soaked up by the structure during heating, to be able to transform back. This behaviour constitutes one of the extraordinary features of this material. Measurements were taken at room temperature,  $250^\circ\text{C}$  and  $370^\circ\text{C}$  and the transformation from stistaite to  $\text{Sn}_3\text{Sb}_2$  could be clearly followed in the diffraction images recorded during temperature ramping (see Figure 53). In this case the back transformation is not induced by the elevated temperature alone, only if a piece of tin is added to the capillary.

Moreover the samples were measured at a wavelength of  $\lambda = 0.42484 \text{ \AA}$  - which is close to the absorption edge of tin - to enhance the contrast between the two elements.

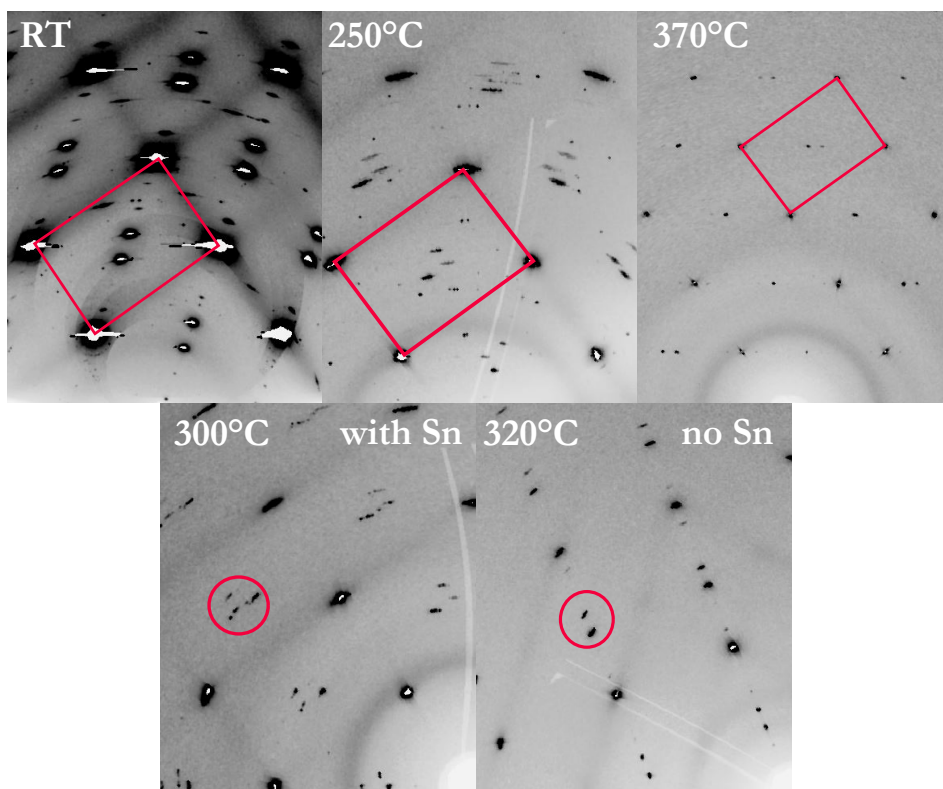


**Figure 53:** The upper row shows reciprocal space reconstructions at room temperature,  $250^\circ\text{C}$  and  $370^\circ\text{C}$  with the body diagonal plane of the cube shown as a pink rectangle. In the middle of the rectangles, groups of satellites are discernible. The lower row shows a more direct comparison of two reconstructions at  $300^\circ\text{C}$  and at  $320^\circ\text{C}$  respectively. Note that the left image was recorded with a sample containing additional tin and hence showing a quadruplet of satellites while the right image was recorded without additional tin.

### 5.5.2 Results and Discussion\*

With the enhanced contrast and the additional piece of tin to synthesise  $\text{Sn}_3\text{Sb}_2$  *in situ*, diffraction data of the sought after structure could be recorded and interpreted.

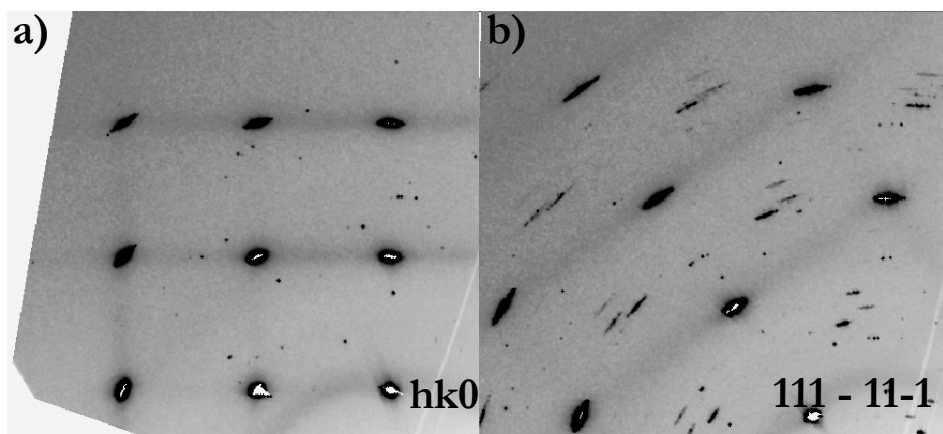


**Figure 54:** Two reconstructed images of diffraction spots at 250°C. a) Shows the  $hk0$  layer, where only main reflections can be seen. b) Shows the  $(111) - (11-1)$  layer which exhibits rectangles of intense main reflections and smaller rectangles with less intense satellite reflections. Also found in the Licenciante thesis [3].

At 250°C, when there is enough additional tin to be soaked up, first order satellite reflections can be found, *i.e.* the structure becomes incommensurate as expected. Reconstructed diffraction images can be seen in Figure 54, highlighting the first exciting oddity of this structure. Main reflections order on the corners of a cube, where satellites reside only along the four body diagonals of the respective cubes. This is easiest imagined on the example of a tesseract as displayed in Figure 55.

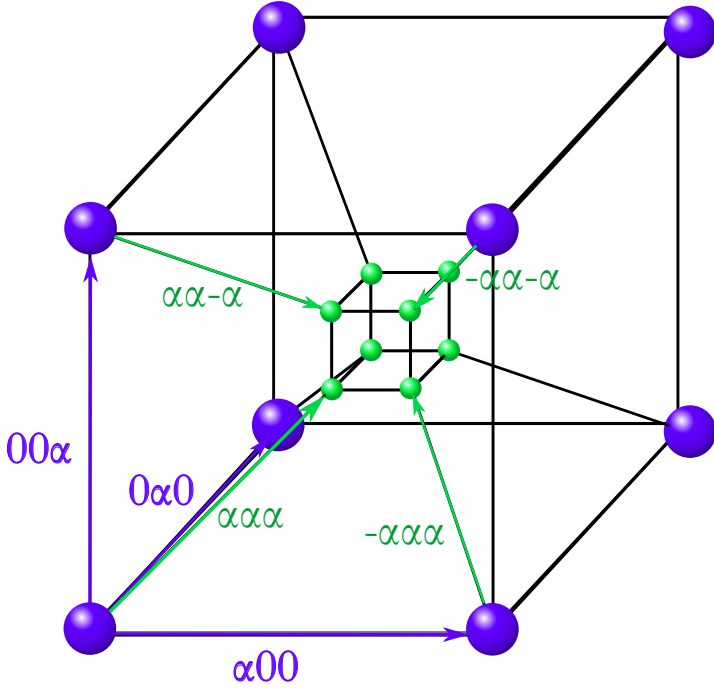


**Figure 55:** A tesseract decorated with purple spheres indicating main reflection positions and green spheres indicating satellite reflection positions. The green arrows indicate the q-vector orientations needed for the (3+4)D indexation, while the purple arrows indicate the q-vectors required for the (3+3)D indexation. Also found in the Licenciate thesis [3].

All eight of the satellite reflections are genuine, meaning they do not originate from twinning or other symmetry effects. Hence this structure would technically require four q-vectors to be properly described. However this still leaves four q-vectors of the form:

$$q_1 = (\alpha, \alpha, \alpha) \tag{10}$$

$$q_2 = (\alpha, -\alpha, -\alpha) \tag{11}$$

$$q_3 = (-\alpha, -\alpha, \alpha) \tag{12}$$

$$q_4 = (-\alpha, \alpha, -\alpha) \tag{13}$$

where  $\alpha = 0.473(6)$ . The respective vectors are indicated in green in Figure 55. Since structures with more than two q-vectors are rare and no programs exist that incorporate more than three q-vectors, a coordinate transformation was employed, resulting in only three q-vectors required to describe the satellites properly (purple q-vectors in Figure 55).

$$q_1^* = (\alpha, 0, 0) \quad (14)$$

$$q_2^* = (0, \alpha, 0) \quad (15)$$

$$q_3^* = (0, 0, \alpha) \quad (16)$$

Furthermore this requires the use of the following extinction condition: in reflections of the type  $hklmnp$ ,  $mnp$  must either all be even or all be odd [3]. In the refinement itself the  $q^*$ -vectors were suppressed and only the following combinations allowed:

$$q_1 = q_1^* + q_2^* + q_3^* \quad (17)$$

$$q_2 = q_1^* - q_2^* - q_3^* \quad (18)$$

$$q_3 = -q_1^* - q_2^* + q_3^* \quad (19)$$

$$q_4 = -q_1^* + q_2^* - q_3^* \quad (20)$$

which results in a back transformation to the original four  $q$ -vectors.

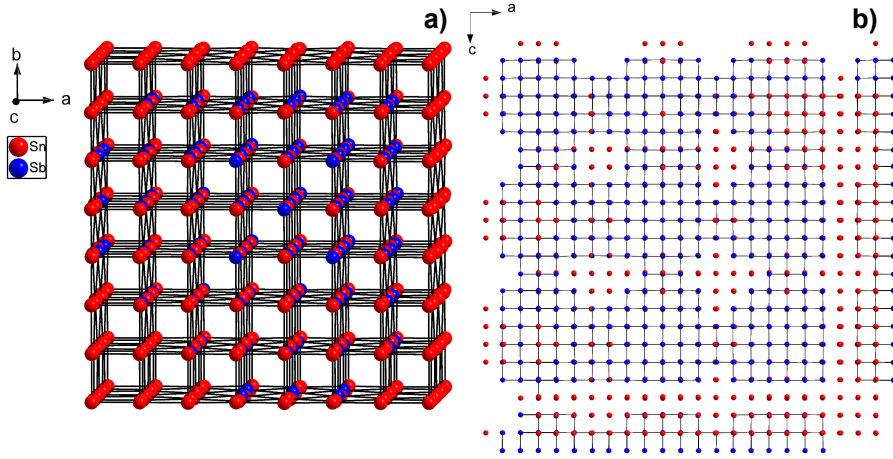
Thus the data could be modelled with a one atom model in the space group  $Xm\bar{3}m$ . The single atom is characterised by seven occupational modulation waves to allow for interchange between Sn and Sb, seven positional modulation waves and three ADP modulation waves; all of which employ a sinus function. Additionally, the atomic position is constrained not to exceed an occupation of one, while the partial occupancies of Sn and Sb are bound to result in a 3:2 stoichiometry while not surpassing unity. Since these measurements were taken close to the tin absorption edge special caution needs to be exercised with refining the occupancies, which under these conditions strongly correlate with the anomalous scattering factors  $f'$  and  $f''$ . To find proper values for  $f'$  and  $f''$ , they were refined against a previously known Sn-Sb structure of which data had been measured at the same beam time. Resulting were  $f'$  and  $f''$  values significantly different from those tabulated [59], which moreover resulted in nonphysical values for the amplitudes of the modulation functions (larger than one or smaller than zero). Thereupon the modulation amplitudes were fixed to physically meaningful values and  $f'$  and  $f''$  of Sn were refined. This leaves two refinable parameters for the modulation, one for the ADP - all other structural parameters are fixed in the basic model - and the overall scale factor. Thus a highly complex structure can be described by only four refinable parameters! Emerging therefrom are the following refinement values:

Table 7: Refinement values for  $\text{Sn}_3\text{Sb}_2$ .

$R_{\text{main}}(\text{obs})$	5.2 %
$R_{\text{sat}}(\text{obs})$	16.6 %



Images of the resulting structure are displayed in Figure 56. It is built from  $7 \times 7 \times 7$  atoms wide cubic clusters that order in a NaCl type pattern and are interleaved by pure sheets of tin atoms. This behaviour matches perfectly with what has been found for other structures in the Sn-Sb phase diagram (chapter 2.3.1), where structures are built of 7 layers of NaCl type, interleaved by various amounts of pure antimony.



**Figure 56:** Approximate pictures of the  $\text{Sn}_3\text{Sb}_2$  crystal structure exhibiting its typical NaCl like pattern. a) A single cluster cube exposing the nature of the cubes being built of  $7 \times 7 \times 7$  atoms. b) This a-c layer shows how the single clusters are interleaved by pure sheets of Sn. Also found in the Licenciate thesis [3].

It should be mentioned, that this structure can also be modelled as a twinned rhombohedral structure with a (3+1)D modulation. While the fit parameters for this description are already worse, a twinned rhombohedral description is also too similar to stistaite to explain that the two alloys form distinct, adjacent phases that also show different crystal morphologies. Since the twinning pattern originating from ht- $\text{Sn}_3\text{Sb}_2$  clearly requires a cubic structure and even the elemental tin forming on cool-down mimicking a cubic pattern, another phase transformation at higher temperatures would be required by the (3+1)D modulated space group. In the small range above ht- $\text{Sn}_3\text{Sb}_2$  and below the liquidus line, no further phase transformation has hitherto been found.

## 6 Outlook\*

After a year's research, one realises that it could have been done in a week.

---

William Henry Bragg

In the future, the suggestion that there is a new subcategory of TII structures and that those structures show the non-modulated TII structure at temperatures between their two melting peaks should be investigated.

To further inspect the possibility of a new subgroup of thallium iodides, more structures of that kind need to be synthesised and structurally characterised. Judging from their lattice parameter ratios the gold rare earth compounds described by McMasters *et al.* [60] seem to be well fit for further investigations in this direction.

For a further examination of the temperature span in which the TII-type compounds of group IIa exhibit the non-modulated TII structure, crystals of the here discussed compounds, together with new phases should be measured close to their melting temperature. To do so, two obstacles have to be overcome: Firstly the crystals need to be disposable, as measurements at this temperature would most probably destroy them. Secondly a suitable beam line and or measurement method has to be found. The suggested measurement temperatures (AuIn  $\sim 490^\circ\text{C}$ , PdBi  $\sim 600^\circ\text{C}$ , PdPb  $\sim 470^\circ\text{C}$ ) are very high and while modern heat blowers might easily reach those temperatures, surrounding beam line equipment, most importantly the detector, may not withstand such high temperatures. Moreover, new IIa TII-type compounds should also show unquenchable phase transitions. This would allow for further temperature dependent *in situ* studies.

Lastly the here discussed structures should undergo a more thorough investigation of their electronic structures. Although there were some examinations for AuIn and PdBi, they were far from universal and in the case of PdBi definitely opened up for more questions.

While the TII-type phases require a lot more synthetic work,  $\text{Sn}_3\text{Sb}_2$  will mainly benefit from computational investigations. Those might give insight into whether there is a possibility to circumvent the phase transition when cooling the sample to room temperature and how the mechanism for losing respectively soaking up Sn can be so fast.

## 7 References

- [1] R. Lifshitz. What is a crystal? *Zeitschrift für Kristallographie*, 222(6), 2007.
- [2] Report of the Executive Committee for 1991. *Acta Crystallographica Section A Foundations of Crystallography*, 48:922–946, 1992.
- [3] L. C. Folkers. Solving Mysteries and Outwitting Transitions: Investigating the Incommensurate Crystal Structures of AuIn and Sn<sub>3</sub>Sb<sub>2</sub>; [portal.research.lu.se/portal/files/38960801/SpikfilLauraFLUCRIS.pdf](http://portal.research.lu.se/portal/files/38960801/SpikfilLauraFLUCRIS.pdf), 2018.
- [4] C. E. Housecroft and A. G. Sharpe. *Inorganic Chemistry*. 2008.
- [5] D. C. Fredrickson and G. J. Miller. Intermetallic Chemistry: New Advances in Humanity’s Age-Old Exploration of Metals and Alloys. *Accounts of Chemical Research*, 51(2):213–213, feb 2018.
- [6] N.S. Kurnakov, S.F. Zemczuzny, and M. Zasedatelev. No Title. *Journal of the institute of Metals*, 15:305, 1916.
- [7] Z.P. Lu. [www.journals.elsevier.com/intermetallics](http://www.journals.elsevier.com/intermetallics).
- [8] L. Helmholz. The crystal structure of the low temperature modification of thal-  
lous iodide. *Zeitschrift für Kristallographie*, 95:129 – 136, 1936.
- [9] Inorganic Crystal Structure Database; [icsd.fiz-karlsruhe.de/search/basic.xhtml](http://icsd.fiz-karlsruhe.de/search/basic.xhtml).
- [10] O. Schob and E. Parthé. AB compounds with Sc, Y and rare earth metals. I. Scandium and yttrium compounds with CrB and CsCl structure. *Acta Crystallographica*, 19(2):214–224, 1965.
- [11] S. Okada, T. Atoda, and I. Higashi. Structural investigation of Cr<sub>2</sub>B<sub>3</sub>, Cr<sub>3</sub>B<sub>4</sub>, and CrB by single-crystal diffractometry. *Journal of Solid State Chemistry*, 68(1):61–67, 1987.
- [12] T. Bjurstroem and H Arnfelt. Roentgenanalyse des Eisen-Bor-Systems. *Zeitschrift fuer Physikalische Chemie, Abteilung B: Chemie der Elementarprozesse, Aufbau der Materie*, 4(2):469 – 476, 1929.
- [13] D. Hohnke and E. Parthé. AB compounds with ScY and rare earth metals. II. FeB and CrB structures of monosilicides and germanides. *Acta Crystallographica*, 20(4):572–582, 1966.
- [14] N. N. Greenwood and A. Earnshaw. *Chemistry of the Elements*. 2 edition, 1998.
- [15] W. M. Haynes, editor. *CRC Handbook of Chemistry and Physics*. CRC Press / Taylor & Francis, Boca Raton, FL., 97 edition, 2017.

- [16] I. Ansara and J.-Ph. Nabot. AuIn Phase Diagram. *CALPHAD*, 16:13 – 18, 1992.
- [17] Inorganic Material Database (AtomWork); [crystdb.nims.go.jp/index\\_en.html](http://crystdb.nims.go.jp/index_en.html).
- [18] K. Schubert, U. Rösler, M. Kluge, K. Anderko, and L. Härle. Kristallographische Ergebnisse an Phasen mit Durchdringungsbindung. *Naturwissenschaften*, 40(16):473, 1953.
- [19] K. Schubert, H. Breimer, and R. Grohe. Zum Aufbau der Systeme Gold-Indium, Gold-Zinn, Gold-Indium-Zinn und Gold-Zinn-Antimon. *Zeitschrift für Metallkunde*, 50:146–153, 1959.
- [20] S. E. R. Hiscocks and W. Hume-Rothery. The equilibrium diagram of the system gold-indium. *Proceedings of the Royal society of London. Series A, Mathematical and Physical Sciences*, pages 318 – 330, 1964.
- [21] V. K. Nikitina, A. A. Babitsyna, and Yu. K. Lobanova. Phase diagram of the gold-indium system. *Izv. Akad. Nauk SSSR, Neorg. Mater.*, 7:421–427, 1971.
- [22] J. P. Goral and L. Eyring. The Gold-Indium Thin Film System: A High Resolution Electron Microscopy Study. *Journal of the Less Common Metals*, 116:63–72, 1986.
- [23] H. Leidecker and M. Sampson. Indium Solder Encapsulating Gold Bonding Wire Leads to Fragile Gold-Indium Compounds and an Unreliable Condition that Results in Wire Interconnection Rupture. Technical report, NASA, 2003.
- [24] K. Okawa, M. Kanou, T. Katagiri, H. Kashiwaya, S. Kashiwaya, and T. Sasagawa. Crystal growth and physical properties of the noncentrosymmetric superconductor PdBi. *Physics Procedia*, 45:101–104, 2013.
- [25] H. Xu, B. Yan, K. Zhang, J. Wang, S. Li, C. Wang, Y. Du, P. Yang, S. Jiang, and S. Song. N-doped graphene-supported binary PdBi networks for formic acid oxidation. *Applied Surface Science*, 416:191–199, 2017.
- [26] N. N. Zhuravlev. Structure of superconductores. X. Thermal, microscopic and X-ray investigation of the bismuth-palladium system. *Zhurnal Eksperimental'noi i Teoreticheskoi Fiziki*, 5:1064 – 1072, 1957.
- [27] Y. C. Bhatt and K. Schubert. Kristallstruktur von PdBi. *Journal of The Less-Common Metals*, 64(2):17–24, 1979.
- [28] T. B. Massalski, H. Okamoto, P. R. Subramanian, and L. Kacprzak, editors. *Binary Alloy Phase Diagrams*. ASM International, 2nd edition, 1990.

- [29] H.W. Mayer and K. Schubert. Kristallstruktur von PdPb.r\*. *Less-common metals*, 72, 1980.
- [30] W. H. Bragg and W. L. Bragg. The Reflection of X-rays by Crystals. *Proceedings of the Royal Society A: Mathematical, Physical and Engineering Sciences*, 88(605):428–438, jul 1913.
- [31] P. Atkins, L. Jones, and L. Laverman. *Chemical Principles: The Quest for Insight*. Macmillan Higher Education, 6th editio edition, 2013.
- [32] A. R. West. *Basic Solid State Chemistry*. Wiley, second edition, 2014.
- [33] H. E. Swanson and R. K. Fuyat. Standard X-ray diffraction powder patterns. *National Bureau of Standards Circular*, 539:1–65, 1953.
- [34] T. B. Massalski. Phase Diagram PdBi. In T. B Massalski, editor, *Binary Alloy Phase Diagrams*, pages 3304–3306. 2 edition, 1990.
- [35] R. I. McCallum. Occupational exposure to antimony compounds. *Journal of Environmental Monitoring*, 7(12):1245, 2005.
- [36] S. Lidin, J. Christensen, K. Jansson, D. Fredrickson, R. L. Withers, L. Noren, and S. Schmid. Incommensurate Stistaite—Order Made to Order. *Inorganic Chemistry*, 48(12):5497–5503, jun 2009.
- [37] C. S. Barrett, P. Cucka, and K. Haefner. The crystal structure of antimony at 4.2, 78 and 298° K. *Acta Crystallographica*, 16(6):451–453, jun 1963.
- [38] C. Hammond. ‘Whin Brow’: the house at which the new science of X-ray crystallography began. *Crystallography Reviews*, 22(3):220–227, jul 2016.
- [39] W. Massa. *Kristallstrukturbestimmung*. Vieweg+Teubner, 2009.
- [40] E. Prince, editor. *International Tables for Crystallography Volume C: Mathematical, physical and chemical tables*, volume C of *International Tables for Crystallography*. International Union of Crystallography, Chester, England, 3rd edition, oct 2006.
- [41] S. van Smaalen. *Incommensurate Crystallography*. Oxford University Press, jun 2007.
- [42] S. Esmailzadeh, S. Lundgren, U. Hälenius, and J. Grins. Bi(1-x)Cr(x)O(1.5+1.5x'), 0.05≤x≤0.15: A New High-Temperature Solid Solution with a Three-Dimensional Incommensurate Modulation. *Journal of Solid State Chemistry*, 156(1):168–180, jan 2001.

- [43] V. Petricek, M. Dusek, and L. Palatinus. Crystallographic Computing System JANA2006: General Features. *Zeitschrift für Kristallographie*, 229(5):345–352, 2014.
- [44] [www.dplot.com/examples/surface-plot-phong-shading.png](http://www.dplot.com/examples/surface-plot-phong-shading.png), 2017.
- [45] A. Simonov. Meerkat, 2015.
- [46] P. Willmott. *An Introduction to Synchrotron Radiation*. Wiley, jul 2011.
- [47] V. K. Pecharsky and P. Y. Zavalij. *Fundamentals of Powder Diffraction and Structural Characterization of Materials*. Springer US, Boston, MA, second edition, 2009.
- [48] W. C. Phillips, A. Stewart, M. Stanton, I. Naday, and C. Ingersoll. High-sensitivity CCD-based X-ray detector. *Journal of Synchrotron Radiation*, 9(1):36–43, 2002.
- [49] CrysAlisPRO, Technologies, Oxford Diffraction / Agilent Technologies UK Ltd, Yarnton, England, 2017.
- [50] User Manual Xcalibur Series, 2003.
- [51] L. Palatinus and G. Chapuis. SUPERFLIP – a computer program for the solution of crystal structures by charge flipping in arbitrary dimensions. *Journal of Applied Crystallography*, 40(4):786–790, aug 2007.
- [52] H. P. Klug and L. E. Alexander. *X-Ray Diffraction Procedures: For Polycrystalline and Amorphous Materials*. Wiley, 2nd edition, 1974.
- [53] Synchrotron Soleil; [www.synchrotron-soleil.fr/en](http://www.synchrotron-soleil.fr/en).
- [54] Synchrotron Diamond; [www.diamond.ac.uk/Home.html](http://www.diamond.ac.uk/Home.html).
- [55] L. C. Folkers, A. Simonov, F. Wang, and S. Lidin. The Mystery of the AuIn 1:1 Phase and Its Incommensurate Structural Variations. *Inorganic Chemistry*, 57(5):2791–2796, mar 2018.
- [56] P. Bayliss. Revised unit cell dimensions, space group, and chemical formula of some metallic minerals. *Canadian Mineralogist*, 28:751 – 755, 1990.
- [57] V.M. Ionov, N.A. Tomilin, A.E. Prozorovskii, A.N. Klimenko, Yu.V. Titov, S.G. Zhukov, and G.V. Fetisov. Anisotropy of Physical Properties and Crystal Structure of PdBi in the Interval 293-570 K. *Kristallografiya*, 34:829 –834, 1989.

- [58] L. C. Folkers, H. E. Mitchell Warden, D. C. Fredrickson, and S. Lidin. Incommensurability in Entangled Bonding Networks: Temperature-Dependent Structural Variations in PdBi. 2019.
- [59] C. T. Chantler. Detailed Tabulation of Atomic Form Factors, Photoelectric Absorption and Scattering Cross Section, and Mass Attenuation Coefficients in the Vicinity of Absorption Edges in the Soft X-Ray ( $Z = 30-36$ ,  $Z = 60-89$ ,  $E = 0.1$  keV-10 keV), Addressing Convergence I. *Journal of Physical and Chemical reference Data*, 29(4):597–1048, 2000.
- [60] O. D. McMasters, K. A. JR. Gschneider, G. Bruzzone, and A. Palenzona. Stoichiometry, crystal structures and some melting points of the lanthanide-gold alloys. *Journal of the Less-Common metals*, 25(2978):135–160, 1971.

# Scientific publications

## Author contributions

Co-authors are abbreviated as follows:

Sven Lidin (SL), Arkadiy Simonov (AS), Fei Wang (FW), Hillary E. Mitchell Warden (HEMW), Daniel C. Fredrickson (DCF).

### **Paper I: The Mystery of the AuIn 1:1 Phase and its Incommensurate Structural Variations**

I did the syntheses, measurements, analyses and wrote most of the paper. SL suggested the project, guided me through measurements, analyses and writing. AS did the 3D pair distribution function analyses. FW did the first principle quantum mechanical calculations.

### **Paper II: Incommensurability in Entangled Bonding Networks: Temperature-Dependent Structural Variations in PdBi**

I did the syntheses, measurements and wrote most of the paper. SL suggested the project, guided me through measurements and writing. SL did most of the analyses and I contributed with input. HEMW and DCF conducted the theoretical analyses and wrote the respective part of the paper.

### **Paper III: PdPb: The Incommensurately modulated structure of another TII type compound**

I did the syntheses, measurements and wrote most of the paper. SL suggested the project, guided me through syntheses, measurements and writing. SL did most of the analyses and I contributed with input.



**Paper IV: In situ synthesis and single crystal synchrotron X-ray diffraction study of ht-Sn<sub>3</sub>Sb<sub>2</sub>**

I did the syntheses, measurements, came up with the *in situ* measurement, analyses and proofreading of the paper. SL suggested the project, guided me through measurements, analyses and wrote the paper.





I came across this painting when I visited the History of science museum in Oxford, UK, where it was displayed in one of the last vitrines on the basement floor. The way it depicts solid state chemistry, it immediately spoke to me. For some reason it seems almost comedic how the master scientist gives orders to the little angels that have to keep the furnaces running and syntheses working. Because more than once I found myself in the position wishing to have a bunch of little angles by my side to help me run the syntheses.

Mostly however I was intrigued by how different yet similar this laboratory setup is compared to what we have in our labs today.